# Unraveling Structure-Functionality Relationships of Shape-Defined $Cu_2O$ Nanocrystal Model Catalysts for Methanol Decomposition

A THESIS SUBMITTED TO

THE GRADUATE SCHOOL OF ENGINEERING AND SCIENCE

OF BILKENT UNIVERSITY

IN PARTIAL FULFILMENT OF THE REQUIREMENTS

FOR THE DEGREE OF

MASTER OF SCIENCE

IN

CHEMISTRY

By

Kaan Karaca

August 2024

**Unraveling Structure-Functionality Relationships of Shape-Defined $Cu_2O$ Nanocrystal Model Catalysts for Methanol Decomposition**

By Kaan Karaca

August 2024

We certify that we have read this thesis and that in our opinion it is fully adequate,in scope and in quality, as a thesis for the degree of Master of Science.

Prof. Dr. Emrah Özensoy (Advisor)

Asst. Prof. Halil İbrahim Okur

Asst. Prof. Mustafa Karatok

Approved for the Graduate School of Engineering and Science

Orhan Arıkan

Director of the Graduate School

# ABSTRACT

UNRAVELING STRUCTURE-FUNCTIONALITY RELATIONSHIPS OF SHAPE-DEFINED $Cu_2O$ NANOCRYSTAL MODEL CATALYSTS FOR METHANOL DECOMPOSITION

Kaan Karaca

M.S.c in Chemistry

Advisor: Emrah Özensoy

August 2024

Methanol is one of the centerpieces of the chemical industry as a $C_1$ building block and an intermediate producing high-value chemicals such as formaldehyde, methyl methacrylate, methyl tertiary-butyl ether/ tertiary-amylmethylether, and acetic acid. The global demand for methanol is expected to grow exponentially due to its applications in hydrogen production, direct methanol fuel cells, and olefin production via the Methanol to Olefins (MTO) processes. Cu-based catalysts have been widely studied both in academia and in the industry to transform methanol into value-added chemicals at the industrial scale. Some of these academic fundamental research studies have been performed either under ultra-high vacuum (UHV), cryogenic temperature conditions utilizing single-crystal nanocatalysts or under industrially relevant high temperature-pressure conditions utilizing complex mesoporous catalysts resulting in complex data which is challenging to analyze in a conclusive manner to obtain reliable mechanistic information due to the presence of the well-known limitations in heterogenous

catalysis called “the materials gap” and “ the pressure gap”. Thus, uniquely defined model catalysts are required to bridge these gaps by offering well-ordered surfaces that can be studied under ambient conditions. This thesis focuses on the structure-functionality relationships of shape-defined $Cu_2O$ model catalysts for methanol decomposition. Cubic and octahedral $Cu_2O$ nanocrystal catalysts were synthesized and characterized by various ex-situ methods such as Scanning Electron Microscopy (SEM), X-Ray Diffraction (XRD), X-Ray Absorption Near Edge (XANES), Extended X-Ray Absorption Fine Structure (EXAFS), Attenuated Total Reflectance Infrared Spectroscopy (ATR-IR), X-Ray Photoelectron Spectroscopy (XPS) and $H_2$-Temperature Programmed Reduction ($H_2$-TPR). The nature of the surface-active sites were characterized by CO adsorption via in-situ Fourier Transform Infrared Spectroscopy (in-situ FTIR) and the morphology-dependent methanol and formaldehyde decomposition properties were studied via in-situ FTIR and Temperature Programmed Desorption (TPD). The results showed that c-$Cu_2O$ and o-$Cu_2O$ have distinct structure-functionality relationships for methanol decomposition. It is proposed that the labile surface oxygens that can be readily donated from the c-$Cu_2O$ surface can facilitate low-temperature ($T \leq 250$ °C) methanol/methoxy oxidation to formates which in turn yield predominantly $CO_2$ and $H_2O$ as the total oxidation products. In contrast, limited reducibility of the c-$Cu_2O$ surface only allows methanol/methoxy oxidation to first formaldehyde and then to dioxymethylene, eventually yielding predominantly CO and $H_2$ as the thermal decomposition products, indicating the predominance of dehydrogenation catalytic pathways rather than total oxidation  thus, unraveling the structure-functionality relationships of shape-defined $Cu_2O$ nanocrystal model catalysts for methanol decomposition.

**Keywords:** $Cu_2O$, Methanol Decomposition, Model Catalysts, Structure-Functionality Relationships

# ÖZET

## METANOL BOZUNMASI İÇİN ŞEKİL TANIMLI $Cu_2O$ NANOKRİSTAL MODEL KATALİZÖRLERİN YAPI-FONKSİYONELLİK İLİŞKİLERİNİN AYDINLATILMASI

Kaan Karaca

Kimya, Yüksek Lisans

Tez Danışmanı: Emrah Özensoy

Ağustos 2024

Metanol, formaldehit, metil metakrilat, metil tersiyer-bütil eter/tersiyer-amilmethileter ve asetik asit gibi değerli kimyasalları üretmek amacıyla kullanılan, kimya endüstrisinin önemli C1 yapı taşlarından biridir. Metanol üretiminde küresel talebin, metanolün endüstriyel olarak önem arz eden alanlardaki uygulamaları nedeniyle katlanarak artması beklenmektedir. Bu uygulamalar arasında hidrojen üretimi, doğrudan metanol yakıt hücreleri (DMFC) ve Metanol'den Olefinlere (MTO) gibi prosesler yer almaktadır. Literatürde, metanol ile heterojen katalizörlerin etkileşimini daha iyi anlamak amacıyla Cu katalizörler yaygın olarak incelenmiştir. Bu çalışmalar, ultra-yüksek vakum (UHV), kriyojenik sıcaklık koşulları altında tek kristal nano katalizörler kullanılarak veya endüstriyel koşullara yakın, yüksek sıcaklık-basınç koşulları altında kompleks mezo-gözenekli katalizörler kullanılarak gerçekleştirilmiştir. Bu durum, mekanistik çalışmalarda artan bir karmaşıklığa ve heterojen kataliz alanında iyi bilinen "malzeme uçurumu" ve "basınç uçurumu" sorunlarına neden olmaktadır. Bu nedenle model

katalizörler, yüksek düzenliliğe sahip yüzeyleri ve oda koşullarında incelenebilmeleri sebebiyle bu sorunlara bir çözüm olarak kullanılmaktadır. Bu tez, metanol bozunması sırasında, iyi-tanımlı şekillere sahip $Cu_2O$ model katalizörlerinin, katalitik yapı-işlev ilişkilerine odaklanmaktadır. Bu çalışmada, kübik ve oktahedral şekillere sahip $Cu_2O$ nano kristal model katalizörler sentezlenmiş ve Taramalı Elektron Mikroskobu (SEM), X-Işını Kırınımı (XRD), X-Işını Absorpsiyonu Yakın Kenar Yapısı (XANES), Genişletilmiş X-Işını Absorpsiyonu İnce Yapısı (EXAFS), Zayıflatılmış Toplam Yansıma Kızılötesi Spektroskopisi (ATR-IR), X-Işını Fotoelektron Spektroskopisi (XPS) ve $H_2$-Sıcaklık Programlı İndirgeme ($H_2$-TPR) gibi çeşitli ex-situ yöntemlerle karakterize edilmiştir. Yüzeydeki aktif bölgelerin doğası, in-situ Fourier Dönüşümü Kızılötesi Spektroskopisi (in-situ FTIR) ile CO adsorpsiyonu aracılığıyla karakterize edilmiştir. Ayrıca, morfolojiye bağlı metanol ve formaldehit bozunması in-situ FTIR ve Sıcaklık Programlı Desorpsiyon (TPD) aracılığıyla incelenmiştir Bu çalışmanın bulguları, metanol bozunmasının daha iyi anlaşılmasını sağlamayı ve şekli tanımlanmış $Cu_2O$ katalizörleri arasındaki yapı-fonksiyonellik ilişkisini açıklamayı amaçlamaktadır. Sonuçlar, c-$Cu_2O$ yüzeyinden kolayca bağışlanabilen yüzey oksijenlerinin, düşük sıcaklıkta ($T \leq 250$ °C) metanol/metoksi oksidasyonunu gerçekleştirerek format oluşturduğunu ve bu türlerin çoğunlukla $CO_2$ ve $H_2O$'ya ayrışarak total oksidasyon ürünlerini meydana getirdiğini göstermektedir. Buna karşılık, o-$Cu_2O$ yüzeyinin sınırlı indirgenebilirliği, metanol/metoksi oksidasyonunun önce formaldehit, ardından dioxymethylene oluşturduğu ve nihayetinde CO ve H2'nin termal ayrışma ürünleri olarak ortaya çıktığı gözükmektedir. Bu durum, total oksidasyondan ziyade katalitik dehidrojenasyon yollarının baskın olduğunu göstermektedir. Bu sonuçlara dayanarak, şekil tanımlı $Cu_2O$ nanokristal model katalizörlerinin metanol ayrışmasındaki yapı-fonksiyon ilişkileri ortaya çıkarılmaktadır.

**Anahtar Kelimeler:** $Cu_2O$, Metanol Bozunması, Model Katalizörler, Yapı-İşlev İlişkileri

# Acknowledgements

I would like to sincerely thank my adviser, Prof. Dr. Emrah Özensoy for all the support, encouragement, motivation and inspiration that he provided during my masters studies. His deep understanding of science and the excitement that he creates during our discussions have greatly influenced the way that I look into this world and research. It was an honor for me to work with you and develop as a scientist.

I would also express my gratitude to the members of my thesis committee, Asst. Prof. Halil I. Okur, and Asst. Prof. Mustafa Karatok for their precious time and their insightful criticism and recommendations.

I would like to thank Prof. WeiXin Huang (USTC, Hefei) for fruitful discussions on $Cu_2O$ nanocrystal synthesis.

I also want to thank and appreciate all of the precious members of Ozensoy Research Group especially to Ayşe Dilay Erdali, Yusuf Koçak, Miray Tamer, and Seda Karaboğa for their constant support and for the time that we spent on making numerous scientific discussions. I would also like to thank Ahsan Jalal, Beyzanur Erdivan, Ahmet Arda Türk, and Ömer Faruk Sadak for their friendship and support during my studies.

Finally, I would like to thank to my dear family, Anne, Baba, Lara, and Kayra and to my dear friends for believing in me and constantly supporting me. I am so lucky to have you all by my side.

TABLE OF CONTENTS

LIST OF TABLES

LIST OF FIGURES

LIST OF APPENDIX FIGURES

# 1 Introduction

## 1.1 Methanol Industry

Methanol is one of the centerpieces of the chemical industry not only as a $C_1$ product but also as an intermediate and ubiquitous chemical feedstock. The global methanol production has reached 98 Mt/year as of 2020 and it is projected to reach 500 Mt/year by 2050 [1]. The projected exponential growth of methanol production displays its crucial role in various industries.

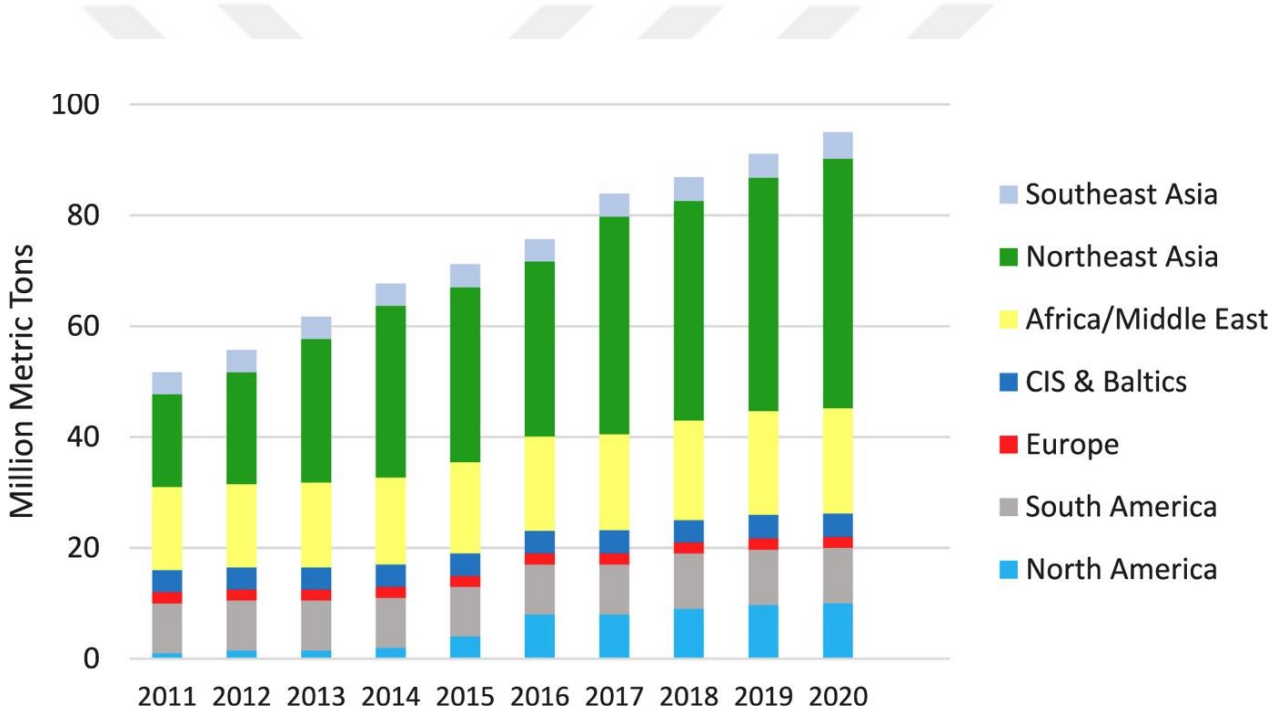


**Figure 1:** Global annual methanol production (Adapted from [1]).

Methanol is a fundamental $C_1$ building block in the production of various higher-value chemicals which have applications in a wide range of industries. Formaldehyde, methyl methacrylate, methyl tertiary-butyl ether/ tertiary-amylmethylether, and acetic acid are some of the primary products of the methanol industry [1,2]. Figure 2 shows the value chain of methanol demonstrating the wide range of industries in which methanol is utilized.

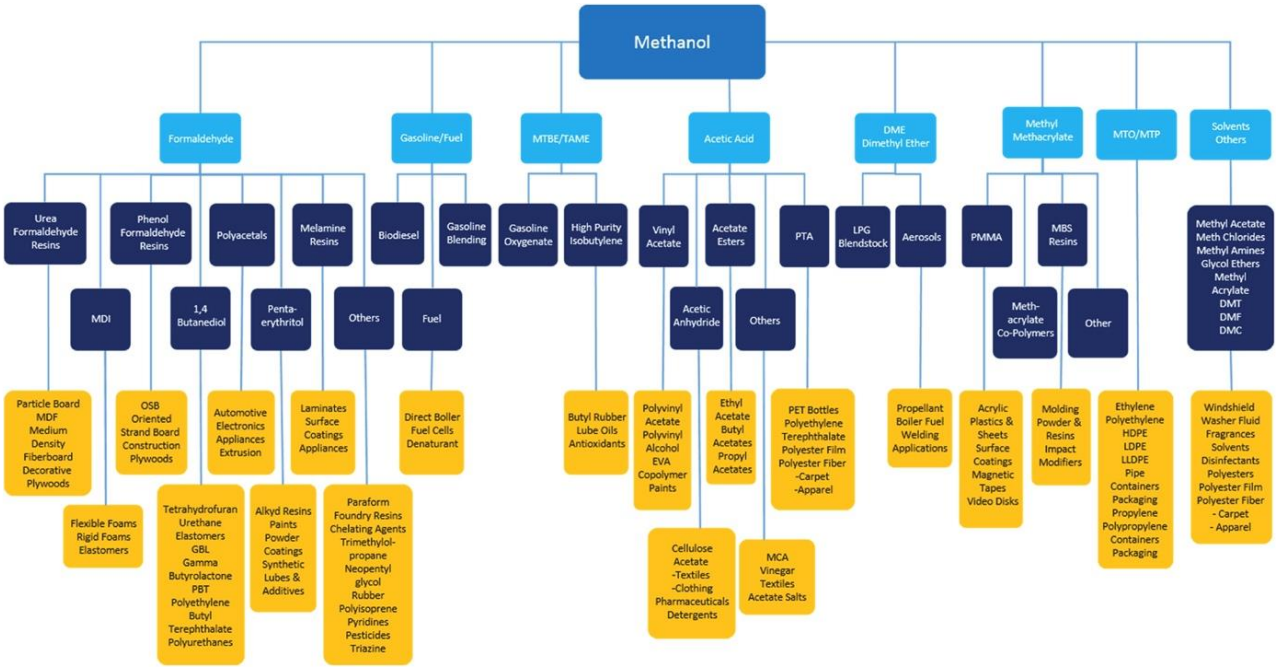


**Figure 2:** Value-chain of methanol (Adapted from [1]).

The methanol-to-olefins (MTO) process is another major industrial process that holds foremost importance. This process is developed by China and creates an alternative pathway for the production of olefins that do not rely on traditional oil resources. MTO utilizes methanol derived from non-oil resources such as coal, natural gas or biomass for the production of basic petrochemicals such as ethylene and propylene. As of 2010, this process is commercialized for the production of petrochemicals and largely used in countries that do not have access to oil resources. [3, 4].

Methanol also plays a crucial role in hydrogen generation and methanol fuel cells/direct methanol fuel cells (DMFC). Hydrogen is considered as an important green energy source and has important applications such as fuel for transportation, fuel cells, energy vectors, etc. and DMFCs can be used as portable power units for small electronic which is of particular advantage in military applications. Methanol has a high H/C ratio, and it is easy and safe to store, transport, and handle methanol due to its liquid form at ambient temperature and pressure.

Furthermore, the production of methanol from biomass or $CO_2$ provides a renewable source for hydrogen production. These properties make methanol a desired source for hydrogen production and fuel cell applications [5-8].

## 1.2 Reactions of methanol

### 1.2.1 Methanol synthesis (MS)

Industrial methanol synthesis is typically carried out using a mixture of $CO/CO_2/H_2$ at high pressures between 50-100 bar at 250-300˚C and $Cu/ZnO/Al_2O_3$ is the most widely used catalyst for this reaction [9, 10]. Figure 3 shows the major methanol synthesis pathways. The main reactions involved in this process are $CO_2$ hydrogenation (1), CO hydrogenation (2) and water-gas shift (WGS) (3) reactions listed below:

$$CO_2 + 3H_2 \longrightarrow CH_3OH + H_2O \quad (1)$$

$$CO + 2H_2 \longrightarrow CH_3OH \quad (2)$$

$$CO + H_2O \longrightarrow CO_2 + H_2 \quad (3)$$

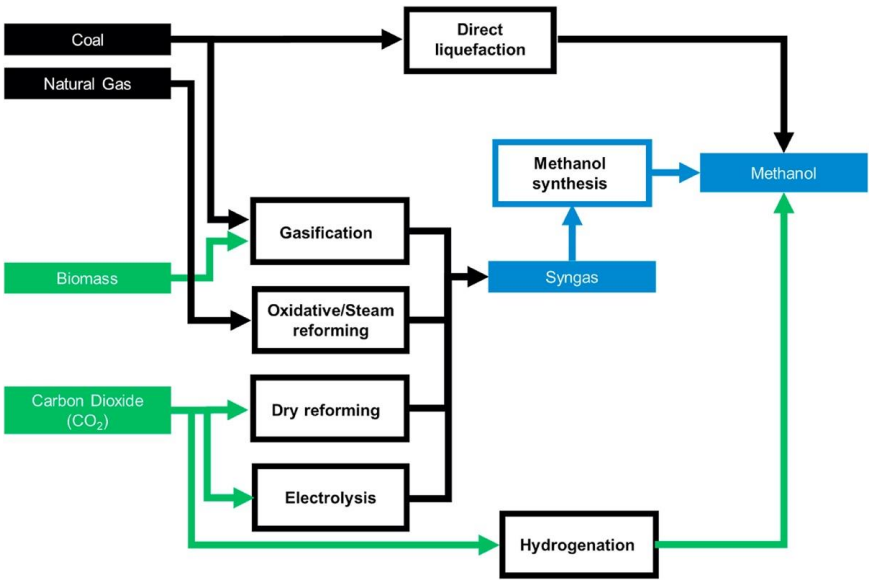


**Figure 3:** Methanol synthesis pathways (Adapted from [11]).

### 1.2.2 Methanol decomposition (MD)

The methanol decomposition (4) is an endothermic reaction yielding $H_2$ and CO. Methanol decomposition is mostly used for hydrogen production as it can reach high conversion even at 200˚C and a variety of catalysts have been studied in the literature containing different catalytic active sites such as Cu, Zn, Ni, etc. [11-14]

$$CH_3OH \longrightarrow CO + 2H_2 \qquad \Delta^\circ H_{rxn} = 90.1 \text{ kJ mol}^{-1} \quad (4)$$

### 1.2.3 Steam reforming of methanol (SRM)

Methanol steam reforming is generally used for hydrogen production as it creates higher moles of hydrogen per mole of methanol compared to the oxidative processes. Figure 4 illustrates the SRM process and shows the used catalysts and conditions. SRM is an endothermic reaction, as shown in reaction (5) and results in the formation of CO and $H_2$ [11,12].

$$CH_3OH + H_2O \longrightarrow 3H_2 + CO \qquad \Delta^\circ H_{rxn} = 50 \text{ kJ mol}^{-1} \quad (5)$$

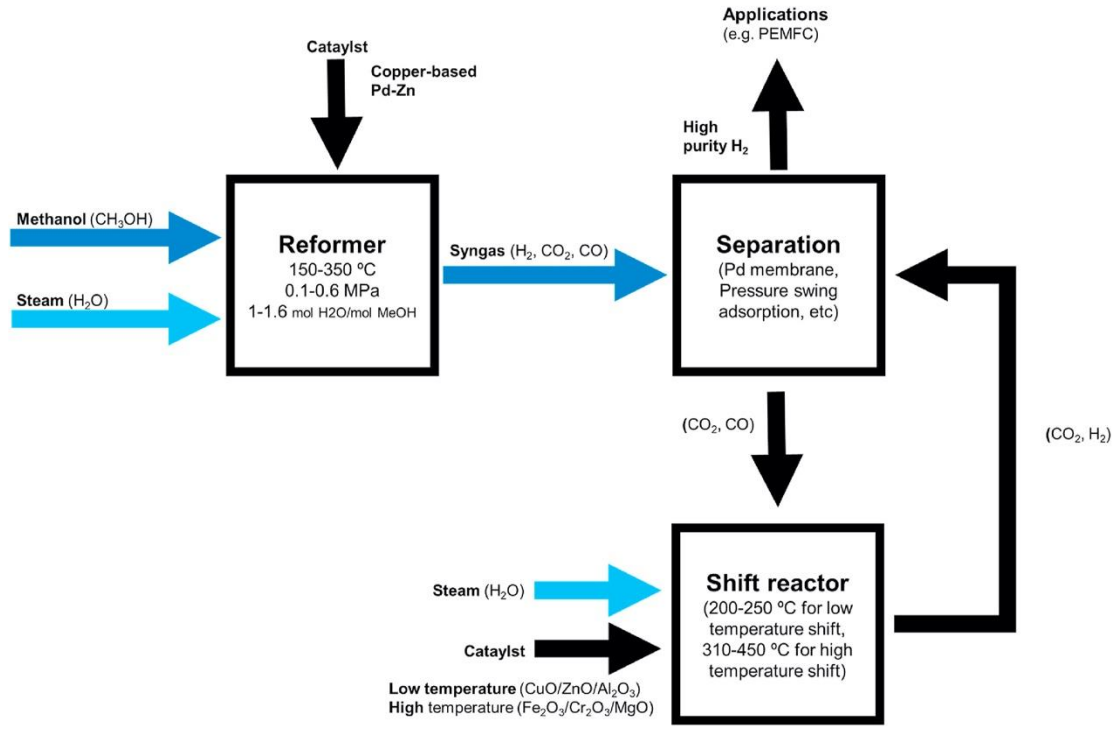


**Figure 4:** Representation of steam reforming of methanol (Adapted from [11]).

### 1.2.4 Partial oxidation of methanol (POM)

Partial oxidation of methanol is an endothermic reaction shown in reaction 5. POM is also important for formaldehyde synthesis with high selectivity. There are three industrial formaldehyde production processes namely Silver Catalyst process, BASF process and Formox process. The former two use Ag catalysts at elevated temperatures, 600-720˚C at ambient pressures while the later uses FeMo catalysts at lower temperatures of 250-400˚C [11, 14, 15]. The main reaction of formaldehyde synthesis are listed in reactions (6-9).

$$CH_3OH + \frac{1}{2}O_2 \longrightarrow 2H_2 + CO_2 \qquad \Delta°H_{rxn} = -192.2 \text{ kJ mol}^{-1} \text{ (6)}$$

$$CH_3OH \longrightarrow CH_2O + H_2 \qquad \Delta°H_{rxn} = 84 \text{ kJ mol}^{-1} \text{ (7)}$$

$$H_2 + \frac{1}{2}O_2 \longrightarrow H_2O \qquad \Delta°H_{rxn} = -243 \text{ kJ mol}^{-1} \text{ (8)}$$

$$CH_3OH + \frac{1}{2}O_2 \longrightarrow CH_2O + H_2O \qquad \Delta°H_{rxn} = -159 \text{ kJ mol}^{-1} \text{ (9)}$$

## 1.3 Copper catalysts in the methanol industry

Copper catalysts are among the most studied catalyst families in the methanol industry as $Cu/ZnO/Al_2O_3$ is the classical industrial methanol synthesis catalyst and Cu-based metal oxides are extensively used for methanol reforming processes [16,17]. The extensive use of copper catalysts in the methanol industry also brings attention to mechanistic studies and studies on understanding the selectivity of these catalysts. There have been numerous spectroscopic studies utilizing in-situ Fourier Transform Infrared Spectroscopy (in-situ FTIR), Diffuse Reflectance Infrared Fourier Transform spectroscopy (DRIFTS), and Temperature Programmed Desorption (TPD) on Cu-based catalysts such as CuO, $Cu_2O$, $Cu/SiO_2$, Cu/ZnO, $Cu/ZnO/Cr_2O_3$, $Cu/ZrO_2$, Cu-ZSM-5 and etc. [18-29] and other studies utilizing Reflection Adsorption Infrared Spectroscopy (RAIRS/IRAS), High Resolution Electron Energy Loss Spectroscopy (HREELS), and TPD on Cu-single crystals such as Cu(100), Cu(111), and

Cu(110) [7, 30-38] as well as computational Density Functional Theory (DFT) studies [39, 40]. These studies were focused on methanol, formaldehyde, formic acid and other surface intermediates represented in Figure 5 [41] associated with heterogenous catalytic methanol transformations.

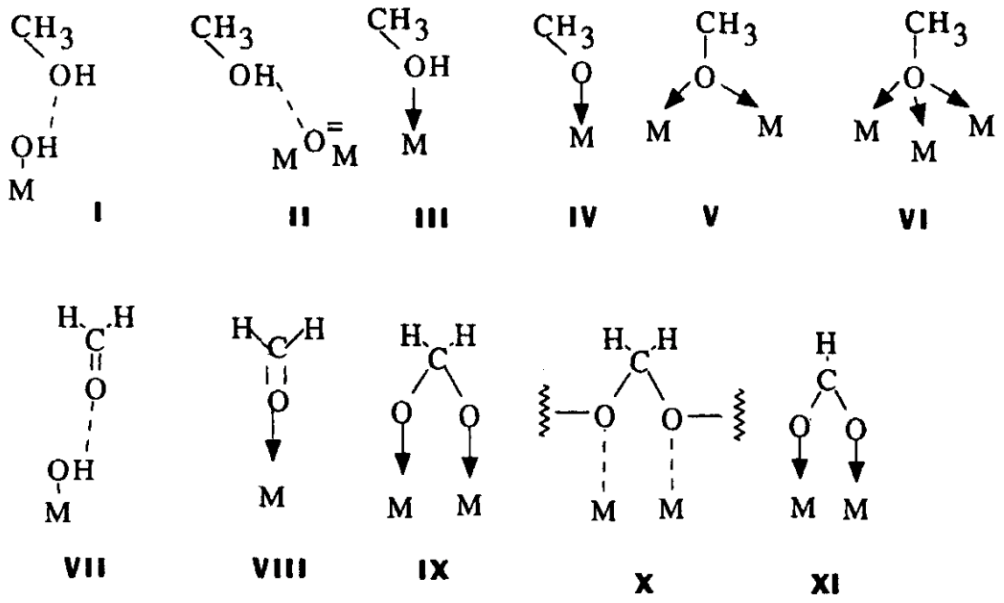


**Figure 5:** Structures of adsorbed species observed in methanol transformations (Adapted from [41]).

Some of the important species in Figure 5 are structure IV (methoxy), structure VII (molecularly adsorbed formaldehyde), structure IX (dioxymethylene, DOM), and structure XI (bidentate formate). There are many different proposed reaction mechanisms for methanol reactions in the literature [18-41] and the dioxymethylene-intermediate mediated pathway is shown in Figure 6.

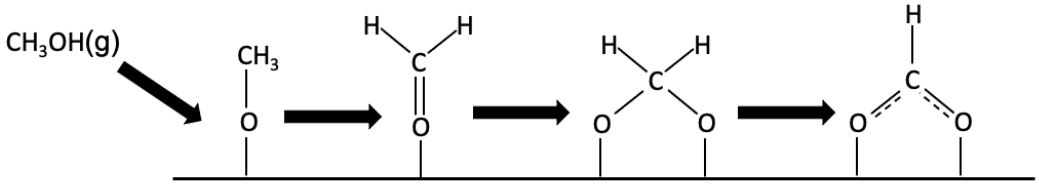


**Figure 6:** DOM-mediated methanol decomposition pathway.

## 1.4 Model Catalysts

The aforementioned spectroscopic studies have either been performed on complex polycrystalline catalysts revealing poorly defined surface chemistry or on single crystals revealing homogenous and well-defined surfaces. Using polycrystalline catalysts allows mechanistic studies to be performed under industrially relevant temperatures and pressures but the complex surface chemistry of these catalysts limits the understanding of reaction mechanisms resulting in one of the essential challenges in heterogeneous catalysis which is the identification of the electronic nature of the catalytic active sites and determination of site-dependent catalytic reaction mechanisms. On the other hand, using single crystals with well-defined surfaces allows mechanistic studies to be conducted under ultra-high vacuum (UHV) conditions and cryogenic temperatures which are far from industrial reaction conditions creating the so-called "materials gap" and the "pressure gap" between conventional planar single-crystals that are often studied under ultra-high vacuum (UHV)/cryogenic conditions and complex mesoporous technical catalyst which are used under elevated temperatures and pressures.

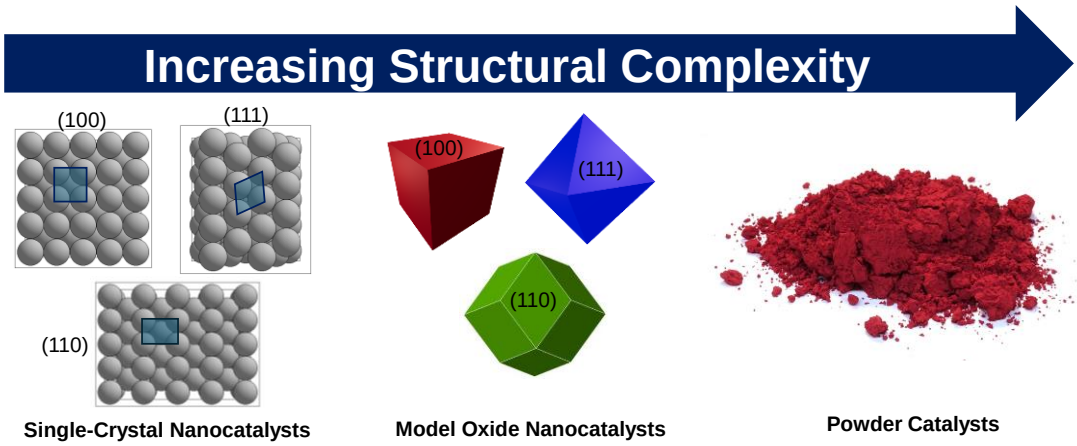


**Figure 7:** Progression of structural complexity from single crystal planar model catalysts to shape-defined nanocrystal model catalysts, and mesoporous polycrystalline powder catalysts.

Model catalysts provide a versatile opportunity for bridging the gap between single-crystal and complex technical catalysts by eliminating materials and pressure gaps as visualized in Figure 7. Model catalysts have atomically well-defined surfaces as well as well-defined types and numbers of surface crystal defects (point defects such as corners and extended line defects such as edges) that can be studied under ambient conditions allowing mechanistic studies. Shape-defined nanocrystals are among the well-studied model catalysts. These catalysts tend to expose different facets depending on their morphology enabling the investigation of "structure sensitivity" and "structure-functionality" relationships in heterogenous catalysis without the need for UHV or cryogenic temperatures [42-44].

### 1.4.1 Shape-defined $Cu_2O$ as a model catalyst

Shape-defined $Cu_2O$ nano/micro-crystal model catalysts [43-46] were selected as the model catalysts that were used in this study due to relevancy of Cu-based catalysts in methanol industry. Shape-defined $Cu_2O$ catalysts showed morphology-dependent catalytical activity in a variety of reactions such as CO oxidation, water gas shift (WGS) reaction, $CO_2$ photoreduction, etc. [47-50]. Thus, they are also expected to show structure-dependent activity during methanol decomposition. Some of the commonly investigated $Cu_2O$ nanocrystals are cubic, octahedral, and dodecahedral crystals exposing different crystal facets (100), (111), and (110) as shown in Figure 8, respectively.

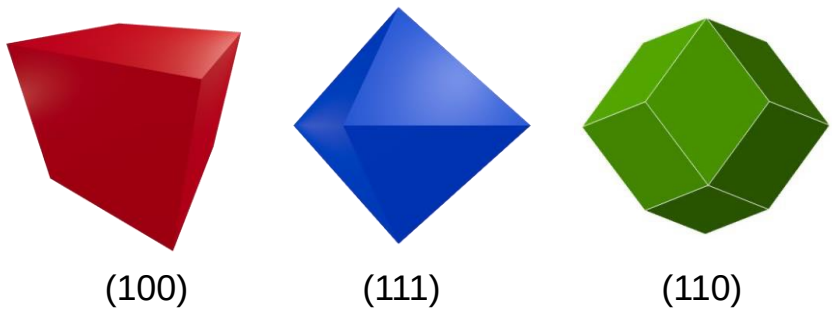


**Figure 8:** Exposed facets of shape-defined $Cu_2O$ nanocrystals.

$Cu_2O$ has a cubic crystallographic structure shown in Figure 9 in which Cu atoms are oriented in a face-centered cubic (FCC) structure and O atoms are in a body-centered cubic (BCC) structure. In the bulk, Cu atoms are two-fold coordinated to oxygen atoms and O atoms are four-fold coordinated to copper atoms [51,52]

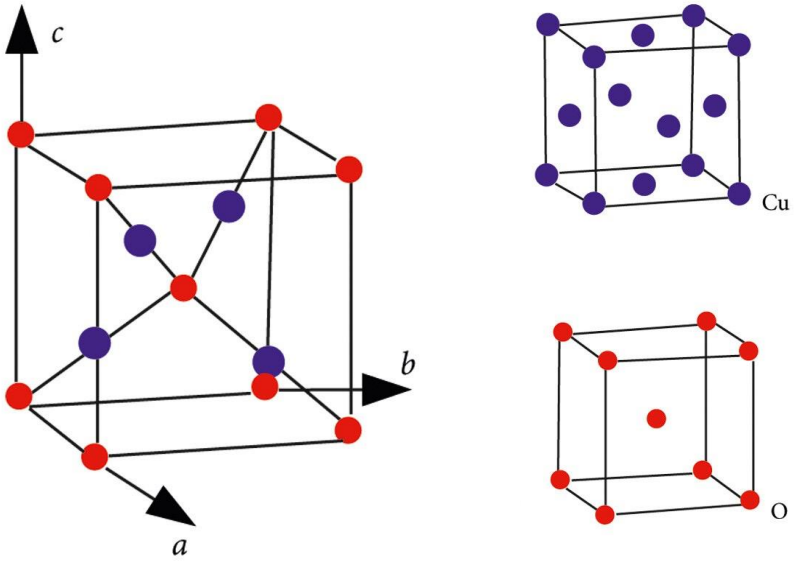


**Figure 9:** $Cu_2O$ unit cell and cation/anion packings inside the unit cell (Adapted from [51]).

The orientations and coordination of the Cu and O surface sites are also morphology dependent as shown in Figure 10 [53].

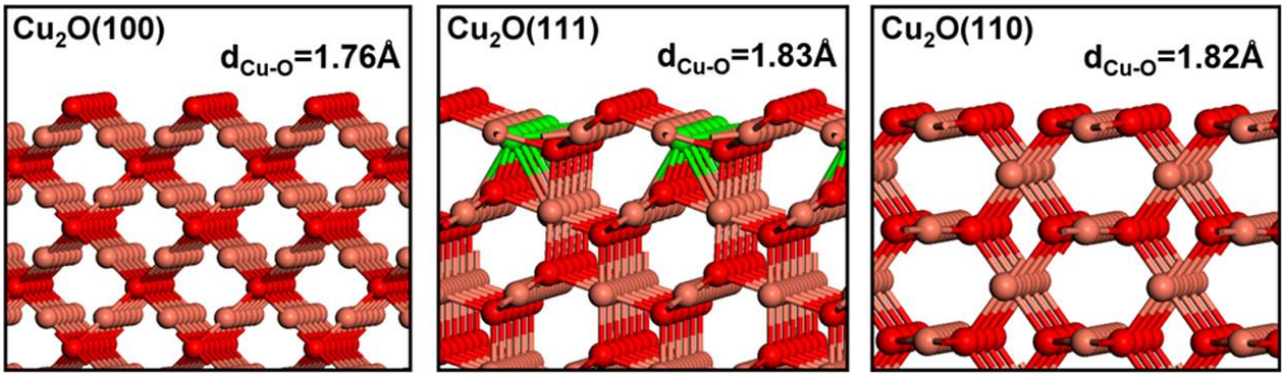


**Figure 10:** Surface structures of Cu2O (100), (111), and (110). O, $Cu_{CSA}$, and $Cu_{CUS}$ are represented by red, brick-red, and green balls (Adapted from [53]).

On $Cu_2O$ (100), the topmost layer consists of two-fold coordinated $O_{2c}$ species and the second layer consists of two-fold coordinatively saturated $Cu_{CSA}$ species. On $Cu_2O$ (111), the topmost layer consists of three-fold coordinated $O_{3c}$ species and the second layer consists of twofold coordinatively-saturated $Cu_{CSA}$ species and one-fold coordinatively unsaturated $Cu_{CUS}$ species. On $Cu_2O$ (110), the topmost layer consists of three-fold coordinated $O_{3c}$ species and twofold coordinated saturated $Cu_{CSA}$ atoms, and the second layer consists of twofold coordinated saturated $Cu_{CSA}$ atoms [44, 54]. The surface coordination of different morphologies are summarized in Table 1.

| Nanocrystals | Exposed Crystal Planes | Topmost Layer | Second Layer | d(Cu-O) (Å) |
|---|---|---|---|---|
| c-$Cu_2O$ | $Cu_2O$ (100) | 2-fold-coordinated $O_{2c}$ | 2-fold-coordinated $Cu_{CSA}$ | 1.76 |
| o-$Cu_2O$ | $Cu_2O$ (111) | 3-fold-coordinated $O_{3c}$ | 2-fold-coordinated $Cu_{CSA}$ (75%) 1-fold-coordinated $Cu_{1c}$ (25%) | 1.83 1.91 |
| d-$Cu_2O$ | $Cu_2O$ (110) | 3-fold-coordinated $O_{3c}$ 2-fold-coordinated $Cu_{CSA}$ | 2-fold-coordinated $Cu_{CSA}$ | 1.82 |
| Bulk $Cu_2O$ | | 4-fold-coordinated $O_{CSA}$ 2-fold-coordinated $Cu_{CSA}$ | | 1.85 |

**Table 1:** Surface coordination of c/o/d-$Cu_2O$ ( Adapted from [44]).

Overall, this study aims to serve as a bridge between surface science studies on Cu single crystals and Cu-based polycrystalline catalysts during methanol decomposition. Shape-defined cubic and octahedral $Cu_2O$ nanocrystals were selected as the model catalysts for this study.

Their structures were characterized by various ex-situ methods. Methanol thermal decomposition and formaldehyde thermal decomposition were studied by utilizing in-situ FTIR and TPD techniques. Lastly, the findings were used to elucidate the "structure sensitivity" and "structure-functionality" and relationship between c-$Cu_2O$ and o-$Cu_2O$ during methanol decomposition.

# 2 Experimental

## 2.1 Material Synthesis

### 2.1.1 Synthesis of shape defined c-$Cu_2O$ (100):

All of the precursors used in the $Cu_2O$ synthesis namely, $CuCl_2 \cdot 2H_2O$ (ACS reagent, ≥99.0%), NaOH (puriss., meet analytical specification of Ph. Eur., BP, NF, E524, 98-100.5%, pellets), L-Ascorbic Acid ($C_6H_8O_6$, (2*R*)-2-[(1*S*)-1,2-dihydroxyethyl]-3,4-dihydroxy-2*H*-furan-5-one) (99%) were purchased from Sigma Aldrich and used without further purification. In the synthesis of c-$Cu_2O$, 287 mL of 0.1 M $CuCl_2$ aqueous solution was prepared in a beaker equipped with a thermal jacket connected to a water circulator (CLS CLRC-08C Refrigerated Circulator), and the synthesis solution inside the beaker was continuously stirred at 700 rpm throughout the synthesis. The temperature of the water circulator was set to 25 ± 0.2˚C (Temperature values were recorded at two different points using thermocouples for accuracy). After a stirring period of 5 min, 21 mL 0.2 M NaOH aqueous solution was added to the $CuCl_2$ solution using an electronic syringe pump (Syringe Pump Specson Instruments 200-X) with an injection rate of 1 mL/min and stirred for 30 min. Then, 14 mL of 0.1 M L-Ascorbic Acid aqueous solution was added with an injection rate of 1 mL/min into the reaction mixture and stirred for 2 h. The collected samples were centrifuged (6000 rpm, 5 min) and washed 5 times

with distilled water and 2 times with absolute ethanol (ACS, ISO, Reagent, Ph. Eur., for analysis ≥99.9%). Finally, the collected precipitate was dried in an oven at 80˚ for 12 h [55, 56].

### 2.1.2 Synthesis of shape defined o-$Cu_2O$ (111):

All of the precursors used in the $Cu_2O$ synthesis namely, $CuCl_2{\cdot}2H_2O$ (ACS reagent, ≥99.0%), NaOH (puriss., meets analytical specification of Ph. Eur., BP, NF, E524, 98-100.5%, pellets), L-Ascorbic Acid (99%) and Polyvinylpyrrolidone (PVP, powder, average Mw ~29,000) were purchased from Sigma Aldrich and used without further purification. In the synthesis of o-$Cu_2O$, 100 mL of 0.1 M $CuCl_2$ aqueous solution was prepared in a jacketed beaker connected to a water circulator (CLS CLRC-08C Refrigerated Circulator) and the solution was continuously stirred at 700 rpm throughout the synthesis. The temperature of the water circulator was set to 35˚C. After a stirring period of 5 min, 3.33 g of PVP was added to the reaction mixture and stirred until completely dissolved. Then, 10 mL 2 M NaOH aqueous solution was added to the reaction mixture using an electronic syringe pump (Syringe Pump Specson Instruments 200-X) with an injection rate of 1 mL/min and mixed further for 30 min. After that, 10 mL of 0.6 M L-Ascorbic Acid aqueous solution was added with an injection rate of 0.3 mL/min into the reaction mixture and stirred for 3 h. The collected samples were centrifuged (6000 rpm, 5 min) and washed 5 times with distilled water and 2 times with absolute ethanol (ACS, ISO, Reagent, Ph. Eur., for analysis ≥99.9%). Finally, the collected precipitate was dried in an oven at 80˚ for 12 h [57].

### 2.1.3 Etching and cleaning of surface capping agents on o-$Cu_2O$ (111):

The capping ligands on o-$Cu_2O$ were removed by controlled oxidative treatment performed in a custom-made flow-reactor setup. Typically, 50-60 mg of the sample was placed in the quartz reactor and pure Ar(g) (99.995%, Linde GmbH) was purged with a flow rate of 60 sccm until the temperature became 50˚C. Then, the stream was switched to a mixture of $C_3H_6$ (99.5%,

Mitan) + $O_2$ (99.5%, Linde GmbH) + $N_2$ (99.99%, Linde GmbH) gas mixture ($C_3H_6$:$O_2$:$N_2$ = 2:1:22) with a flow rate of 200 sccm. The sample was purged with this gas mixture for 30 min at 50˚C and then, heated to 200˚C with a heating rate of 5 ˚C/min and kept for another 60 min. After that, the stream was switched to pure Ar(g) gas at 60 sccm and cooled down to room temperature with a cooling rate of 10˚C/min [58]. The morphologies of the o-$Cu_2O$ nanocrystals were preserved in this process (Appendix A).

## 2.2 Material Characterization Methods

### 2.2.1 Scanning Electron Microscopy (SEM):

SEM images were acquired using FEI QUANTA 200 FEG ESEM equipped with a Schottky field emission gun (FEG). SEM samples were prepared by transferring tiny amounts of sample powder onto the sticky carbon tape that was mounted on an aluminum SEM stub. For most of the samples, the voltage was selected as 20.00 kV, and the spot size was 3. For determining the particle size distribution and average particle size values, ImageJ software was used.

### 2.2.2 X-Ray Diffraction (XRD):

The crystallographic structures of the samples were determined using a PANalytical (X'Pert PRO) multipurpose X-ray diffractometer equipped with a Cu Kα X-ray source (40 kV, 45 mA, λ = 1.5405 Å). Powder samples were placed in the middle of a silicon single-crystal sample holder and pressed. The samples were scanned in the range of 20-80˚ with 0.01 step resolution and 100 s per step . International Centre for Diffraction Database (ICDD) crystal structure library was used to identify the crystal structure.

### 2.2.3 X-Ray Absorption Near Edge (XANES) and Extended X-Ray Absorption Fine Structure (EXAFS) measurements:

XANES and EXAFS measurements were performed at the XRF beamline of the Synchrotron-light for Experimental Science and Applications in the Middle East (SESAME) located in Allan, Jordan operating at 2.5 GeV. BM08-XAFS/XRF (X-ray Absorption Fine Structure/X-ray Fluorescence) which has an energy range of 4.7-30 keV energy range was used. Before the experiments pellets were prepared by mixing the desired amount of sample with PVP. The ratios of sample/PVP were calculated using XAFSmass software and listed in Table 2.

| Sample Name | Sample Amount (mg) | PVP Amount (mg) |
|---|---|---|
| Commercial $Cu_2O$ | 7 | 83 |
| $CuCl_2 \cdot 2H_2O$ | 10 | 80 |
| c-$Cu_2O$ | 7 | 83 |
| o-$Cu_2O$ | 7 | 83 |

**Table 2:** XANES/EXAFS sample preparation amounts.

Measurements were performed in transmission mode for Cu-K edge (8980 eV). 4 scans for collected for each sample to obtain a high signal-to-noise (S/N) ratio and the spectral parameters are shown in Table 3.

| Energy Range (keV) | Resolution (keV) |
|---|---|
| 8.885-8.965 | 0.001 |
| 8.965-8.992 | 0.0002 |
| 8.992-9.018 | 0.0005 |

| | |
|---|---|
| 9.018-9.85 | 0.03 |

**Table 3:** XANES/EXAFS spectra acquisition parameters.

The analysis of the XANES/EXAFS data was performed using the Athena software.

### 2.2.4 Attenuated Total Reflectance Infrared Spectroscopy (ATR-IR):

ATR-IR spectra were measured by a Bruker ALPHA FTIR spectrometer, equipped with a Platinum ATR module. A small amount of sample was placed onto the diamond crystal and pressed with the adjustable pressure arm. The spectra were recorded in the 400-4000 $cm^{-1}$ range by averaging 128 scans with a resolution of 4 $cm^{-1}$ and a background measurement was recorded before each measurement.

### 2.2.5 X-Ray Photoelectron Spectroscopy (XPS):

Electronic structures of the samples were determined using a SPECS PHOIBOS hemispherical energy analyzer equipped with a monochromatic Al-Kα X-ray source (Excitation energy: 1486.6 eV). A flood gun (13 $\mu$A, 0.9 eV) was used for charge compensation. The powder samples were pressed to make small pellets and placed on an aluminum foil bed mounted on the sample holders by sticky carbon tape. Such pellets led to limited differential charging. XPS binding energy (B.E.) values were referenced with respect to the Cu 2p satellite peak at 944.2 eV, which is present for both $Cu^{+}$ and $Cu^{2+}$. The quantification of the elements were performed based on the areas under major peaks: Cu 2p, O 1s, C 1s, N 1s, and Na 1s. The relative sensitivity factors (RSF) used were 25.39, 2.93, 1.0, 1.8, and 8.52 for Cu 2p, O 1s, C 1s, N 1s, and Na 1s, respectively.

### 2.2.6 $H_2$-Temperature Programmed Reduction ($H_2$-TPR):

$H_2$-TPR experiments were performed in a custom-made flow-reactor setup connected to a quadrupole mass spectrometer (QMS, Stanford Research Systems, RGA 200). Firstly, 150 mg

of quartz wool was placed inside the quartz reactor. Then, 100 mg of catalyst (c-$Cu_2O$ or o-$Cu_2O$) was loaded onto the quartz wool inside the reactor. Initially, the catalysts were heated under $N_2$ (g) flow at 100 sccm to 200˚C with a ramp rate of 5˚C/min and kept at 200˚C for 60 min. After that, the catalysts were cooled down to 50˚C in $N_2$ (g) flow. This pretreatment was performed to clean the surfaces of the catalysts and the removal of the adsorbed water. After the pretreatment, the gas was switched to 5% $H_2$/Ar (g) (Linde GmbH) flow at 25 sccm for 240 min to stabilize the $H_2O$ (m/z=18) QMS signal. After signal stabilization, the catalyst was heated to 800˚C with a ramp rate of 5˚C/min, and the reduction process was monitored by following the $H_2O$ (m/z=18) signal by QMS. After reaching 800˚C, the stream was switched to $N_2$ (g) flow at 100 sccm and the catalysts was cooled down. The reduction profiles were plotted as $H_2O$ (m/z=18) QMS intensity as a function of temperature.

## 2.3 Functional Characterization:

### 2.3.1 In-situ Fourier Transform Infrared Spectroscopy (in-situ FTIR):

In-situ FTIR Spectroscopy measurements were carried out with a Bruker Tensor 27 FTIR spectrometer equipped with a batch-type custom-design spectroscopic reactor and a liquid nitrogen-cooled mercury cadmium telluride (MCT) mid-IR detector. The spectra were acquired in transmission mode. The samples were pressed onto a lithographically etched-tungsten grid. Then, the grid was placed into the in-situ FTIR reactor and evacuated. Before the experiments, each sample was heated to 250˚C with a ramp rate of 5 sec/˚C and kept for 30 min under vacuum ($10^{-3}$ Torr). Background measurements were collected under vacuum ($10^{-6}$ Torr) during the cool down period at every 50˚C between 250 - 50˚C. At 50˚C desired amount of CO (g) (>99%, Linde GmbH), methanol (≥99.9%, suitable for immunofluorescence, HPLC, Sigma Aldrich), or formaldehyde vapor (generated by heating solid paraformaldehyde was introduced to the system and the sample was saturated with CO (g), methanol, or formaldehyde for 30 min. Gas

pressures were measured with a MKS Baratron 626A capacitance manometer operating within 0.1-1000 Torr Then, the vapor was evacuated, and sample IR spectra were acquired at 50 °C in vacuum ($10^{-6}$ Torr). After that, the sample was heated to 100, 150, 200, and 250 °C in vacuum with a ramp rate of 5 sec/°C step by step, and at each temperature, an IR measurement was taken. All in-situ IR spectroscopic measurements were taken with 256 scans and a resolution of 4 $cm^{-1}$.

#### 2.3.1.1 Methanol Adsorption:

16 Torr of methanol (≥99.9%, suitable for immunofluorescence, HPLC, Sigma Aldrich) vapor was dosed into the manifold and reactor chamber.

#### 2.3.1.2 Formaldehyde Adsorption:

Solid paraformaldehyde was heated with heating tapes to generate gaseous formaldehyde. 5.5 Torr of gaseous formaldehyde was dosed into the manifold and the reactor chamber.

#### 2.3.1.3 CO Adsorption:

In contrast to the above-mentioned experimental method for in-situ FTIR experiments, for CO adsorption experiments, background IR spectrum measurement was only recorded at 50 ˚C after the pretreatment and the sample IR spectrum measurement was performed at this temperature only. Before the sample IR spectrum acquisition, 20 Torr of CO(g) was dosed into the manifold and reactor chamber followed by evacuation.

### 2.3.2 Temperature Programmed Desorption (TPD):

TPD experiments were performed in the in-situ spectroscopic reactor coupled to a quadrupole mass spectrometer (QMS, Stanford Research Systems, RGA 200). The samples were pressed into a tungsten grid. Then, the grid was placed into the in-situ FTIR reactor set-up and evacuated. Before the experiments, each sample was heated to 250˚C with a ramp rate of 5 sec/˚C and kept for 30 min under vacuum then, cooled down to 50˚C. At 50˚C desired amount

of methanol (16 Torr, ≥99.9%, suitable for immunofluorescence, HPLC, Sigma Aldrich), or formaldehyde vapor (5.5 Torr, generated by heating solid paraformaldehyde) was introduced to the system and the sample was saturated with methanol, or formaldehyde for 30 min. Then, the vapor was evacuated until the reactor pressure reached ~1 x $10^{-6}$ Torr. The sample was then heated to 700˚C with a ramp rate of 5 sec/˚C and the evolving gaseous species were monitored by on-line QMS using the following mass-to-charge ratio (m/z) channels: 2, 18, 28, 30, 31, and 44.

### 2.3.2.1 Blank TPD:

In the blank TPD measurements, no gas was introduced to the system and the desorption product during sample heating was analyzed using the exact procedure described in section

# 3 Results and Discussion

## 3.1 Particle size and shape analysis via SEM:

SEM was used to analyze the shape and ImageJ software was used to determine the average particle size of the synthesized nanoparticles. Figure 11a,b and c shows the SEM images of the c-$Cu_2O$ samples. These images showed that the desired cubic morphology was obtained, and the samples expose (100) facets. The ImageJ analysis of the SEM images (Figure *11*d) showed that the average particle size for the c-$Cu_2O$ samples were 90 ± 16 nm, and a homogenous size distribution was obtained.

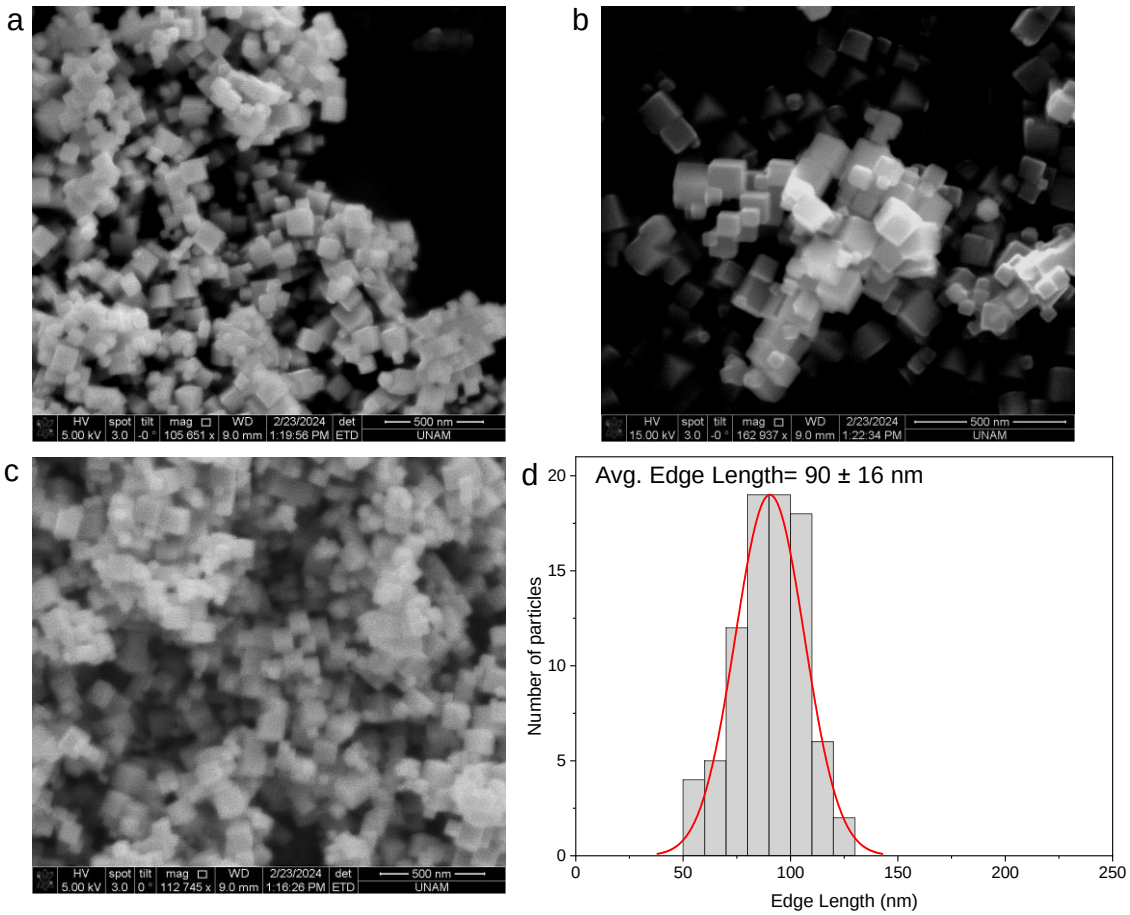


**Figure 11**: a-c) SEM images of c-$Cu_2O$ d) ImageJ analysis.

Figure 12a,b and c shows the SEM images of the o-$Cu_2O$ samples. These images showed that the desired octahedral morphology was obtained, and the samples expose (111) facets. ImageJ analysis of the SEM images (Figure 12d) showed that the average particle size for the o-$Cu_2O$ samples were 428 ± 45 nm and the size distribution between different batches were not as homogenous as it was for c-$Cu_2O$ samples.

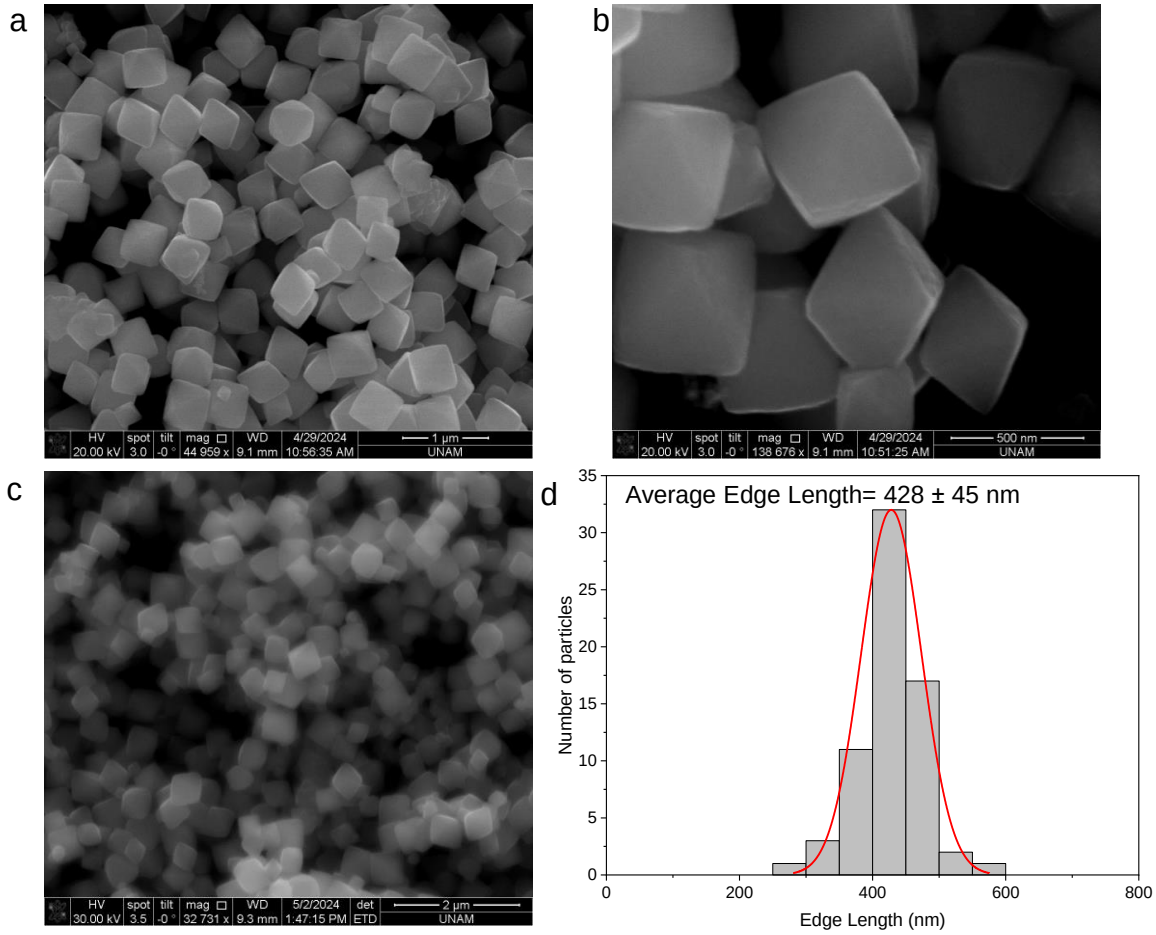


**Figure 12:** a-c) SEM images of o-$Cu_2O$ d) ImageJ analysis.

## 3.2 Crystal structure analysis via XRD:

The XRD patterns of c-$Cu_2O$ and o-$Cu_2O$ were analyzed to identify their crystal structures and degree of crystallinity. Figure 13 shows the XRD patterns of the synthesized nanoparticles, commercial $Cu_2O$ (97%, Acros Organics), and the $Cu_2O$ reference (ICDD No. 01-080-3714) obtained from the ICDD database. It is seen that all of the diffraction peaks match well with the

cubic $Cu_2O$ and no other peaks related to CuO or metallic copper are present in the diffractograms. In addition to that, the diffraction patterns of c-$Cu_2O$ and o-$Cu_2O$ match perfectly with that of the commercial $Cu_2O$ showcasing the purity of the crystal structures. Furthermore, the sharpness of the obtained diffraction peaks indicates the high degree of crystallinity of the synthesized nanoparticles. Thus, the synthesized nanoparticles have a highly pure cubic $Cu_2O$ crystal structure in their bulk with a remarkably high crystallinity consistent with a single crystal-like structure.

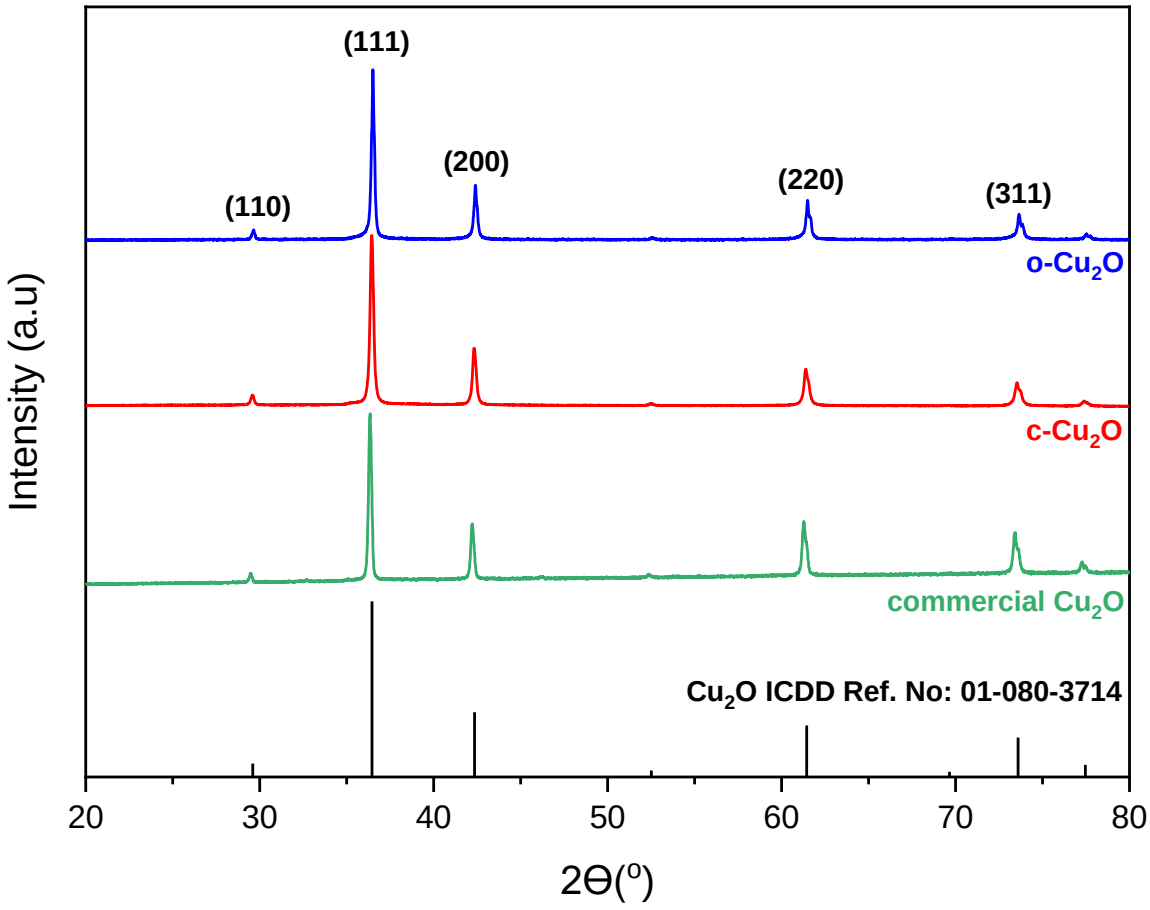


**Figure 13:** XRD diffraction pattern of commercial $Cu_2O$, c-$Cu_2O$, o-$Cu_2O$, and $Cu_2O$ ICDD Ref. No:01-080-3714.

## 3.3 Analysis of the bulk oxidation state and coordination environment via XANES and EXAFS

XANES and EXAFS measurements were performed to obtain information about the bulk oxidation state and the coordination environment of c-$Cu_2O$ and o-$Cu_2O$. The Cu K-edge XANES spectra of Cu-based catalysts are composed of a well-defined edge peak due to the dipole allowed 1s→4p electronic transition 8983-8984 eV and a pre-edge feature due to the dipole forbidden 1s→3d electronic transition 8976-8979 eV [59]. Figure 14a and b show the Cu K-edge XANES spectra of commercial $Cu_2O$, $CuCl_2{\cdot}2H_2O$, o-$Cu_2O$, c-$Cu_2O$, and metallic Cu foil. These results indicate that o-$Cu_2O$ and c-$Cu_2O$ have a Cu oxidation state of +1 as expected.

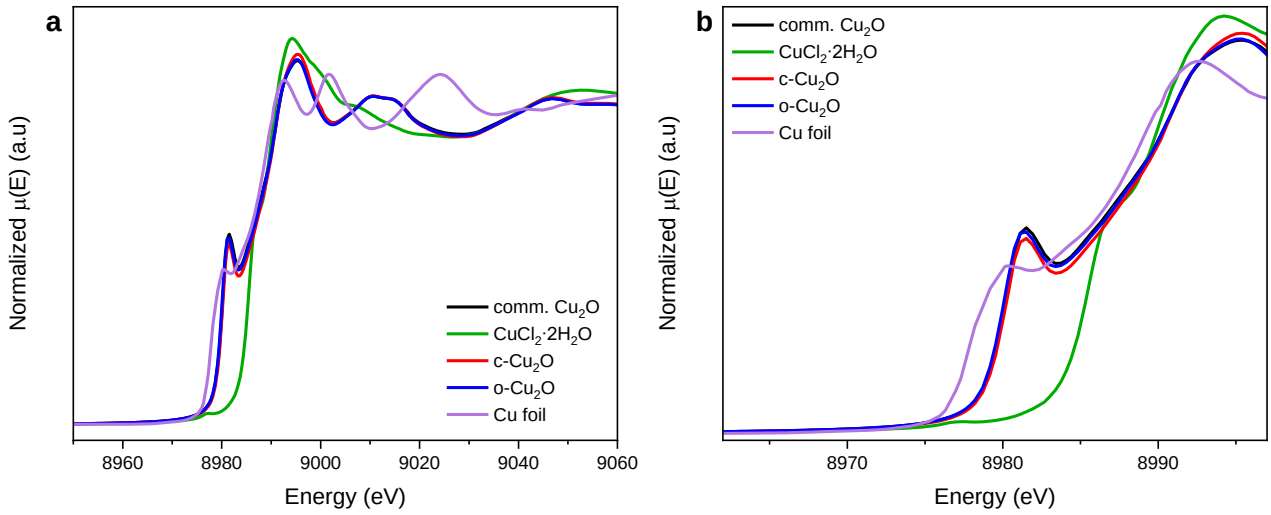


**Figure 14:** XANES spectra of Cu K-edge for commercial $Cu_2O$, $CuCl_2{\cdot}2H_2O$, o-$Cu_2O$, c-$Cu_2O$, and Cu foil.

Figure 15 shows the Cu K-edge EXAFS spectra of commercial $Cu_2O$, $CuCl_2{\cdot}2H_2O$, o-$Cu_2O$ and c-$Cu_2O$. When the EXAFS spectra are investigated, it is seen that the spectra align perfectly for commercial $Cu_2O$, o-$Cu_2O$ and c-$Cu_2O$ indicating that the o-$Cu_2O$ and c-$Cu_2O$ have the same coordination environment with commercial $Cu_2O$, where Cu-O and Cu-Cu bond distances are 1.47 and 2.74 Å, respectively [60, 61]. For $CuCl_2{\cdot}2H_2O$, the Cu-O and Cu-Cl bond distances were observed at 1.56 and 1.68 Å, respectively [62]. These results indicate that the bulk

coordination environment and oxidation states of o-$Cu_2O$ and c-$Cu_2O$ align with that of commercial $Cu_2O$ showing that these catalysts have comparable and well-defined lattice structures in their bulk.

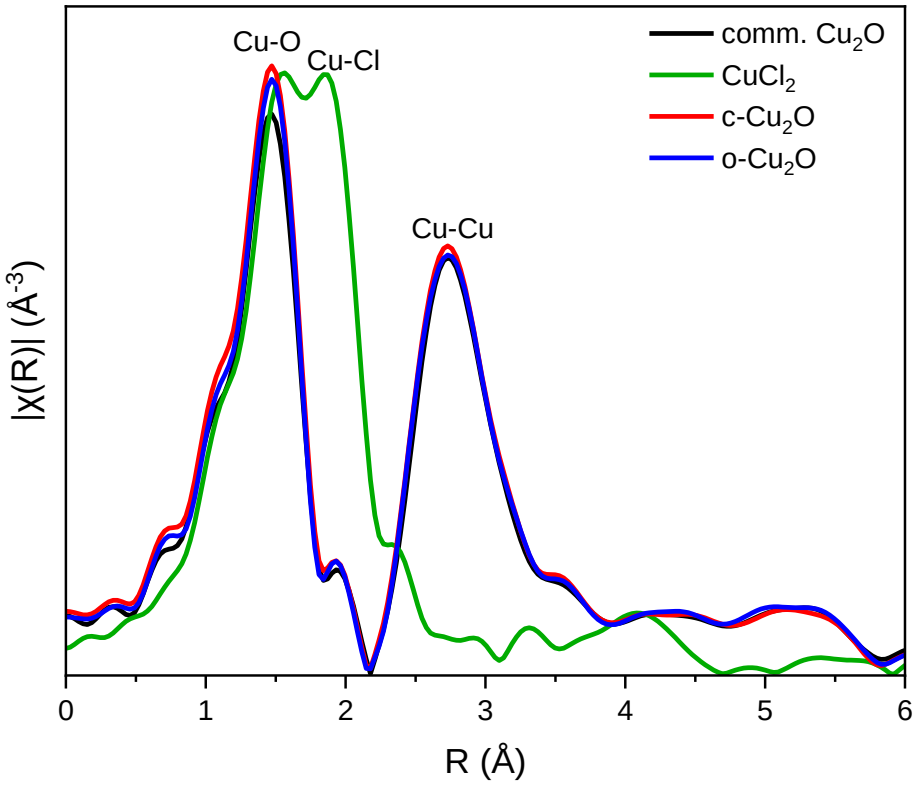


**Figure 15:** Cu K-edge EXAFS spectra of commercial $Cu_2O$, $CuCl_2 \cdot 2H_2O$, o-$Cu_2O$, and c-$Cu_2O$.

## 3.4 Analysis of the residual surface functional groups and bulk oxidation state via ATR-IR:

ATR-IR was used to analyze the residual surface functional groups of the synthesized catalyst which are important to investigate as these surface functionalities can be detrimental for the catalytic activity by covering/blocking surface active sites and altering oxidation states of surface sites. Also, since the depth of penetration of ATR-IR for mid-IR frequencies is approximately 1.5 µm, it provides information about both bulk and surface. Thus, ATR-IR is a useful technique for determining the surface/bulk oxidation state of Cu and if any capping agents/precursors are left on the surface.

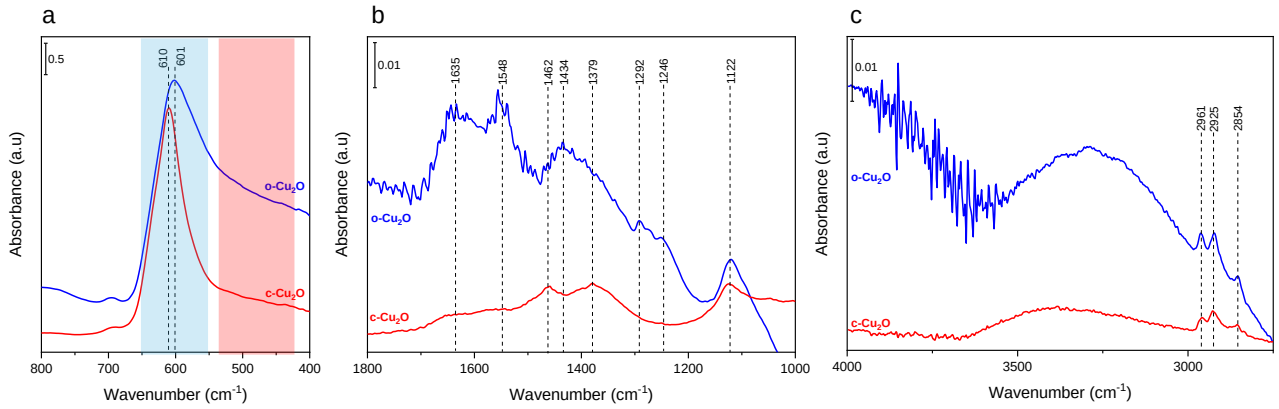


**Figure 16:** ATR-IR spectra of c-$Cu_2O$ and o-$Cu_2O$ a) Cu-O phonon region b) C-H bending region c) C-H and -OH stretching region.

Figure 16a, b and c shows the ATR-IR spectra of c-$Cu_2O$ and o-$Cu_2O$. When the Cu-O phonon region (Figure 16a) is investigated, peaks at 610 $cm^{-1}$ and 601 $cm^{-1}$ (highlighted in blue) are observed for c-$Cu_2O$ and o-$Cu_2O$ respectively and these peaks were attributed to Cu(I)-O stretching mode of $Cu_2O$ [63-68]. Furthermore, the intensity increase of the tail of the Cu-O stretching peak of o-$Cu_2O$ within the 400-550 $cm^{-1}$ region (highlighted in red) might be attributed to the presence of Cu(II)-O as minority species [63-68]. In Figure 16b, ATR-IR peaks located at 1122, 1379, and 1462, $cm^{-1}$ are present for c-$Cu_2O$, and at 1122, 1246, 1292, 1434, 1548, and 1635 $cm^{-1}$ are present for o-$Cu_2O$. The peak located at 1122 is present for both samples and it is attributed to Cu(I)-O stretching mode [63-68]. The peaks located at 1379 and 1462 $cm^{-1}$ for c-$Cu_2O$ can be attributed to $CH_2$ wagging and CH bending/$CH_2$ scissoring modes of the surface-bound ascorbic acid/ascorbate species [69-70]. For o-$Cu_2O$, the peaks located at 1246 and 1292 $cm^{-1}$ can be assigned to C-N bending/$CH_2$ wagging modes, and the peaks located at 1434 and 1635 $cm^{-1}$ can be associated to CH bending and C=O stretching modes of the remaining PVP residues on the o-$Cu_2O$ surface [71-73]. Finally, in Figure 16c, peaks at 2854, 2925, 2961 $cm^{-1}$ and a broad feature between 3000-3600 $cm^{-1}$ are observed for both samples, coming from CH and -OH stretching modes. These results indicate that while the surfaces of the c-$Cu_2O$ and o-$Cu_2O$ model catalysts are not entirely devoid of capping agent residues (i.e.,

-$C_xH_yO_z$) after washing/etching. This point will be discussed in further detail in the next section along with the surface elemental analysis via XPS.

## 3.5 Surface-sensitive elemental and oxidation state analysis via XPS:

XPS is used for the oxidation state and elemental analysis. Figure 17 shows the XPS Survey spectra and Figure 18 illustrates the surface atomic percentage results for c-$Cu_2O$ and o-$Cu_2O$ obtained from the XPS data. A higher amount of carbon is observed for c-$Cu_2O$ as compared to that of o-$Cu_2O$, since c-$Cu_2O$ did not undergo an etching procedure after the synthesis. The presence of carbon on c-$Cu_2O$ and o-$Cu_2O$ samples in XPS results is consistent with the residual surface functionalities that ATR-IR observed in Figure 16. Additionally, trace amounts of N and Na were observed for o-$Cu_2O$ originating from PVP and NaOH used in the synthesis suggesting that Na and N-containing species were successfully removed almost entirely from the c-$Cu_2O$ and o-$Cu_2O$ surfaces at the end of the synthesis procedure (Appendix B and Appendix C).

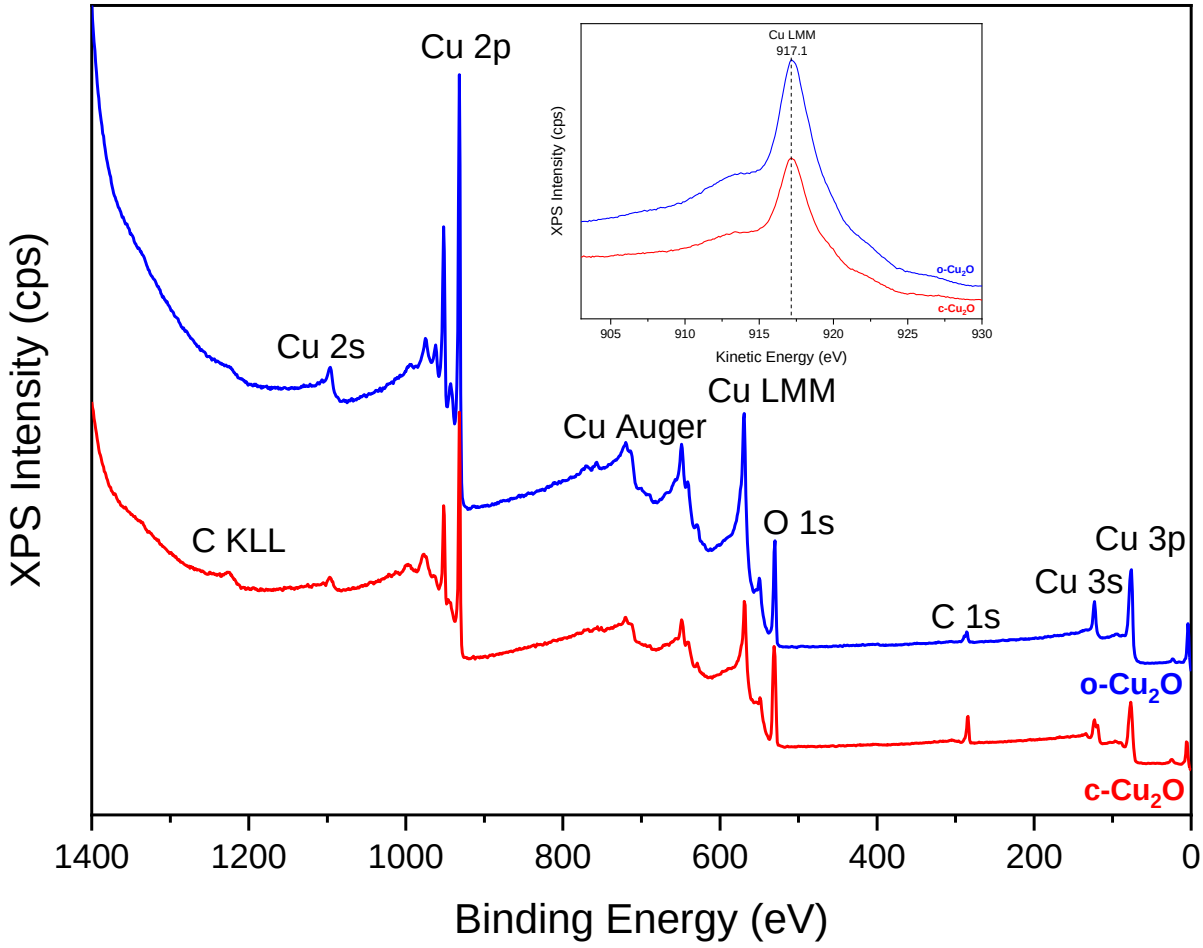


**Figure 17:** XPS survey spectra of c-$Cu_2O$ and o-$Cu_2O$.

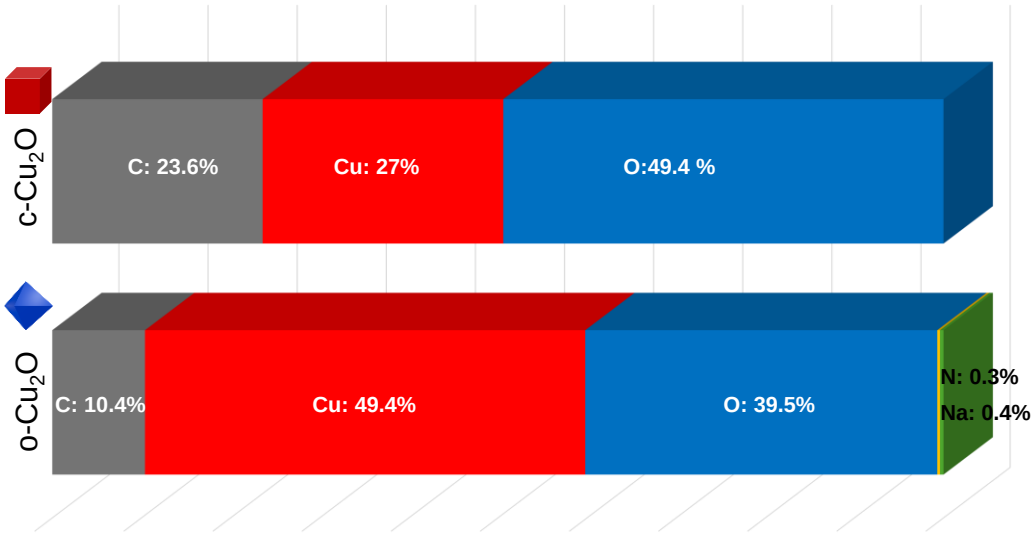


**Figure 18:** Surface atomic percentages obtained from XPS survey spectra of c-$Cu_2O$ and o-$Cu_2O$.

Figure 19 shows the Cu 2p XPS results for c-$Cu_2O$ and o-$Cu_2O$ samples. The peaks located at 932.6 and 932.5 eV (highlighted in blue ) for c-$Cu_2O$ and o-$Cu_2O$ belong to the Cu $2p_{3/2}$ state of $Cu^+$, while the shoulder peak at 935.2 eV (highlighted in red) for o-$Cu_2O$ belongs to the Cu $2p_{3/2}$ state of $Cu^{2+}$ [74-78]. The satellite peak at 944.2 eV (highlighted in green) is a feature that is present for both $Cu^+$ and $Cu^{2+}$, thus it is not useful for oxidation state analysis. On the other hand, the satellite peaks located at 946.7 (highlighted in blue) and 941.1 eV (highlighted in red) are very distinct features for distinguishing the oxidation state. The satellite peak located at 946.6 eV belongs to $Cu^+$ state [74-78] and is present for both samples while the satellite peak located at 941.1 eV is due to $Cu^{2+}$ state [74-78] and is predominantly observed for o-$Cu_2O$. The presence of this satellite together with the shoulder peak located at 935.2 eV for o-$Cu_2O$ indicates the presence of a $Cu^{2+}$ minority species on the o-$Cu_2O$ surface, which is rather elusive to detect via bulk-sensitive techniques and might be linked to the differences in the catalytic behavior of o-$Cu_2O$ as opposed to c-$Cu_2O$ where the latter surface has insignificant amounts of $Cu^{2+}$ surface species [74-78].

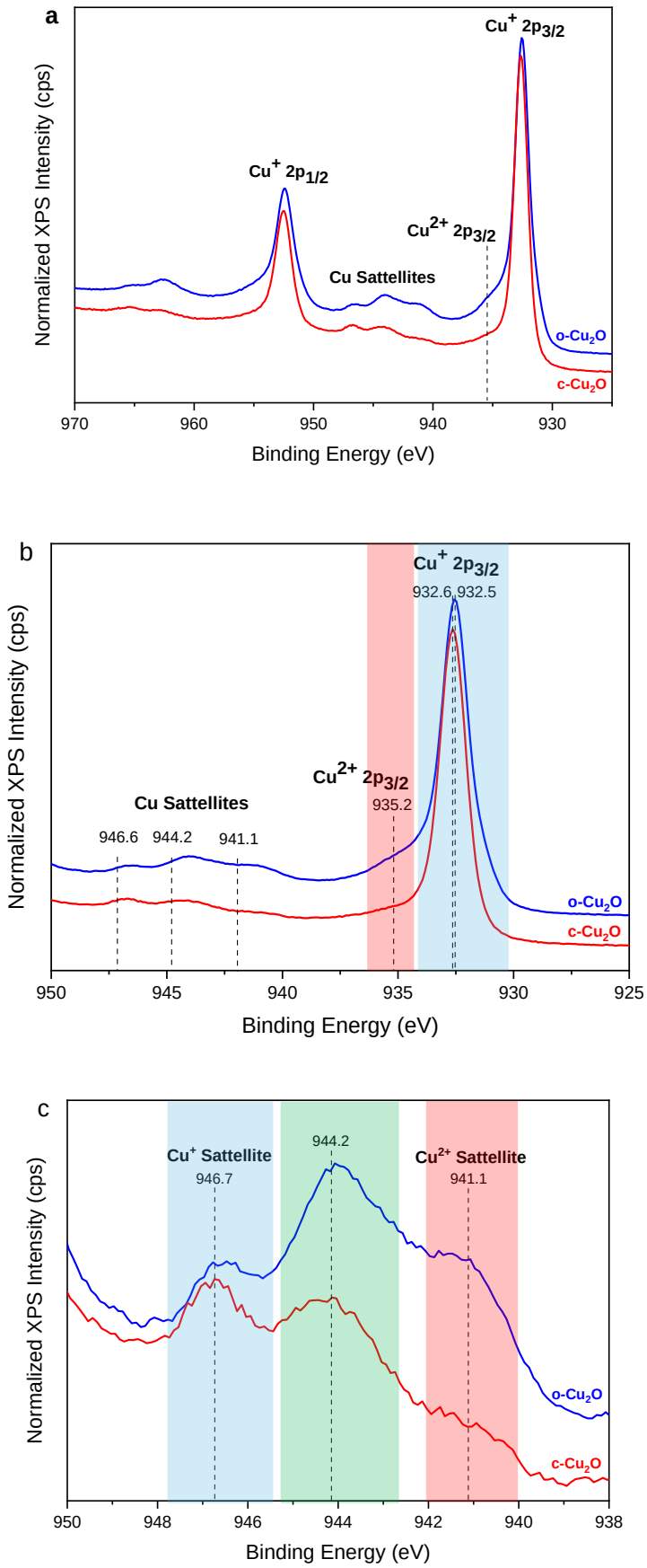


**Figure 19:** a-c) Cu 2p XPS spectra of c-$Cu_2O$ and o-$Cu_2O$.

### 3.6 Analysis of the nature of the surface adsorption sites by CO adsorption via in-situ FTIR:

In-situ CO adsorption experiments were performed via transmission FTIR spectroscopy to elucidate the nature of Cu adsorption sites on the surface. Figure 20 shows v(CO) region of the in-situ FTIR spectra of CO adsorption on c-$Cu_2O$ and o-$Cu_2O$ at 50˚C. For c-$Cu_2O$, a single sharp peak was observed at 2139 $cm^{-1}$ (highlighted in blue). On the other hand, for o-$Cu_2O$, besides a sharp and intense peak at 2143 $cm^{-1}$ (highlighted in blue) additional IR peaks at 2216, 2199, 2191 (highlighted in red), and 1978 $cm^{-1}$ (highlighted in green) were also observed.

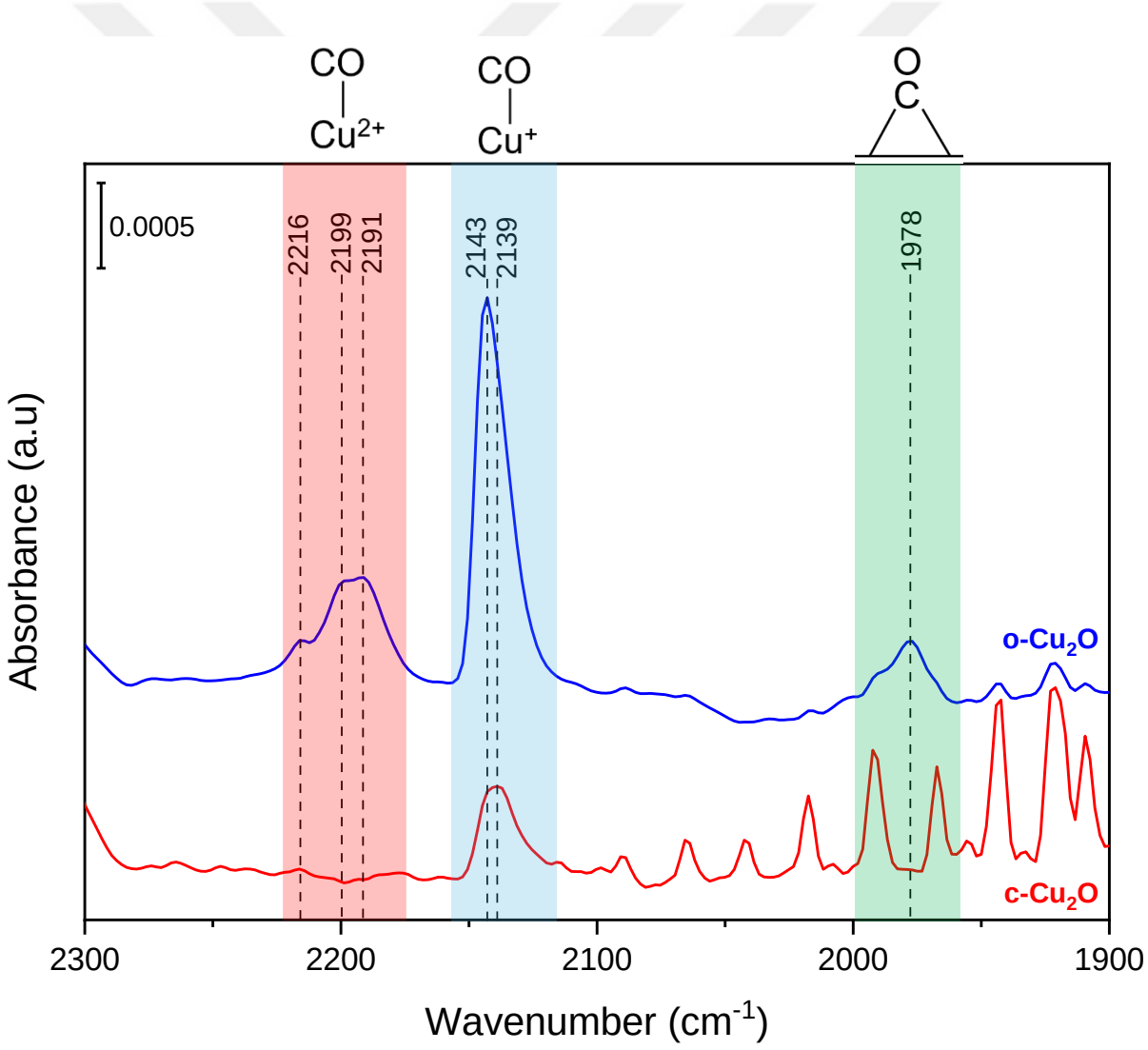


**Figure 20:** In-situ FTIR spectra of CO adsorption on c-$Cu_2O$, o-$Cu_2O$.

The peaks at 2139 $cm^{-1}$ for c-$Cu_2O$ and 2143 $cm^{-1}$ for o-$Cu_2O$ (highlighted in blue) are attributed to linearly adsorbed (atop) CO chemisorbed at $Cu^+$ sites [79-84]. It is apparent that the IR intensity of this linearly adsorbed CO species on $Cu^+$ sites is significantly stronger on o-$Cu_2O$ compared to that of c-$Cu_2O$. This is due to the presence of dissimilar surface structures and variations in the surface coordination on these two different surfaces as depicted in Figure 10. As can be seen in Figure 10, both surfaces are O-terminated (2-fold coordinated O, $O_{2c}$ for c-$Cu_2O$ and 3-fold coordinated O, $O_{3c}$ for o-$Cu_2O$) and the second layer consists 2-fold coordinatively saturated Cu ($Cu_{CSA}$) site only for c-$Cu_2O$, while there is both $Cu_{CSA}$ and 1-fold coordinatively unsaturated ($Cu_{CUS}$) sites present for o-$Cu_2O$. It is likely that the presence of unsaturated Cu ($Cu_{CUS}$) sites together with a more open surface create a stronger adsorption capability for CO on o-$Cu_2O$, explaining the higher intensity of the CO adsorption peak on o-$Cu_2O$ compared to that of c-$Cu_2O$ [53, 85]. Former reports in the literature reveal that CO can barely adsorb on c-$Cu_2O$ [86]. However, current in-situ FTIR spectroscopic data presented in Figure 20 show a clear peak which might be due to the presence of surface defects resulting from the smaller size of the $Cu_2O$ nanoparticles synthesized in the current work (~90 nm for c-$Cu_2O$ and ~430 nm for o-$Cu_2O$ ) as opposed to that of literature (400-700 nm for c-$Cu_2O$ and 300-600 nm for o-$Cu_2O$ [86]) or it is also likely that the surface cleaning procedures used in the former studies in the literature were not as effective as the currently devised procedures resulting in a weaker CO adsorption in the literature data. Another important feature of the IR bands located at 2139 $cm^{-1}$ for c-$Cu_2O$ and 2143 $cm^{-1}$ for o-$Cu_2O$ is the sharpness of these peaks. Sharp CO adsorption peaks in FTIR spectroscopy indicate uniform and homogenous $Cu^+$ adsorption sites on c-$Cu_2O$ and o-$Cu_2O$ consistent with their single-crystal-like nature revealing atomically well-defined adsorption sites verified by the current XRD (Figure 13) and XANES/EXAFS results (Figure 14 and Figure 15). The full-width half maxima (FWHM) of these IR peaks are measured to be as 16 and 14 $cm^{-1}$ for c-Cu2O and o-$Cu_2O$, respectively, as

illustrated in Figure 21a and b. When these values are compared with the FWHM values for IR signals of CO adsorbed on various single-atom catalysts (SAC) which show FWHM values between 15-22 $cm^{-1}$ [87, 88] and oxidized Cu(111) single crystal surfaces revealing FWHM values of ca. 10 $cm^{-1}$ [89]; it can be seen that the homogeneity and the uniformity of $Cu^{+}$ sites of c-$Cu_2O$ and o-$Cu_2O$ are comparable to that of SACs and oxidized Cu single crystal surfaces.

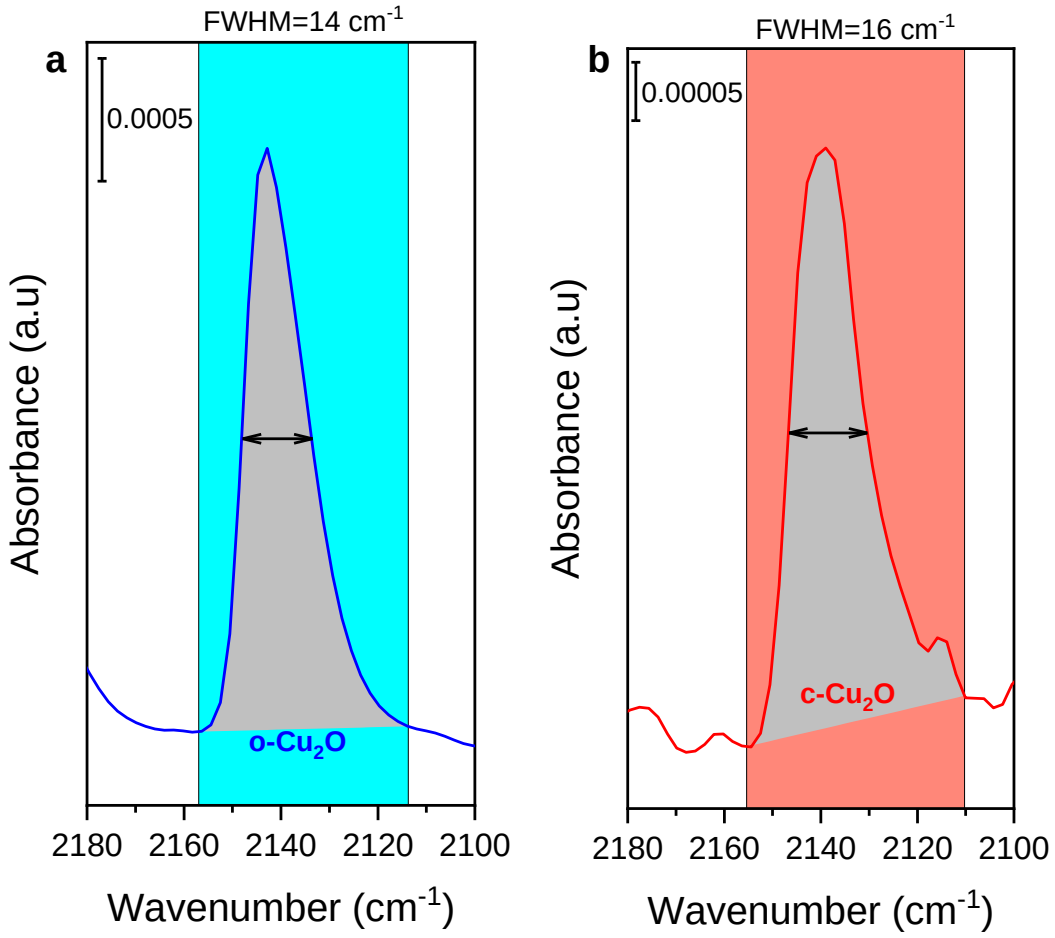


**Figure 21:** FWHM calculations of CO adsorbed on $Cu^{+}$ sites of a) c-$Cu_2O$ b) o-$Cu_2O$.

For o-$Cu_2O$; IR peaks between 2191-2216 $cm^{-1}$ (highlighted in red) in Figure 20 are attributed to the presence of CO adsorbed on $Cu^{2+}$ sites [79-84] and the broadness and convoluted nature of these peaks imply the heterogeneity of the $Cu^{2+}$ sites compared to $Cu^{+}$ sites. This assignment also aligns with the current XPS data given in Figure 19 showing the presence of a small amount of $Cu^{2+}$ on the surface. The IR peak at 1978 $cm^{-1}$ (highlighted in green) in Fig 20 for o-$Cu_2O$ is

attributed to bridge bound CO on either $Cu^0$ sites [79-84] or on surface defect sites such as steps, edge, or kink sites. Note that the conclusive verification of the presence of $Cu^0$ by XPS is challenging as the Cu $2p_{3/2}$ signals of $Cu^+$ and $Cu^0$ are nearly at the same binding energy. Overall, CO adsorption via in-situ FTIR spectroscopy showed that c-$Cu_2O$ and o-$Cu_2O$ have predominantly homogenous and uniform $Cu^+$ sites while non-uniform $Cu^{2+}$ and defect sites are also observed on o-$Cu_2O$ surfaces.

## 3.7 Analysis of the reducibility of $Cu_2O$ catalysts via $H_2$-TPR:

The reducibility of the c-$Cu_2O$ and o-$Cu_2O$ was investigated via $H_2$-TPR and shown in Figure 22. When the $H_2$-TPR profile of c-$Cu_2O$ is investigated a sharp and narrow peak was observed at 300 ˚C (highlighted in red) with a low-temperature shoulder at 263 ˚C (highlighted in blue). These two reduction signals can both be attributed to the reduction of $Cu^+$ surface species to $Cu^0$ on c-$Cu_2O$. This relatively low-temperature reduction process on c-$Cu_2O$ at 263 ˚C can associated to the facilitated activation of $H_2$ on the step-edges (i.e., extended defects bearing $Cu^+$ species with a lower coordination number than that of $Cu^+$ species on terraces) of c-$Cu_2O$; while the slightly higher-temperature (300 ˚C, highlighted in green) reduction process requiring a greater activation can be assigned to the reduction of $Cu^+$ surface species to $Cu^0$ on the terraces of c-$Cu_2O$.

On the other hand, the TPR profile of o-$Cu_2O$, reveals a quite different line shape than that of c-$Cu_2O$ (Figure 22) depicting a broad and a convoluted line-shape indicating a variety of reduction processes with dissimilar activation energies, with an additional very intense high-temperature reduction signal at 538 ˚C (highlighted in purple). This extremely high and very intense reduction signal at 538 ˚C can be attributed to the bulk reduction of $Cu^+$ species in the o-$Cu_2O$ lattice. Furthermore, reduction of $Cu^{2+}$ minority species (verified by the current Cu2p XPS results illustrated in Figure 19) to $Cu^+$ and subsequently to $Cu^0$ as well as the presence of

dissimilar $Cu^{+}$ surface species (i.e., $Cu_{CSA}$, and $Cu_{CUS}$ , Figure 10) can also contribute to the broad and convoluted nature of the TPR profile of o-$Cu_2O$.

The difference in the peak widths and peak positions of the TPR profiles given in Figure 22 for c-$Cu_2O$ and o-$Cu_2O$ can be explained in light of the average particle size and particle size distribution effects. When the SEM images given in Figure 11 and Figure 12 are analyzed, it can be readily realized that o-$Cu_2O$ nanocrystals are much larger in their average edge length (428 nm) with a broader particle size distribution compared to that of c-$Cu_2O$ with a smaller average edge length (90 nm) and a narrower particle size distribution.

The literature suggests that larger particles tend to reduce at higher temperatures due to the slower interaction with the reducing gas and a broad particle size distribution lead to a wide TPR profile due to the reduction of particles of different sizes at different temperatures [90]. It is expected that, low-coordination $Cu^{+}$ species located on edges and corners (i.e. extended defects and point defects) that are present on small c-$Cu_2O$ particles facilitates $H_2$ activation and shifts the reduction temperatures to lower temperatures.

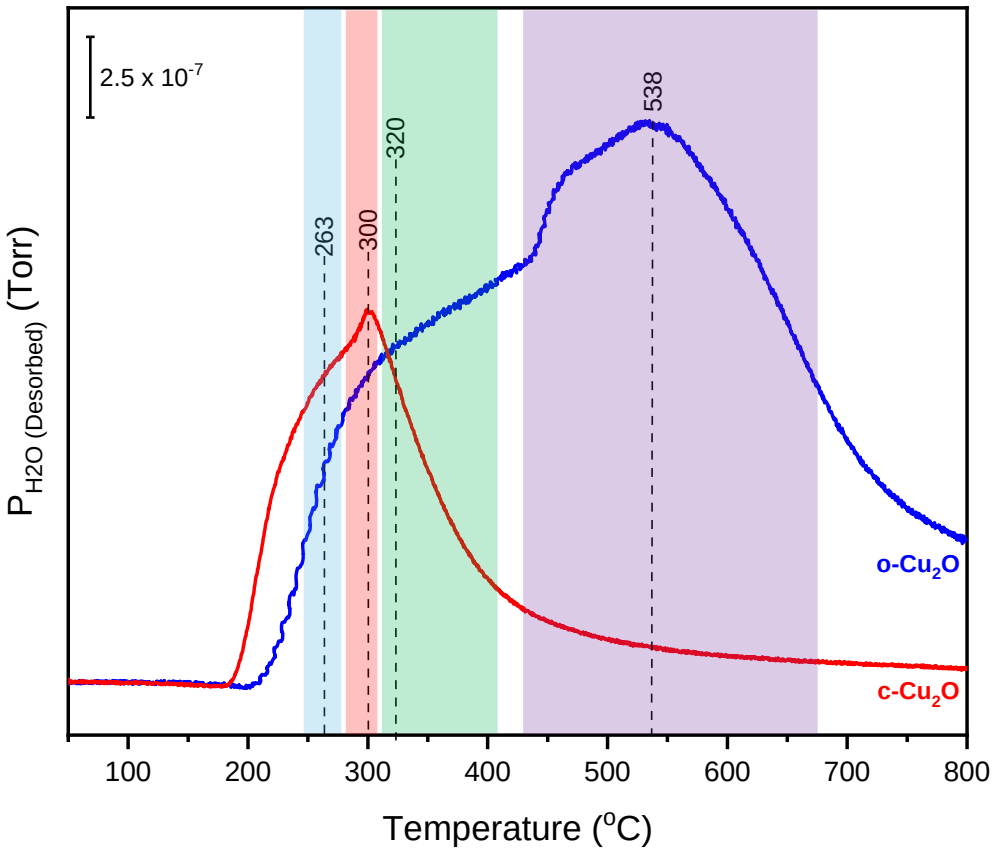


**Figure 22:** $H_2$-TPR profiles of c-$Cu_2O$ and o-$Cu_2O$.

When the low temperature (i.e., T < 350 ˚C) section of the TPR profiles of c-$Cu_2O$ and o-$Cu_2O$ given in Figure 22 are compared, it can be argued that the first reduction signal of c-$Cu_2O$ appears at 263 ˚C which is lower than that of o-$Cu_2O$ (320 ˚C). The lower initial peak temperature for the reduction of $Cu^+$ species on c-$Cu_2O$ suggests that $Cu^+$ sites on c-$Cu_2O$ are more readily reducible than that of o-$Cu_2O$. Thus, it can be argued that the surface oxide ions of c-$Cu_2O$ are more labile and these surface oxygen species can be readily utilized in the oxidation of methanol at low temperatures (T ≤ 250 ˚C) leading to a greater low-temperature methanol oxidation capability for c-$Cu_2O$ than that of o-$Cu_2O$ [75]. As will be shown in the later sections of this thesis, this important finding is in line with the fact that methanol thermal decomposition on c-$Cu_2O$ yields large amounts of $CO_2$ and $H_2O$ at T ≤ 250 ˚C; an observation that is consistent with the enhancement of the total oxidation pathway on c-$Cu_2O$ due to the readily available lattice oxygen species on the c-$Cu_2O$ surface that can be utilized for the total

oxidation of methanol. In contrast, $H_2$-TPR signals on o-$Cu_2O$ at T ≤ 250 ˚C (i.e., at temperatures relevant to methanol decomposition on $Cu_2O$ studied in the current work) appear at greater temperatures as compared to the c-$Cu_2O$ case, suggesting that o-$Cu_2O$ is less reducible at T ≤ 250 ˚C compared to c-$Cu_2O$. Hence, scarcity of available labile lattice oxygen species on o-$Cu_2O$ at T ≤ 250 ˚C is in very good agreement with the predominance of dehydrogenation pathways of methanol over total oxidation of methanol on o-$Cu_2O$ which will be further experimentally verified in the forthcoming section of this thesis.

## 3.8 Analysis of the methanol decomposition via in-situ FTIR:

Methanol decomposition was studied on c-$Cu_2O$ and o-$Cu_2O$ between 50-250˚C via in-situ FTIR. Figure 23 shows the in-situ FTIR spectra of methanol adsorption and decomposition on c-$Cu_2O$ and o-$Cu_2O$ surfaces.

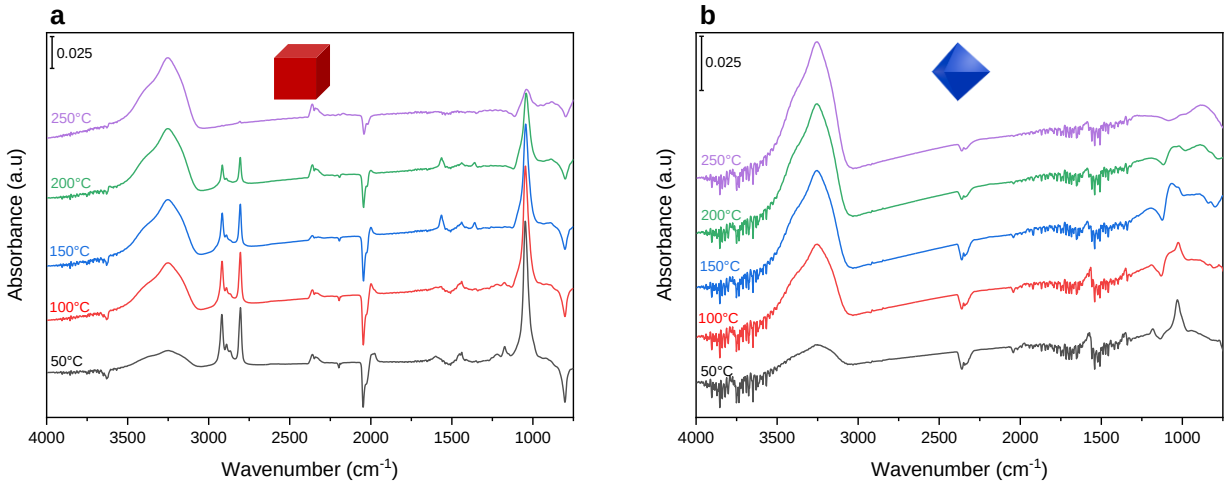


**Figure 23:** In-situ FTIR spectra of methanol adsorption on a) c-$Cu_2O$ b) o-$Cu_2O$.

When the 900-1100 $cm^{-1}$ region in Figure 24 is investigated for c-$Cu_2O$ and o-$Cu_2O$, three sharp peaks located at 1047 $cm^{-1}$ and 1030, 1065 $cm^{-1}$ are observed. These peaks are attributed to the v(C-O) modes of adsorbed methoxy ($CH_3O$-) species on different surface sites generated upon dissociative adsorption of methanol [18, 20, 22, 23-25, 34, 91-103]. The peaks at 1047

and 1030 $cm^{-1}$ belong to methoxy adsorbed on $Cu^{+}$ sites and the peak at 1065 $cm^{-1}$ might belong to methoxy adsorbed on $Cu^{2+}$ sites.

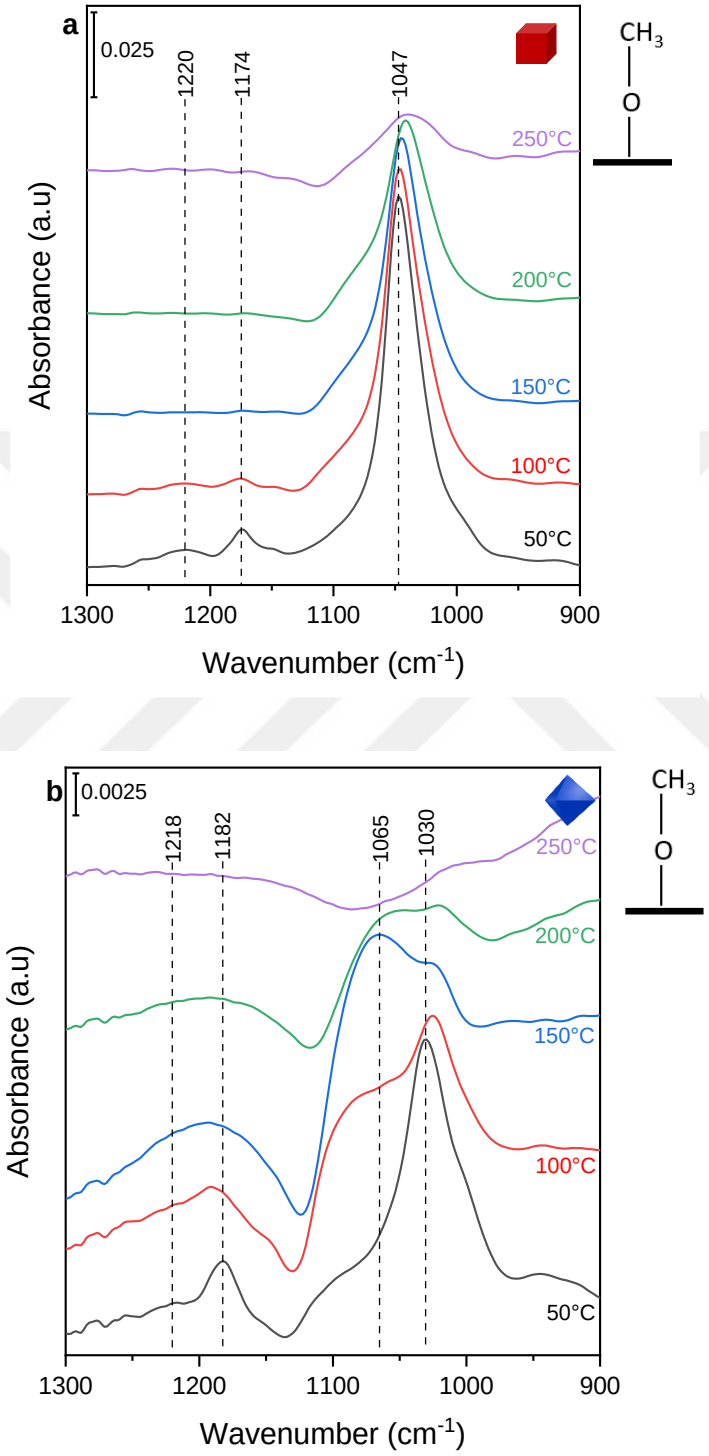


**Figure 24:** 900-1300 $cm^{-1}$ region of in-situ FTIR spectra of methanol adsorption on a) c-$Cu_2O$ b) o-$Cu_2O$.

In the 1150-1300 $cm^{-1}$ region shown in Figure 25a and b, peaks at 1174, 1220 $cm^{-1}$ were observed for c-$Cu_2O$ while IR signals at 1182, 1218 $cm^{-1}$ were visible for o-$Cu_2O$. These peaks are attributed to the $\omega(CH_2)$ and $\rho(CH_2)$ modes of dioxymethylene (-$OCH_2O$-) species, respectively [18, 20, 22, 23-25, 34, 91-103]. Dioxymethylene (DOM) is an intermediate species in the methanol decomposition pathway (Figure 6) and is formed via the reaction of formaldehyde with surface oxygen. Thus, the detection of DOM can be regarded as a strong indicator for the presence of formaldehyde.

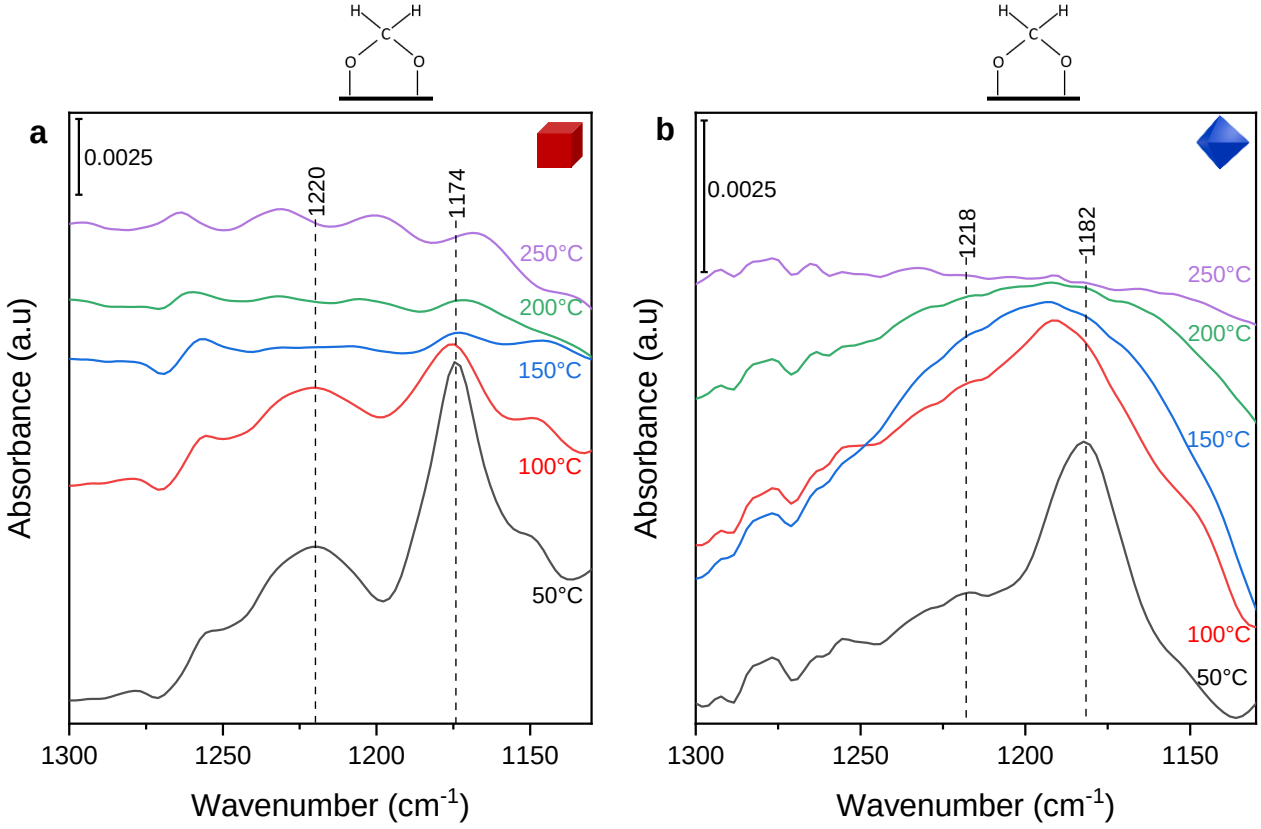


**Figure 25:**1150-1300 $cm^{-1}$ region of in-situ FTIR spectra of methanol adsorption on a) c-$Cu_2O$ b) o-$Cu_2O$.

Figure 26a and b shows the 1300-1800 $cm^{-1}$ region of the in-situ FTIR of methanol adsorption. For c-$Cu_2O$ (Figure 26a), peaks located at 1359, 1445, 1564 and 1599 $cm^{-1}$ are observed. The IR peak at 1445 $cm^{-1}$ for c-$Cu_2O$ belongs to the $\delta(CH_3)$ mode of methoxy species and similar to the v(C-O) mode, its intensity gradually decreased as the temperature increased, eventually

vanishing at 250 ˚C [18, 20, 22, 23-25, 34, 91-103]. The IR peaks of c-$Cu_2O$ at 1599 $cm^{-1}$ and 1564, 1359 $cm^{-1}$ belong the $v_{as}$(OCO) mode of monodentate formate and $v_{as}$(OCO), $v_s$(OCO) modes of bidentate formate species, respectively [18, 20, 22, 23-25, 34, 91-103].

For o-$Cu_2O$ (Figure 26b), only $v_{as}$(OCO) and $v_s$(OCO) modes of bidentate formate species were observed at 1568 and 1350 $cm^{-1}$, respectively. Contrary to the c-$Cu_2O$ data given in Figure 26a; $\delta(CH_3)$ mode of methoxy was not resolved on o-$Cu_2O$ (Figure 26b), due to low IR signal to noise ratio (S/N) obtained in the latter case.

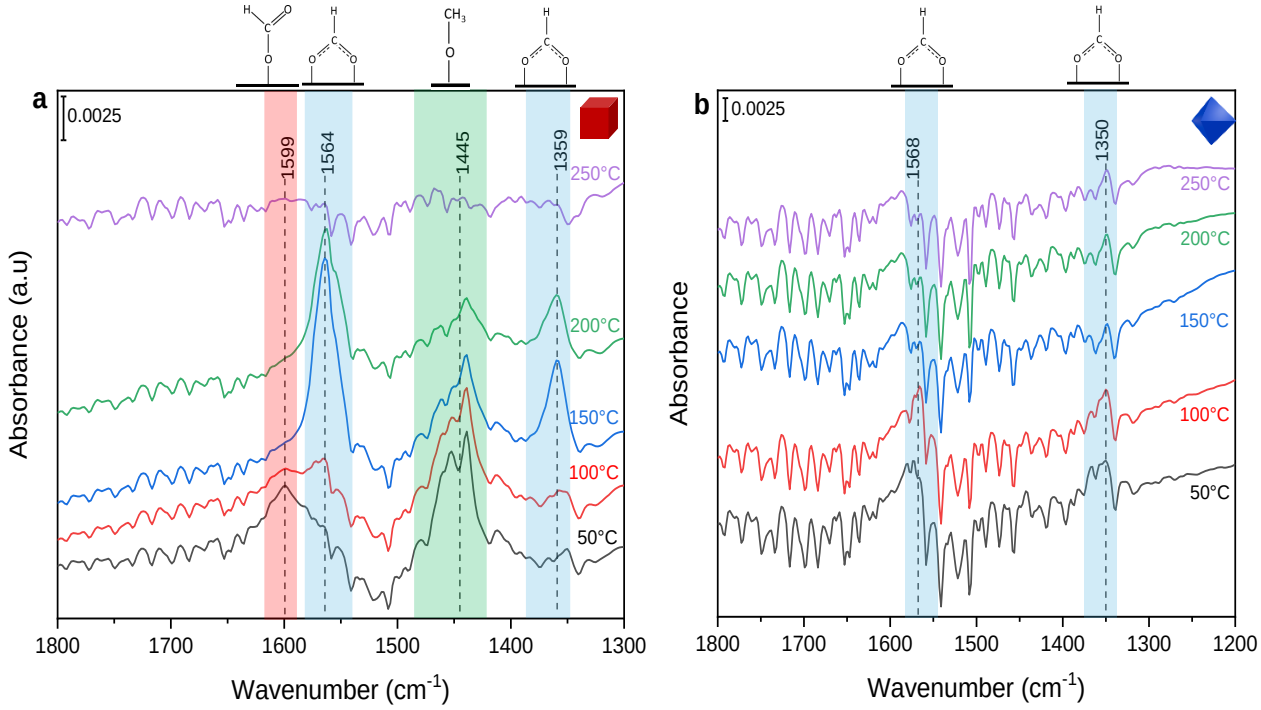


**Figure 26:**1300-1800 $cm^{-1}$ region of in-situ FTIR spectra of methanol adsorption on a) c-$Cu_2O$ b) o-$Cu_2O$.

When the v(CH) stretching region of the IR spectroscopic results are investigated (Figure 27a and b), no significant IR peaks can be detected for o-$Cu_2O$ (Figure 27b), and the observed residual peaks can be attributed to the insufficient subtraction of the background spectrum and the lower S/N of the IR data obtained for o-$Cu_2O$. The lower S/N of the FTIR data corresponding to o-$Cu_2O$ is probably due to the greater average particle size and the lower

overall surface area of the o-$Cu_2O$ as compared to that of c-$Cu_2O$. On the c-$Cu_2O$ surface (Figure 27a), v(CH) signals at 2804, 2866, 2889, 2919, and 2952 $cm^{-1}$ are observed. The peaks at 2804, 2866, 2889, and 2919 belong to the $\nu_s(CH_3)$, $2\delta(CH_3)$, $2\delta(CH_3)$, and $\nu_{as}(CH_3)$ of adsorbed methoxy, respectively ,and a similar trend with v(C-O) and $\delta(CH_3)$ is also observed for these species, where their intensities decreased as temperature increased, eventually vanishing at 250 ˚C. The peak at 2952 $cm^{-1}$ belongs to the $\nu(OCO) + \delta(CH)$ mode of bidentate formate and was observed at 100 and 150 ˚C.

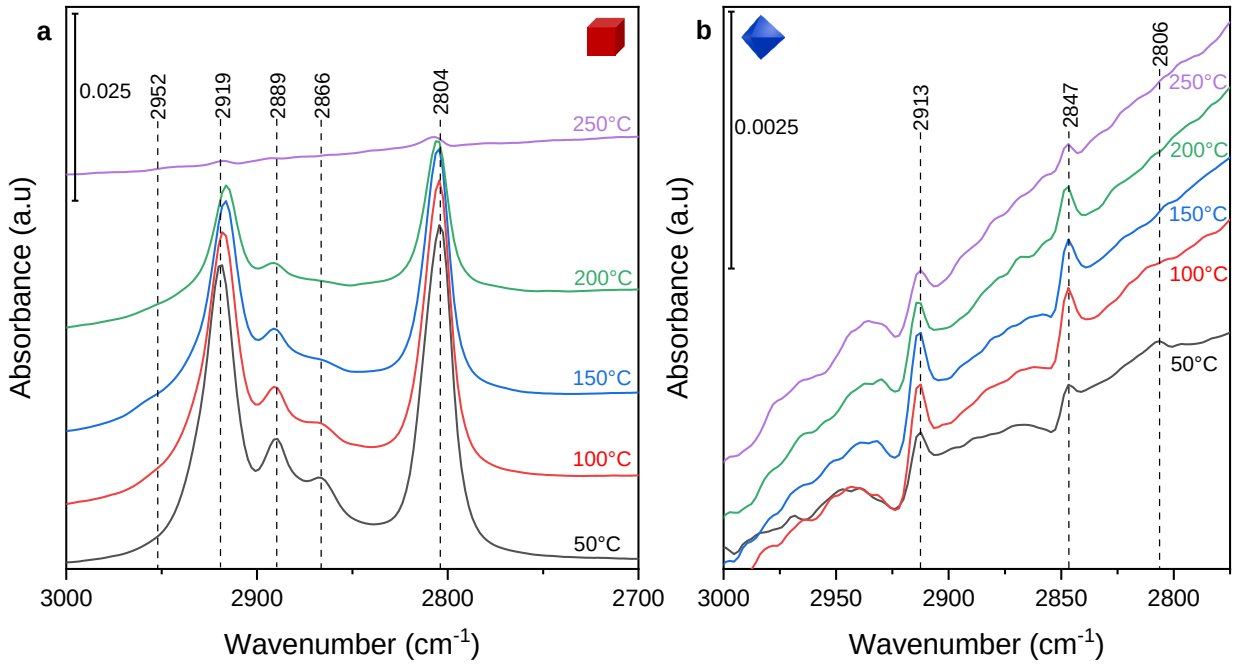


**Figure 27:** 2700-3000 $cm^{-1}$ region of in-situ FTIR spectra of methanol adsorption on a) c-$Cu_2O$ b) o-$Cu_2O$.

Figure 28a and b show the -OH stretching region of the in-situ FTIR of methanol adsorption. Broad peaks due to H-bonded OH groups are observed at 3252, 3369 $cm^{-1}$ for c-$Cu_2O$ and at 3256, 3374 $cm^{-1}$ for o-$Cu_2O$ and the intensities of these peaks increased with temperature probably due to the formation of hydroxyl functional groups generated upon dissociative adsorption of methanol leading to the methoxy groups as well as H atoms adsorbed on surface

oxygen sites resulting in hydrogen-bonded surface -OH groups. For c-$Cu_2O$, a small negative peak is observed at 3626 $cm^{-1}$, which indicates that some of the originally present isolated -OH functionalities on the surface interacted with adsorbates on the surface and transformed into H-bonded -OH groups.

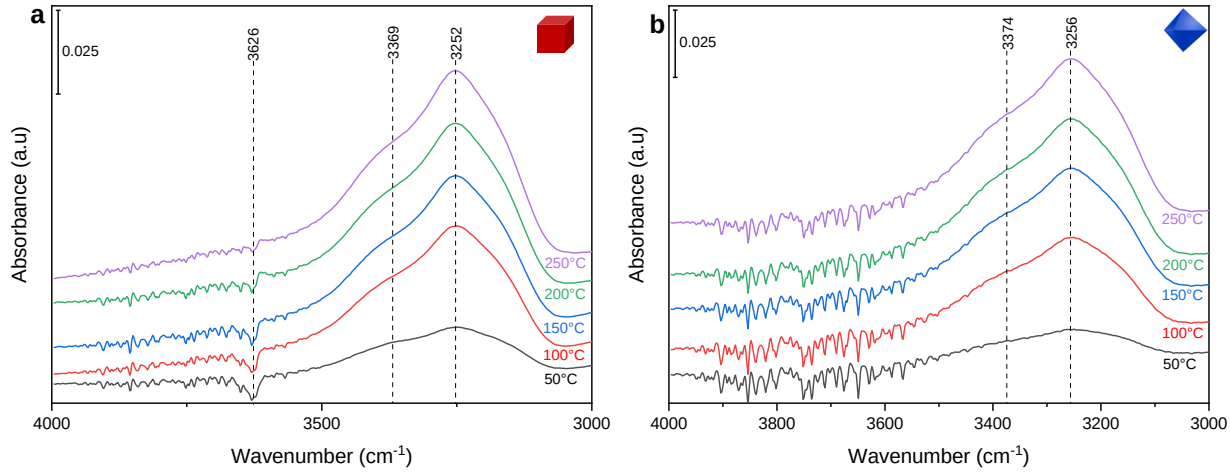


**Figure 28:** 3000-4000 $cm^{-1}$ region of in-situ FTIR spectra of methanol adsorption on a) c-$Cu_2O$ b) o-$Cu_2O$.

The assignments of the vibrational frequencies of the surface species observed during in-situ FTIR of methanol adsorption are summarized in Table 4.

| Species | IR modes | c-$Cu_2O$ | o-$Cu_2O$ | Refs. |
|---|---|---|---|---|
| 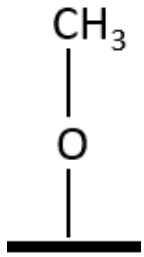 Methoxy | $\nu$(C-O) | 1047 on $Cu^+$ | 1030 on $Cu^+$<br>1065 on $Cu^{2+}$ | 18, 20, 22-25, 91-103 |
| | $\delta(CH_3)$ | 1445 | | |
| | $\nu_s(CH_3)$ | 2804 | | |
| | $2\delta(CH_3)$ | 2866<br>2889 | | |
| | $\nu_{as}(CH_3)$ | 2919 | | |
| 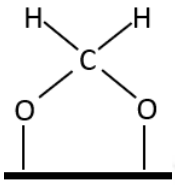 DOM | $\omega(CH_2)$ | 1174 | 1182 | |
| | $\rho(CH_2)$ | 1220 | 1280 | |
| 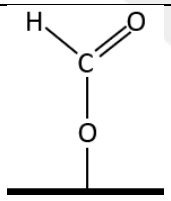 Monodentate Formate | $\nu_{as}$(OCO) | 1599 | | |
| 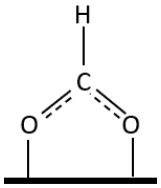 Bidentate Formate | $\nu_s$(OCO) | 1359 | 1350 | |
| | $\nu_{as}$(OCO) | 1564 | 1568 | |
| | $\nu$(OCO) + $\delta$(CH) | 2952 | | |
| Hydroxyls | $\nu$(OH) H-bonded | 3252<br>3369 | 3256<br>3374 | |
| | $\nu$(OH) Isolated | 3626 | | |

**Table 4:** Vibrational frequencies and the corresponding assignments for methoxy, DOM, monodentate formate, bidentate formate, and hydroxyls.

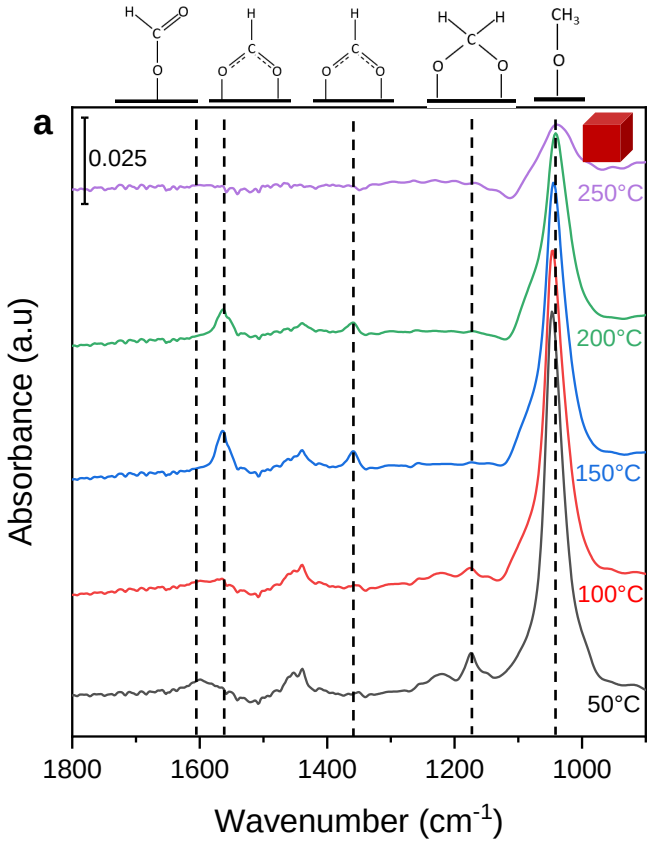


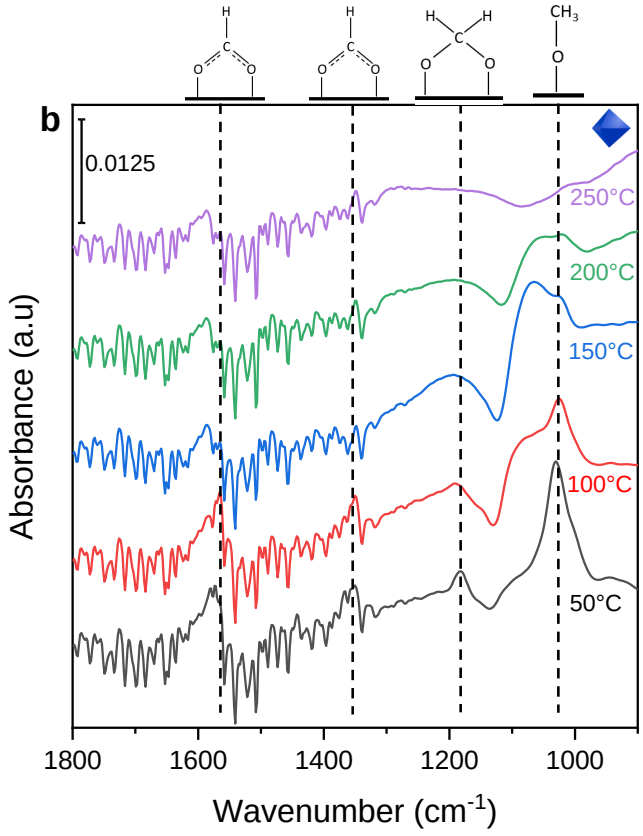


**Figure 29:** 900-1800 $cm^{-1}$ region of in-situ FTIR spectra of methanol adsorption on a) c-$Cu_2O$ b) o-$Cu_2O$.

Figure 29a and b show the 900-1800 $cm^{-1}$ region of in-situ FTIR spectra of methanol adsorption for c-$Cu_2O$ and o-$Cu_2O$, respectively. For c-$Cu_2O$, the intensity of the v(C-O) mode of methoxy species decreases gradually as temperature increases while there is still a slight amount of unreacted methoxy left at 250˚C (Figure 29a). On the other hand, for o-$Cu_2O$ the intensity of the peak at 1030 $cm^{-1}$ decreases much faster and the peak at 1065 $cm^{-1}$ emerged a maximum at 150˚C and at 250˚C there was no remaining methoxy on the surface (Figure 29b). The slower decay of the v(C-O) mode of methoxy at 1047 $cm^{-1}$ for c-$Cu_2O$ (Figure 30a) compared to the faster decay of the v(C-O) mode of methoxy at 1030 $cm^{-1}$ for o-$Cu_2O$ (Figure 30b), indicates a higher methoxy stability on c-$Cu_2O$ as opposed to o-$Cu_2O$.

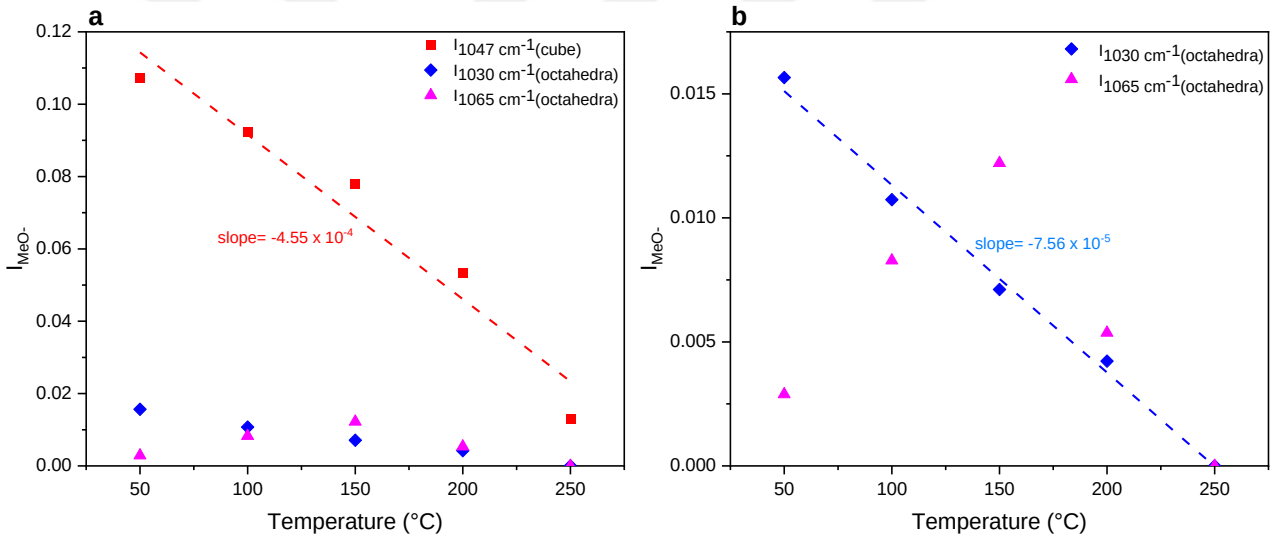


**Figure 30:** a) Intensity versus temperature plots for IR peaks located at 1030, 1047, and 1065 $cm^{-1}$ detected upon methanol adsorption b) zoomed in version.

When the intensities of the primary DOM IR peaks (i.e., 1174 $cm^{-1}$ for c-$Cu_2O$ and 1182 $cm^{-1}$ for o-$Cu_2O$), are normalized with respect to the methoxy IR peaks (i.e., 1047 $cm^{-1}$ for c-$Cu_2O$ and 1030 $cm^{-1}$ for o-$Cu_2O$) at 50˚C (Figure 31), it was observed that the DOM/methoxy ratio ($I_{DOM}/I_{MeO}$) is higher for o-$Cu_2O$ which might indicate that there is a greater amount of methanol decomposition to formaldehyde on o-$Cu_2O$ at 50˚C which leads to the higher DOM amount.

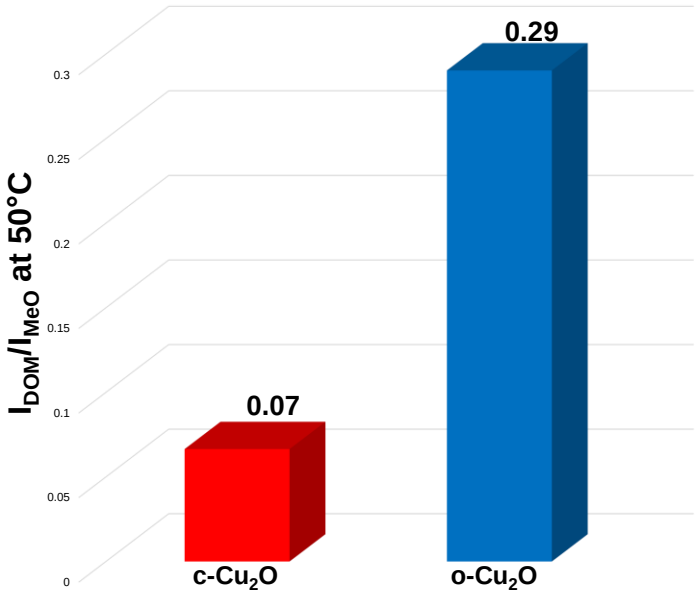


**Figure 31:** $I_{DOM}/I_{MeO}$ at 50°C for c-$Cu_2O$ and o-$Cu_2O$.

When the formation of the formate species are investigated (Figure 26a and Figure 29a) for c-$Cu_2O$, the formate intermediates are observed as monodentate formate species at 50 ˚C and are transformed to bidentate formate species at 150 ˚C. This observed transformation in the formate adsorption geometry and surface coordination can be explained by the availability of a greater number of adsorption sites on the surface at higher temperatures due to the thermal desorption resulting a lower surface coverage of adsorbates that can coordinate to multiple sites. For the c-$Cu_2O$ surface (Figure 26a and Figure 29a), a maximum in the intensity of the bidentate formate species was observed at 150 ˚C and these species vanished at 250˚C.

On the other hand, for o-$Cu_2O$ (Figure 26b and Figure 29b), formate species emerged as bidentate formate and were present until 100˚C on o-$Cu_2O$ (Figure 26b and Figure 29b), where such species managed to survive up to 200˚C on c-$Cu_2O$ (Figure 26a and Figure 29a). Moreover, the overall IR intensities of formate species were much greater on c-$Cu_2O$ compared to o-$Cu_2O$ showing a greater formate production and stability on the c-$Cu_2O$ surface.

Overall, dissociative adsorption of methanol led to methoxy formation on both surfaces (Figure 29). The stability of the methoxy species were higher on c-$Cu_2O$ compared to o-$Cu_2O$, as seen

from the decay rates of the v(CO) modes of methoxy (Figure 30). o-$Cu_2O$ was observed have higher selectivity in methanol decomposition to formaldehyde, compared to c-$Cu_2O$ shown by the higher normalized intensity of the DOM IR peaks (i.e., 1174 $cm^{-1}$ for c-$Cu_2O$ and 1182 $cm^{-1}$ for o-$Cu_2O$), shown in Figure 31. However, compared to o-$Cu_2O$, c-$Cu_2O$ was much more active in further oxidizing DOM to formate species as seen by elevated overall IR intensities of formate species on c-$Cu_2O$ (Figure 26a and Figure 29a). Enhanced generation of formate species on c-$Cu_2O$ surface is also consistent with the predominance of methanol total oxidation to $CO_2$ and $H_2O$ on c-$Cu_2O$ since it is known that at elevated temperatures formates generated upon methanol oxidation typically yield $CO_2$ and $H_2O$ [104]. Thus, in light of the aforementioned discussion given above, it can be argued that due to the readily reducible nature of the c-$Cu_2O$ surface, labile surface oxygens of c-$Cu_2O$ can be utilized by the adsorbed methoxy species, resulting in the oxidation of adsorbed methoxy species to surface formates, which further oxidize to form total oxidation products (i.e., $CO_2$ and $H_2O$) at higher temperatures (Figures 33 and 34). In contrast, on the o-$Cu_2O$ surface, since it is more difficult to exploit the surface oxygens of o-$Cu_2O$ due to the limited reducibility of this surface, methoxy species can only be partially oxidized to formaldehyde and DOM yielding $H_2O$, formaldehyde, CO and $H_2$ as the major decomposition products (Figure 33 and 34).

## 3.9 Analysis of the methanol decomposition via TPD:

Methanol TPD was performed to monitor the gaseous desorption products during methanol decomposition on c-$Cu_2O$ and o-$Cu_2O$. Figure 32 shows the blank TPD of the catalysts which were obtained by simply utilizing pristine c-$Cu_2O$ and o-$Cu_2O$ surfaces without and additional adsorbents. For T > 300 ˚C, it was observed that the blank TPD data were dominated by the decomposition of residual carbonaceous functionalities on the c-$Cu_2O$ and o-$Cu_2O$ surfaces originating from the chemicals used in the catalyst synthesis. On the other hand, below 350 ˚C, TPD desorption signals for the c-$Cu_2O$ and o-$Cu_2O$ surfaces were mostly negligible. Thus, in

order to differentiate TPD signals originating from pristine and methanol adsorbed c-$Cu_2O$ and o-$Cu_2O$ surfaces, we will focus on the low-temperature section (T < 350 ˚C) of the TPD data which are dominated by methanol decomposition features.

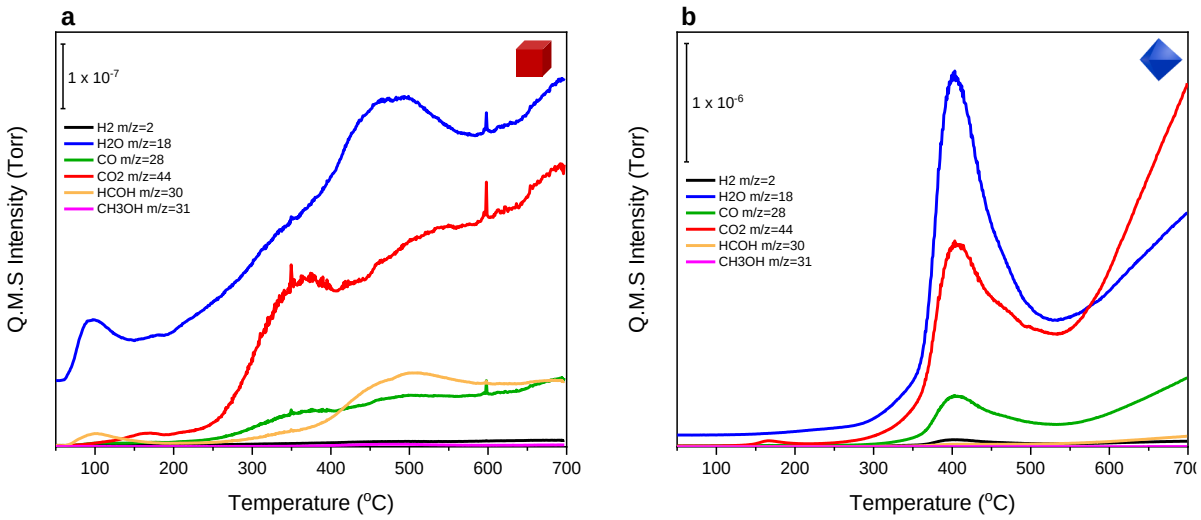


**Figure 32:** Blank TPD of pristine a) c-$Cu_2O$, b) o-$Cu_2O$.

Methanol TPD data of c-$Cu_2O$ and o-$Cu_2O$ are shown in Figure 33. For c-$Cu_2O$ (Figure 33a), two different desorption maxima were clearly visible at *ca.* 150 ˚C and ca. 280 ˚C for the following desorption products: $H_2$, $H_2O$, CO, $CO_2$, HCOH, and $CH_3OH$. The in-situ FTIR data of methanol adsorption on c-$Cu_2O$ showed that formate and methoxy species were stable up to 200 ˚C on c-$Cu_2O$ and fully desorbed at 250 ˚C except a small amount of methoxy, while there were also some additional species such as DOM which desorbed at 100˚C. Thus, observation of multiple major TPD desorption maxima for c-$Cu_2O$ (Figure 33a) as opposed to a single major desorption maximum for o-$Cu_2O$ (Figure 33b) can be attributed to the presence of a greater variety of surface functionalities on the former surface. In contrast, only a single major desorption peak was discernible for o-$Cu_2O$ at 220˚C (Figure 33b) for the following desorption products : $H_2$, $H_2O$, CO, $CO_2$, HCOH, and $CH_3OH$.

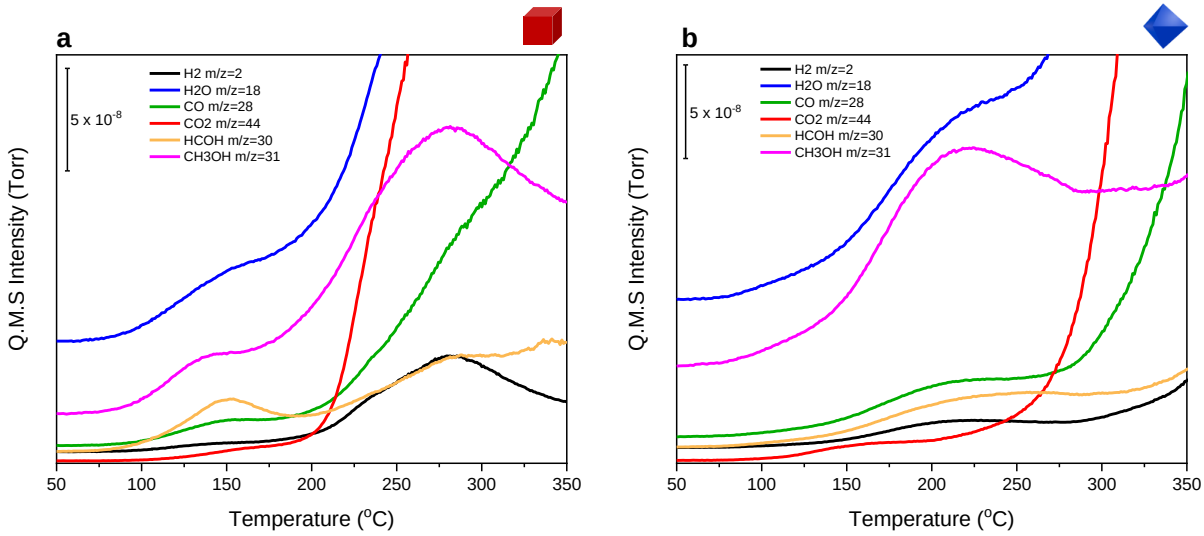


**Figure 33:** Methanol TPD data of a) c-$Cu_2O$ b) o-$Cu_2O$ for T < 350°C.

To quantify the relative amounts of the desorption products detected in the methanol TPD experiments, peak deconvolution was performed (Appendix E and Appendix F) and the relative TPD signal areas of the relevant peaks were calculated. During quantification calculations, mass spectroscopic fragmentation effects were carefully considered. Hence, the contributions of various m/z channels on other desorption channels due to QMS signal fragmentation were quantitatively estimated using reference QMS data shown in Appendix D. Figure 34 shows the total amounts of the products desorbed during the methanol TPD experiments on c-$Cu_2O$ and o-$Cu_2O$. It was observed that the total amount of products is 2.7 times greater for c-$Cu_2O$ compared to o-$Cu_2O$. This was expected since the smaller size of c-$Cu_2O$ results in a higher specific surface area, leading to the adsorption of a greater amount of methanol onto the c-$Cu_2O$ surface compared to that of o-$Cu_2O$ (note that the mass of the c-$Cu_2O$ and o-$Cu_2O$ samples used in the methanol TPD experiments were identical). Furthermore, 67 times greater $CO_2$ desorption was observed for c-$Cu_2O$ as compared to that of o-$Cu_2O$. This amount is significant considering that the total amount of all TPD desorption products differs by a factor of only 2.7 times between these two samples. The significant difference in the $CO_2$ production between c-

$Cu_2O$ and o-$Cu_2O$ is attributed to elevated formate production and consequent total oxidation to form $CO_2$ and $H_2O$ on c-$Cu_2O$ compared to o-$Cu_2O$ (Figure 26).

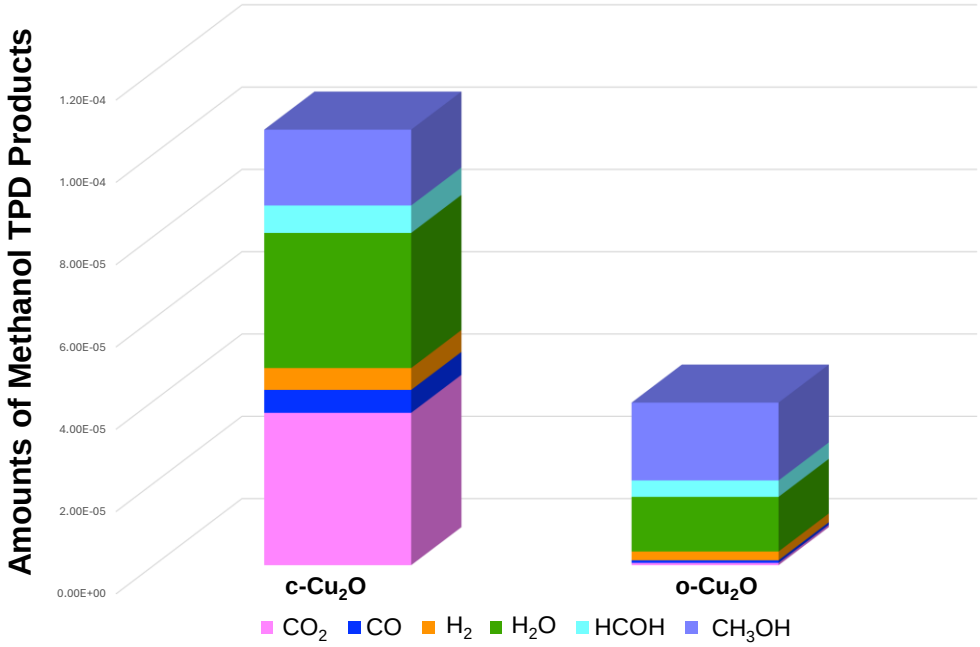


**Figure 34:** Quantification of methanol TPD products of c-$Cu_2O$ and o-$Cu_2O$.

## 3.10 Analysis of the formaldehyde decomposition via in-situ FTIR:

Formaldehyde is often involved in methanol reactions either as a product or an intermediate. Thus, the interaction of formaldehyde with c-$Cu_2O$ and o-$Cu_2O$ was investigated to obtain detailed information about the methanol transformation pathways from formaldehyde onwards, leading to other important intermediates such as DOM and formates. Figure 35 shows the in-situ FTIR spectra for formaldehyde adsorption on c-$Cu_2O$ and o-$Cu_2O$. The primary indication of formaldehyde molecular species on the surface is the presence of a sharp v(CO) peak around ~1700 $cm^{-1}$ and the absence of this peak on both surfaces indicates that formaldehyde molecular adsorption is not observed on c-$Cu_2O$ and o-$Cu_2O$ surfaces and formaldehyde is activated even at 50 ˚C on these surfaces [95-103, 105-112].

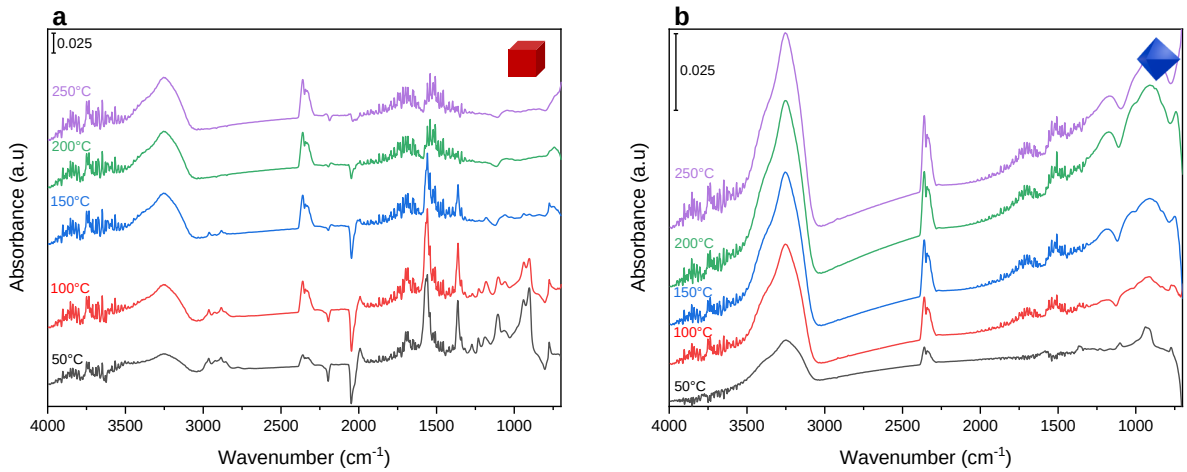


**Figure 35:** In-situ FTIR spectra of formaldehyde adsorption on a) c-$Cu_2O$ b) o-$Cu_2O$.

When the 800-1300 $cm^{-1}$ region in Figure 36a-c is investigated, intense peaks at 904, 941 $cm^{-1,}$ and 917, 938 $cm^{-1}$ are observed for c-$Cu_2O$ and o-$Cu_2O$, respectively; alongside weaker peaks between 1050-1300 $cm^{-1}$. The IR peak profile in Figure 35 within 800-1300 $cm^{-1}$ is similar to that of formaldehyde adsorption on $TiO_2$, $ZrO_2$, and $ThO_2$ reported in the literature where formaldehyde adsorption leads to the direct formation of dioxymethylene on the oxide surfaces [18, 22, 23, 95-103, 105-112]. As a result, the peaks in Figure 35 in the 800-1300 $cm^{-1}$ region are attributed to v(CO), ω($CH_2$), and $\rho$($CH_2$) modes of DOM. Similar to the results of the current methanol adsorption in-situ FTIR data given in Figure 25, DOM-related peaks disappeared after 100˚C for c-$Cu_2O$ and after 50˚C for o-$Cu_2O$. These findings suggest that DOM intermediate is the first step after formaldehyde generation during methanol decomposition and its reactivity on the surface possesses a significant role in the formation of formate species.

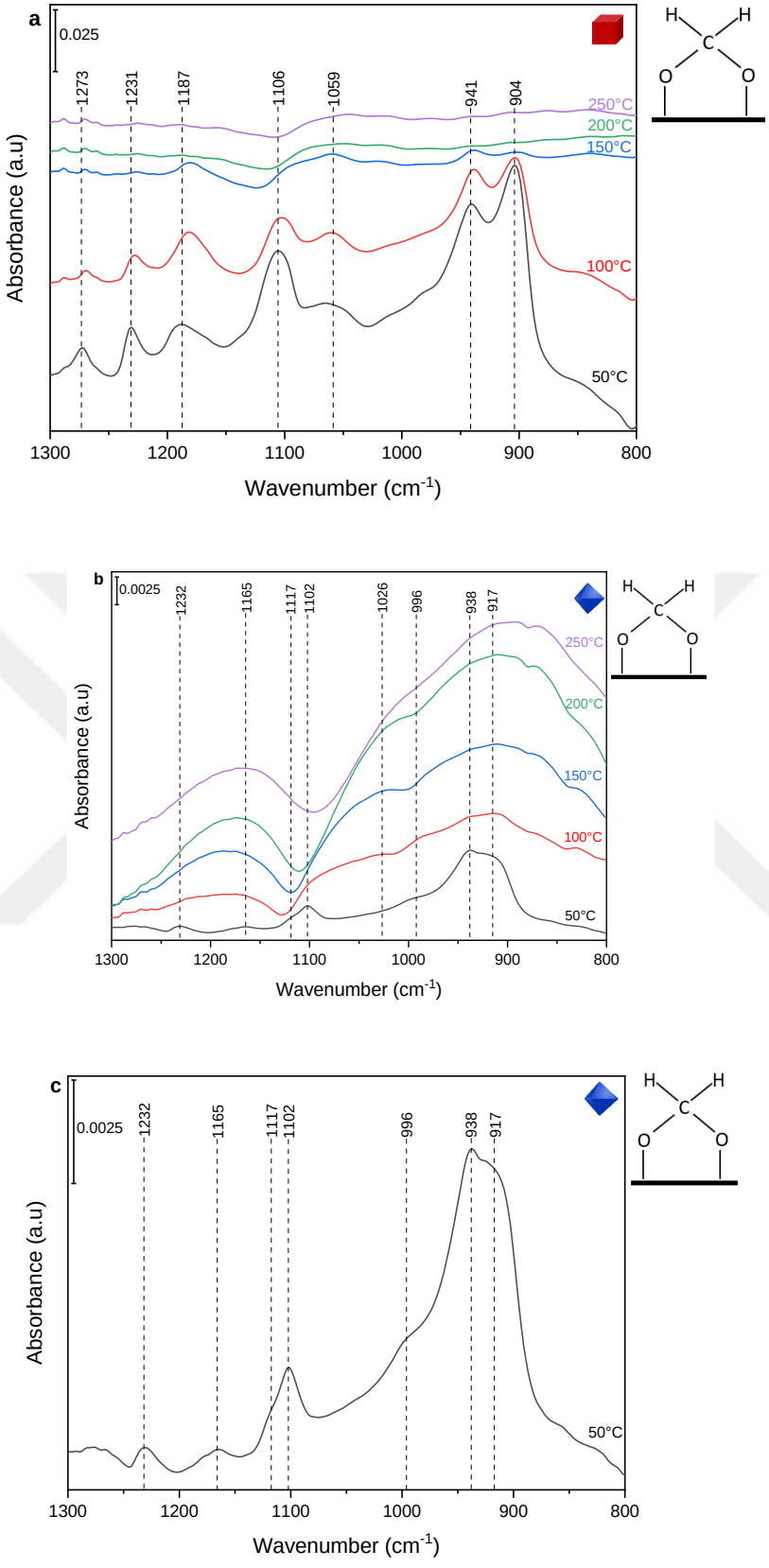


**Figure 36:** 800-1300 $cm^{-1}$ region of in-situ FTIR spectra of formaldehyde adsorption on a) c-$Cu_2O$ b-c) o-$Cu_2O$.

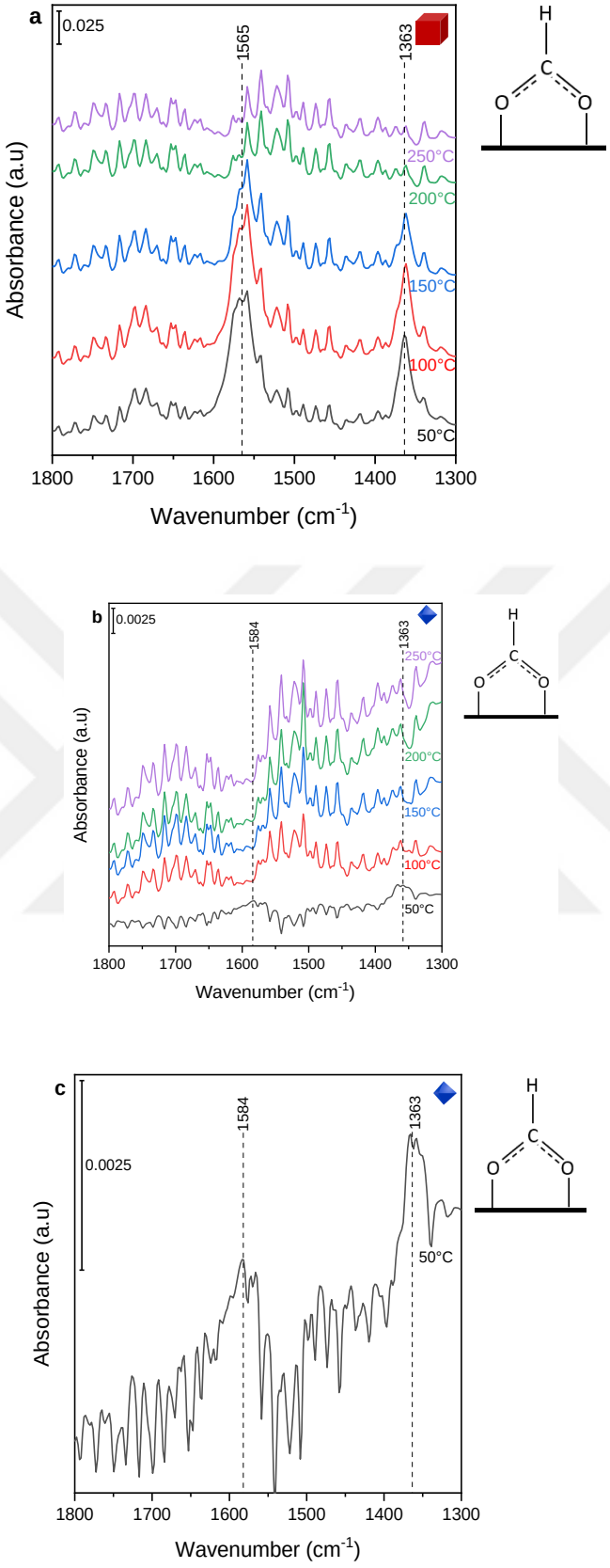


**Figure 37:** 1300-1800 $cm^{-1}$ region of in-situ FTIR spectra of formaldehyde adsorption on a) c-$Cu_2O$ b-c) o-$Cu_2O$.

When the 1300-1800 $cm^{-1}$ region in Figure 37a is investigated, very intense peaks at 1363 and 1565 $cm^{-1}$ are observed for c-$Cu_2O$. However, significantly weaker peaks are detectable for o-$Cu_2O$ at 1363 and 1584 $cm^{-1}$ (Figure 37b, c). These peaks are attributed to the $\nu_s$(OCO) and $\nu_{as}$(OCO) of bidentate formate species [18, 22, 23, 95-103, 105-112]. The formate species were observed on o-$Cu_2O$ only at 50 ˚C while these species were present on c-$Cu_2O$ until 150˚C showing higher stability.

The 2600-3000 $cm^{-1}$ region of the in-situ FTIR spectroscopic measurements acquired during formaldehyde adsorption is shown in Figure 38 for c-$Cu_2O$. Similarly to the methanol adsorption case, no peaks were observed in this region for o-$Cu_2O$. For c-$Cu_2O$, various IR peaks are observed at 2700, 2775, 2854, 2885, 2921, 2964, and 2983 $cm^{-1}$. The weak and broad bands at 2700 and 2775 $cm^{-1}$ can be related to the overtones of DOM species and the shoulder peak at 2983 $cm^{-1}$ is attributed to $\nu_{as}(CH_2)$ of DOM, as these peaks all disappear at the same temperature with DOM, i.e. at 100˚C [18, 22, 23, 95-103, 105-112]. The peaks at 2964, 2921, 2885, and 2854 are associated to formate species. The 2964 $cm^{-1}$ peak is attributed to $\nu$(OCO)+ $\delta$(CH) mode, and the 2885 $cm^{-1}$ peak is attributed to $\nu$(CH) modes while the other weaker peaks at 2854 and 2921 $cm^{-1}$ might be due to combination modes [18, 22, 23, 95-103, 105-112].

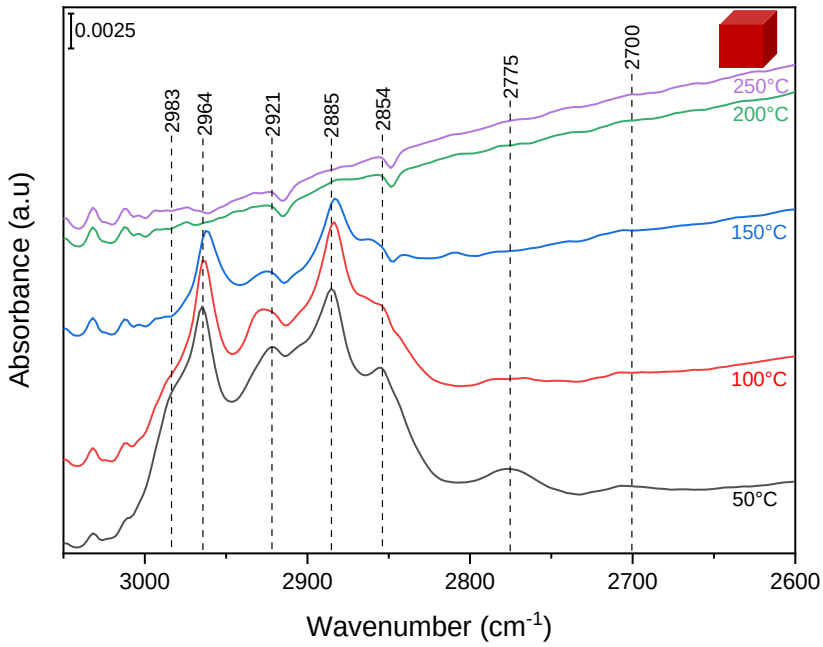


**Figure 38:** 2600-3000 $cm^{-1}$ region of in-situ FTIR spectra of formaldehyde adsorption on c-$Cu_2O$.

When, the 3000-4000 $cm^{-1}$ region is investigated, peaks at 3254, 3356 $cm^{-1}$ and 3252, 3357 $cm^{-1}$ are observed for c-$Cu_2O$ and o-$Cu_2O$ which can be attributed to H-bonded hydroxyls. The intensities of these peaks increased with temperature probably due to the formation of hydroxyls after dehydrogenation/dehydration reactions which was also observed during in-situ FTIR of methanol decomposition (Figure 39).

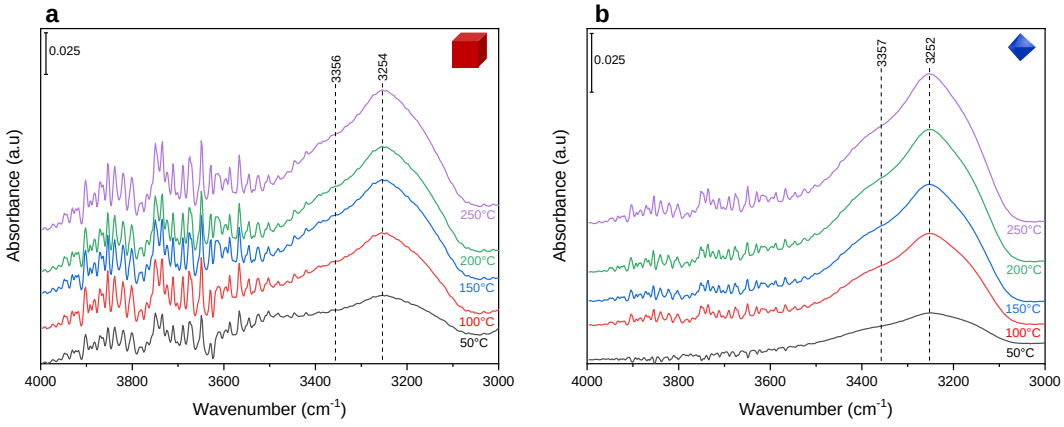


**Figure 39:** 3000-4000 $cm^{-1}$ region of in-situ FTIR spectra of formaldehyde adsorption on a) c-$Cu_2O$ b) o-$Cu_2O$.

The assignments of the vibrational frequencies of the surface species observed during in-situ FTIR of formaldehyde adsorption are summarized in Table *5*.

| Species | IR modes | c-$Cu_2O$ | o-$Cu_2O$ | Refs. |
|---|---|---|---|---|
| 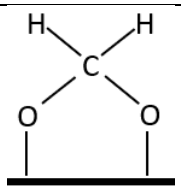 DOM | $\nu$(CO) | 904 | 917 | 18, 22, 23, 95-103, 105-112 |
| | $\omega(CH_2)$ | 941 | 938 | |
| | $\rho(CH_2)$ | 1059 | 966 | |
| | | 1106 | 1102 | |
| | | 1187 | 1117 | |
| | | 1231 | 1165 | |
| | | 1273 | 1232 | |
| | Overtones | 2700 | | |
| | | 2775 | | |
| | $\nu_{as}(CH_2)$ | 2983 | | |
| 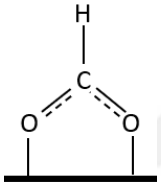 Bidentate Formate | $\nu_s$(OCO) | 1363 | 1363 | |
| | $\nu_{as}$(OCO) | 1565 | 1584 | |
| | | 2854 | | |
| | $\nu$(CH) | 2885 | | |
| | | 2921 | | |
| | $\nu$(OCO) + $\delta$(CH) | 2964 | | |
| Hydroxyls | $\nu$(OH) H-bonded | 3254 | 3252 | |
| | | 3356 | 3357 | |

**Table 5:** Vibrational frequencies and the corresponding assignments for DOM, bidentate formate, and hydroxyls observed from in-situ FTIR of formaldehyde adsorption.

Overall, the in-situ FTIR of formaldehyde adsorption showed that formaldehyde is not molecularly adsorbed but rather gets activated to form DOM species on both c-$Cu_2O$ and o-$Cu_2O$, as shown in Figure 40. The relative amounts of formates produced at 50˚C are compared to that of DOM generated at the same temperature by plotting the corresponding IR intensity values, i.e., $I_{Formate(50^\circ C)}/I_{DOM(50^\circ C)}$ (Figure 40). Firstly, by looking at the intensities of the $\nu_{as}$(OCO) peak at 1363 $cm^{-1}$ in Figure 37, it is apparent that there is much more formate generation on c-$Cu_2O$ compared to o-$Cu_2O$ at 50 ˚C. Secondly, comparison of the

$I_{Formate(50^{\circ}C)}/I_{DOM(50^{\circ}C)}$ ratios shows that the normalized intensity of $I_{Formate(50^{\circ}C)}/I_{DOM(50^{\circ}C)}$ is 4.1 times higher for c-$Cu_2O$ compared to o-$Cu_2O$ at 50 ˚C, as shown in Figure 40. These results are in very good agreement with the formate generation observed in the current in-situ FTIR spectroscopic methanol decomposition studies presented in Figure 26, and indicates that the c-$Cu_2O$ surface is much more successful in activating DOM for further oxidation to formates at 50 ˚C.

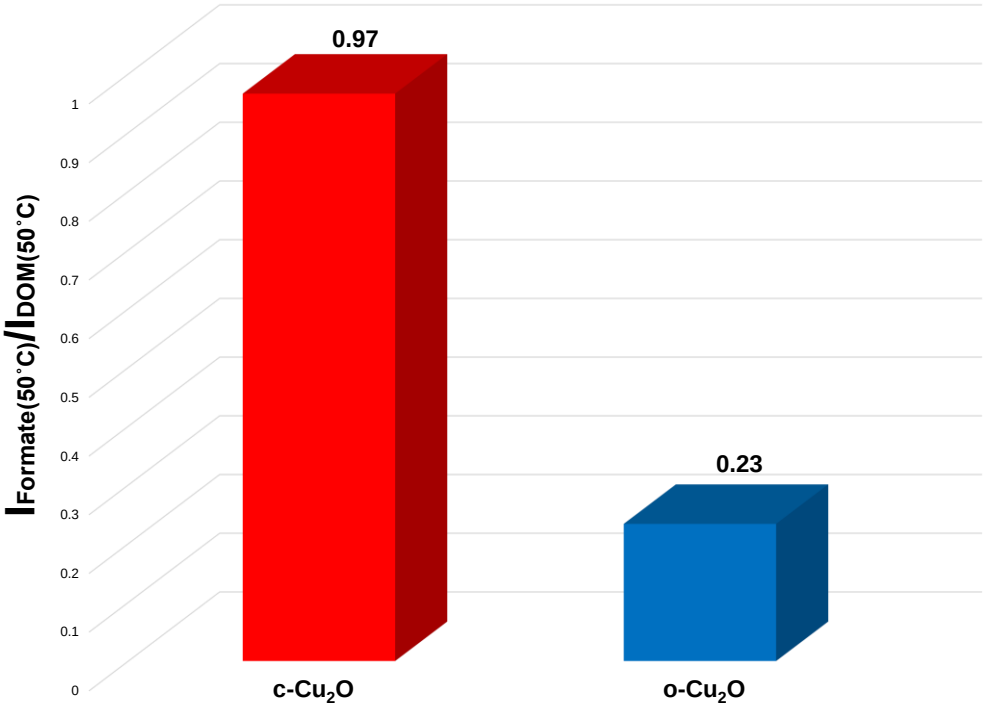


**Figure 40:** $I_{Formate}/I_{DOM}$ in-situ FTIR signal intensity ratios obtained during formaldehyde adsorption on c-$Cu_2O$ and o-$Cu_2O$ at 50 °C.

## 3.11 Analysis of the formaldehyde decomposition TPD:

Formaldehyde TPD was performed to monitor the gaseous desorption products during formaldehyde decomposition on c-$Cu_2O$ and o-$Cu_2O$ (Figure 41). For c-$Cu_2O$, a single desorption peak was observed at ~175 ˚C with a shoulder at $CO_2$ at 227 ˚C. For o-$Cu_2O$ a main desorption peak was observed at ~201˚C for $H_2$, CO, $CO_2$ and HCOH while the main peaks for

$H_2O$ and $CH_3OH$ was observed at 240 and 225˚C. Apart from the main peaks, shoulder peaks were observed at ~268˚C for $H_2$, CO, HCOH, and $CH_3OH$ o-$Cu_2O$.

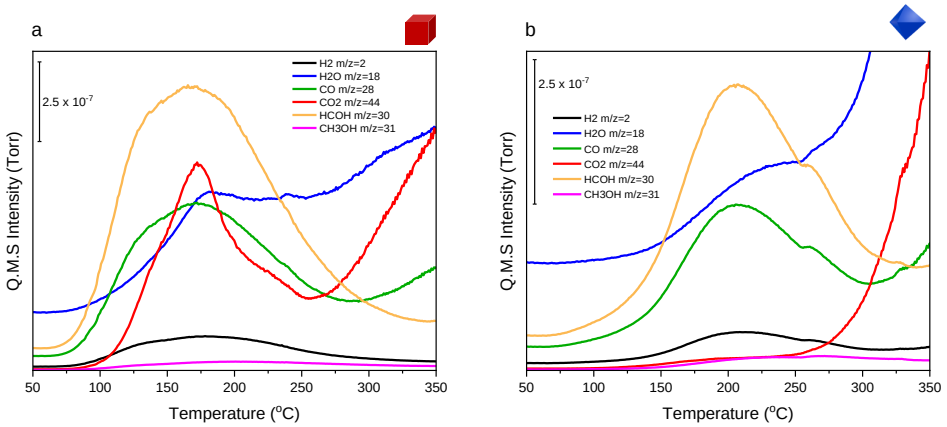


**Figure 41:** Formaldehyde TPD of a) c-$Cu_2O$ b) o-$Cu_2O$.

When the total amounts of products formed during formaldehyde TPD were quantified (Figure 42) by performing peak deconvolution (Appendix G and Appendix H), it was observed that total amount of products is 2.8 times greater for c-$Cu_2O$ compared to o-$Cu_2O$. Similar to the results from methanol TPD, the $CO_2$ production was 27 times higher for c-$Cu_2O$ in comparison to o-$Cu_2O$. These results align well with the findings from methanol TPD and indicate that c-$Cu_2O$ has a higher selectivity towards $CO_2$ production due to increased activity for oxidizing DOM to formates.

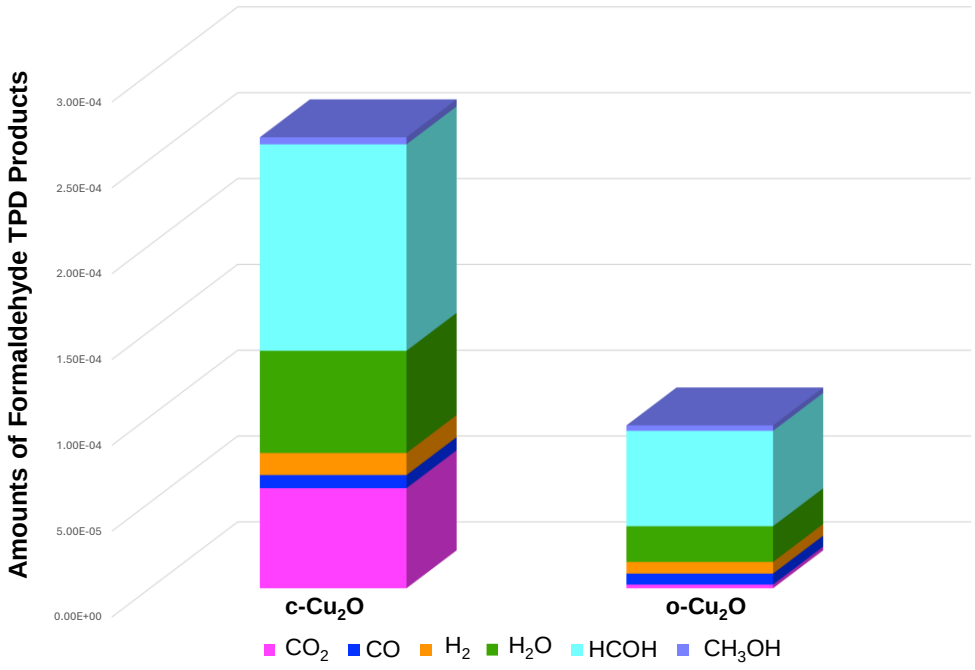


**Figure 42:** Quantification of formaldehyde TPD products of c-$Cu_2O$ and o-$Cu_2O$.

## 3.12 Structure-functionality relationships of c-$Cu_2O$ and o-$Cu_2O$ during methanol decomposition:

The in-situ FTIR of methanol showed dissociative adsorption behavior and the in-situ FTIR of formaldehyde showed that formaldehyde was not molecularly adsorbed but instead transformed into dioxymethylene species on both morphologies. The methoxy species adsorbed on the $Cu^+$ sites on c-$Cu_2O$ and stayed on the surface up to 250 ˚C. However, two adsorption sites, $Cu^+$ and $Cu^{2+}$, were observed on o-$Cu_2O$ similar to the results of CO adsorption. The primary adsorption site on o-$Cu_2O$ is $Cu^+$ while the secondary adsorption site might be either $Cu^{2+}$ or the defect sites. Furthermore, the methoxy species were less stable on the o-$Cu_2O$ surfaces as seen from the faster decay of the ν(CO) peak of methoxy seen in Figure 30. When the methoxy to DOM conversion was compared, a 4.4 times greater methoxy to DOM conversion was observed for o-$Cu_2O$ compared to c-$Cu_2O$, (Figure 31). Despite a higher methoxy conversion to DOM, the stability of the DOM species was lower on the o-$Cu_2O$ surface. The DOM-related peaks were only present at 50˚C for o-$Cu_2O$ but they stayed on the c-$Cu_2O$ surface up to 100˚C and

disappeared after that. The stability of DOM species on the surfaces followed a similar trend during methanol and formaldehyde adsorption. Additionally, the extent of DOM activation varied between the two catalysts. A much higher DOM activation was observed on c-$Cu_2O$ compared to o-$Cu_2O$. The $I_{Formate}/I_{DOM}$ ratio was 4.1 times higher for c-$Cu_2O$ (Figure 40), leading to a greater amount of formate generation. The higher amount of formate production on c-$Cu_2O$ resulted in 67 and 27 times more $CO_2$ production during methanol and formaldehyde TPD, respectively compared to o-$Cu_2O$ (Figure 43). This difference suggests that there is a significant difference in the $CO_2$ yield between c-$Cu_2O$ and o-$Cu_2O$.

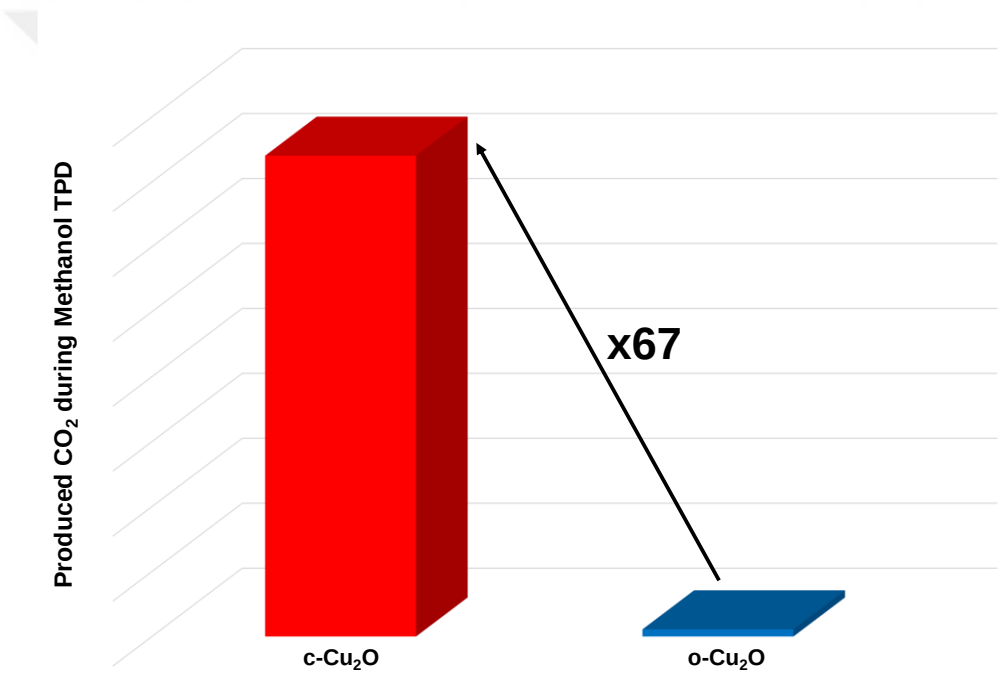


**Figure 43:** Difference in $CO_2$ production during methanol TPD of c-$Cu_2O$ and o-$Cu_2O$.

A significant difference in the $CO/CO_2$ production ratios was also observed for c-$Cu_2O$ and o-$Cu_2O$. For methanol TPD on and o-$Cu_2O$, the $CO/CO_2$ ratio was 7.7 times greater than that of c-$Cu_2O$. Likewise, for formaldehyde TPD, this ratio was 22.9 times greater for o-$Cu_2O$ as opposed to c-$Cu_2O$ . This indicates that the selectivity is shifted towards CO for the o-$Cu_2O$ catalyst as shown in Figure 44 and Figure 45.

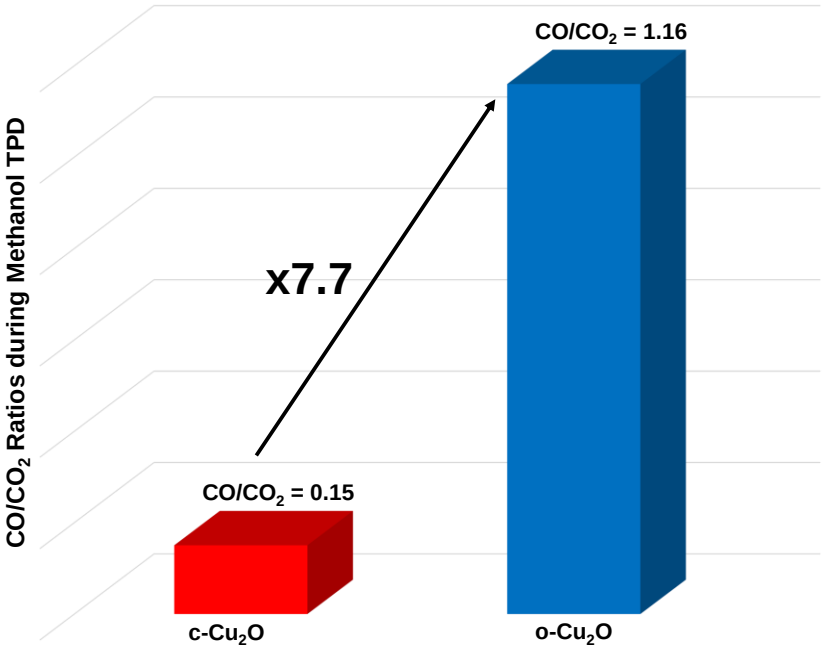


**Figure 44:** $CO/CO_2$ ratio of c-$Cu_2O$ and o-$Cu_2O$ during methanol TPD.

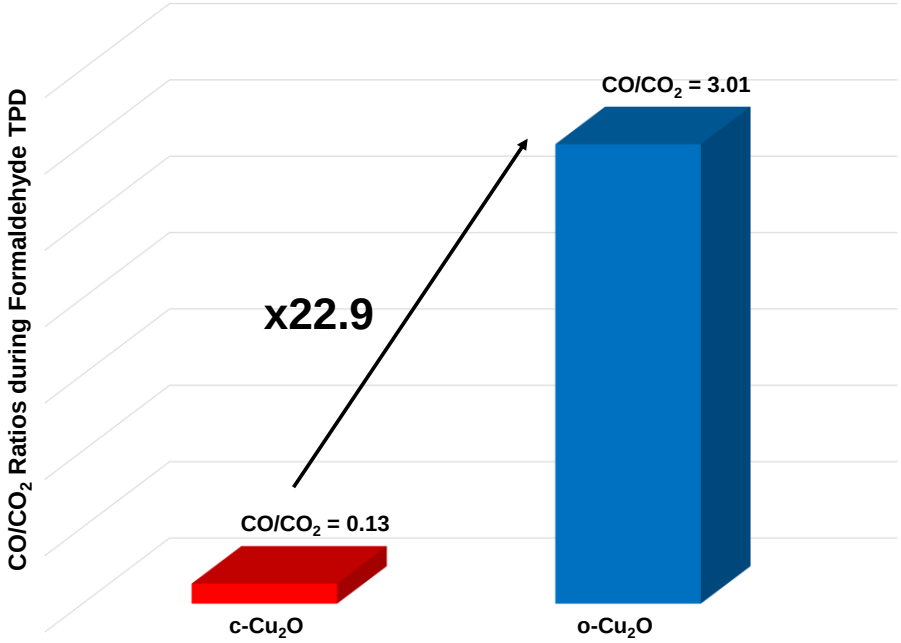


**Figure 45:** $CO/CO_2$ ratio of c-$Cu_2O$ and o-$Cu_2O$ during formaldehyde TPD.

Additionally, when the $CO_2/H_2O$ ratios are compared for c-$Cu_2O$ and o-$Cu_2O$ (Figure 46) it is observed that $CO_2/H_2O$ ratio is much higher for c-$Cu_2O$ compared to o-$Cu_2O$. When we look at the $CO_2$ production (Figure *43*), $CO/CO_2$ ratios (Figure *44* and Figure *45*), and $CO_2/H_2O$ ratios

(Figure 46) it is clear that total oxidation is the dominant pathway on c-$Cu_2O$ while partial oxidation/dehydrogenation is the dominant pathway on o-$Cu_2O$

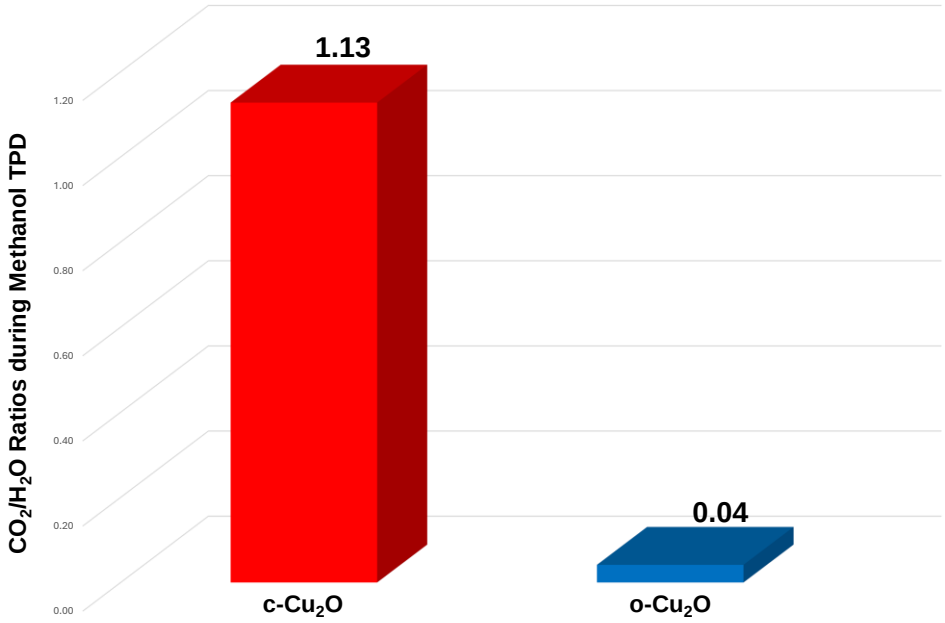


**Figure 46:** $CO_2/H_2O$ ratio of c-$Cu_2O$ and o-$Cu_2O$ during methanol TPD.

Moreover, the ratios of $H_2$, $H_2O$, CO, and $CO_2$ were also investigated. These are the products or the reactants of the common reactions involving methanol such as methanol synthesis, methanol decomposition, partial oxidation of methanol, and steam reforming of methanol. The ratios of reactants, for methanol synthesis, and the ratios of products, for methanol decomposition, partial oxidation of methanol, and steam reforming of methanol, are listed in Table 6.

| Reaction Name | Ratios of reactants |
|---|---|
| Methanol Synthesis | $H_2/CO = 2$<br>$H_2/CO_2 = 3$ |
| | **Ratios of products** |
| Methanol Decomposition | $H_2/CO = 2$ |
| Partial Oxidation of Methanol | $H_2/CO_2 = 2$ |
| Steam Reforming of Methanol | $H_2/CO_2 = 3$ |

**Table 6:** Ratios of reactants and products for methanol reactions.

Figure *47* shows the ratios of generated $H_2/CO$, $H_2O/CO$, $H_2/CO_2$, and $H_2O/CO_2$ during methanol TPD for c-$Cu_2O$ and o-$Cu_2O$. When we look at these ratios, it is observed that the $H_2/CO_2$ ratio is 3.87 for o-$Cu_2O$ while it is 0.14 for c-$Cu_2O$. The closeness of the $H_2/CO_2$ ratio for o-$Cu_2O$ to that of steam reforming of methanol suggests that octahedral $Cu_2O$ exposing (111) is much more suitable for this reaction compared to c-$Cu_2O$ showing the structure-functionality relationship of shape-defined $Cu_2O$ catalysts.

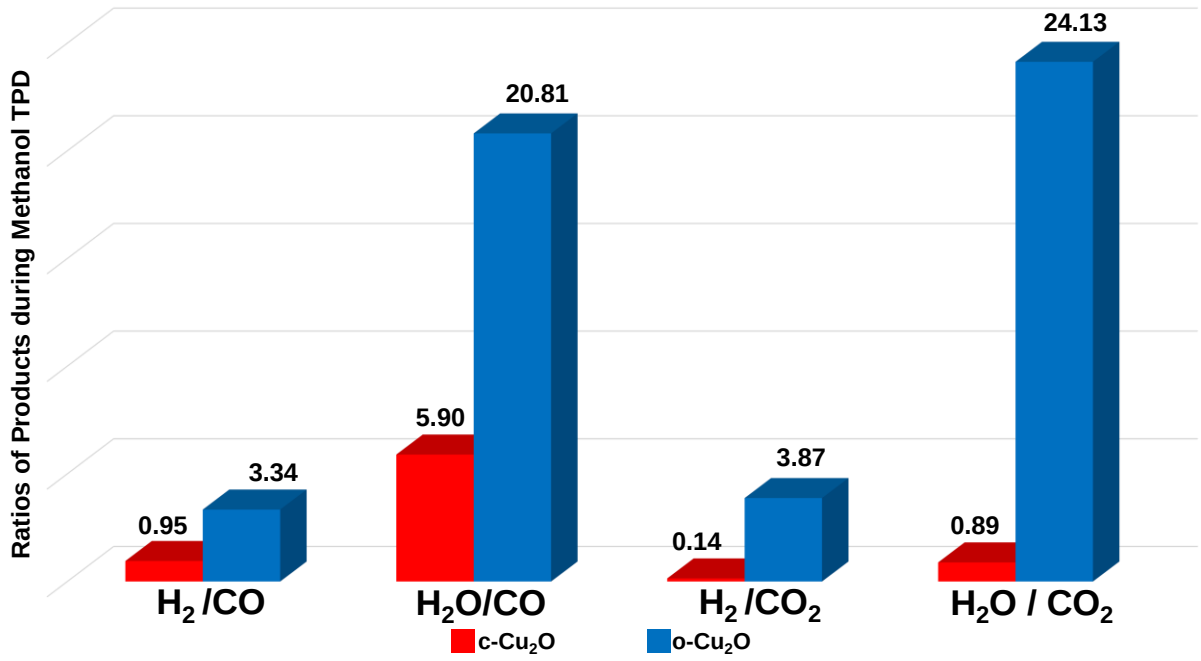


**Figure 47:** $H_2/CO$, $H_2O/CO$, $H_2/CO_2$, and $H_2O/CO_2$ ratios for during methanol TPD for c-$Cu_2O$ and o-$Cu_2O$.

Another important ratio in Figure *47* that stands out is the $H_2/CO$ ratio of c-$Cu_2O$ which is 0.95. $CO + H_2$, commonly known as syngas is the cornerstone of the chemical industry and different $H_2/CO$ ratios are required for different industrial processes. One of these industrial processes is the Fischer-Tropsch synthesis in which the $H_2/CO$ ratio close to unity is desired for the production of hydrocarbon fuels and valuable chemicals [113-115]. In this context, the $H_2/CO$ ratio of 0.95 obtained from methanol decomposition over c-$Cu_2O$ might be relevant for utilizing syngas for Fischer-Tropsch synthesis.

# 4. Conclusions

In this study, the structure-functionality relationships of shape-defined $Cu_2O$ catalysts were investigated during methanol decomposition. This study also aims to serve as a bridge between studies on copper single crystal catalysts and complex polycrystalline copper catalysts which are widely studied in heterogenous catalytic transformations of methanol.

The structural characterization of the c-$Cu_2O$ and o-$Cu_2O$ via XRD, XANES, and EXAFS revealed that these model catalysts have highly ordered single crystal-like $Cu_2O$ structures in the bulk. ATR-IR and XPS results showed that there are residual ($-C_xH_yO_z$) surface functionalities present on the surfaces after synthesis followed by washing/etching. CO adsorption experiments via in-situ FTIR spectroscopy and XPS measurements showed that Cu sites on c-$Cu_2O$ surface are almost entirely in +1 oxidation state, while o-$Cu_2O$ surface reveals a more defective surface where Cu sites possess predominantly +1 oxidation state as well as the +2 minority oxidation state. The reducibility of the catalysts were investigated by $H_2$-TPR revealing that reduction of c-$Cu_2O$ can be initiated at a lower temperature than that of o-$Cu_2O$. On the other hand, o-$Cu_2O$ is more prone to bulk reduction at higher temperatures (T> 500 °C) as compared to c-$Cu_2O$.

Methanol and formaldehyde adsorption and decomposition were studied via in-situ FTIR and TPD on c-$Cu_2O$ and o-$Cu_2O$. These investigations showed that (Figure 47) a higher methoxy to DOM conversion was observed on o-$Cu_2O$, but o-$Cu_2O$ was not active in converting DOM to formates. On the other hand, c-$Cu_2O$ showed significant DOM activation which results in the enhanced formate generation on the c-$Cu_2O$ surface. These general trends observed in the in-situ FTIR spectroscopic experiments were also encountered in the corresponding TPD measurements, as c-$Cu_2O$ produced 67 times more $CO_2$ during methanol TPD than o-$Cu_2O$.

Thus in overall, it is proposed that labile surface oxygens that can be readily donated from the c-$Cu_2O$ surface can facilitate low-temperature ($T \leq 250$ °C) methanol/methoxy oxidation to formates which in turn yield predominantly $CO_2$ and $H_2O$ as the total oxidation products. In contrast, limited reducibility of the o-$Cu_2O$ surface only allows methanol/methoxy oxidation to first formaldehyde and then to DOM, eventually yielding predominantly CO and $H_2$ as the thermal decomposition products, indicating the predominance of dehydrogenation catalytic pathways rather than total oxidation. Furthermore, TPD measurements also showed that c-$Cu_2O$

catalysts produced syngas which has a $H_2/CO$ ratio close to unity which falls in the desired range for Fischer-Tropsch synthesis. On the other hand, methanol thermal decomposition on o-$Cu_2O$ results in a $H_2/CO_2$ ratio of 3.87 which is similar to that of the product distribution in steam reforming of methanol.

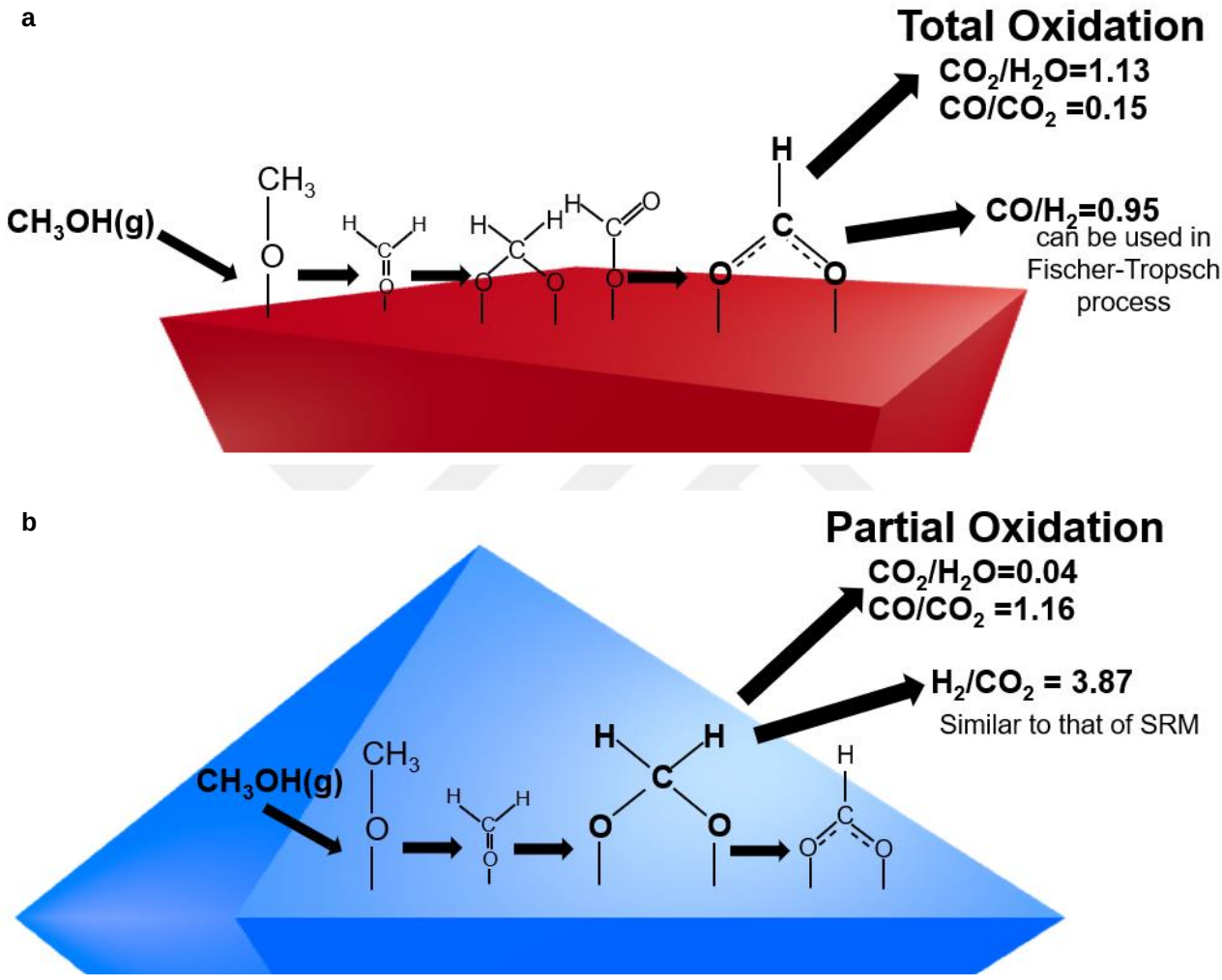


**Figure 48:**Demonstartion of structure-functionality relationships of a) c-$Cu_2O$ b) o-$Cu_2O$ for methanol decomposition.

# Appendix

## Appendix A: SEM images of o-$Cu_2O$ before and after etching

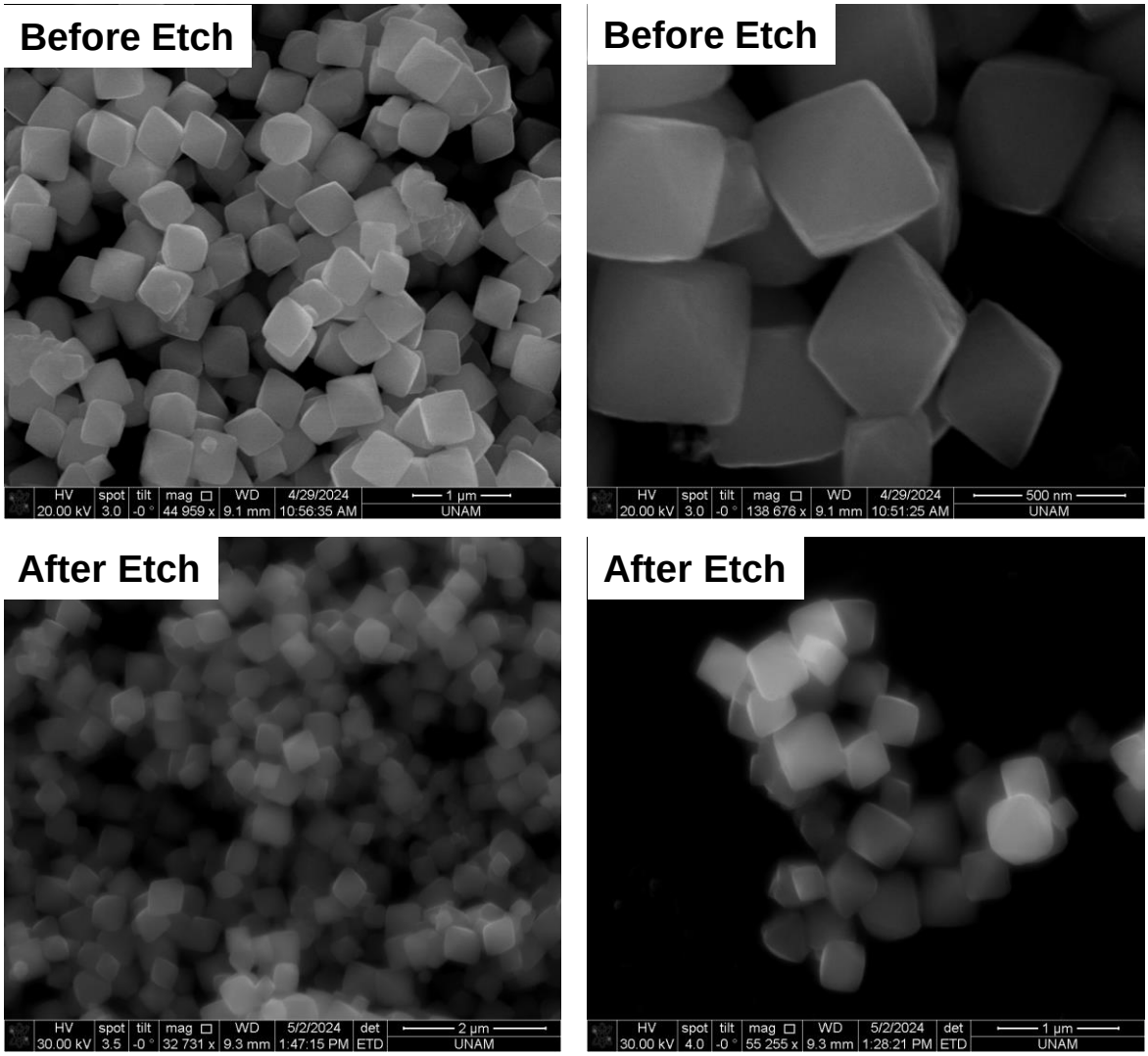


**Appendix A:** SEM images of o-$Cu_2O$ before and after etching.

## Appendix B: Surface atomic percentages from XPS survey spectra of o-$Cu_2O$ before and after etching

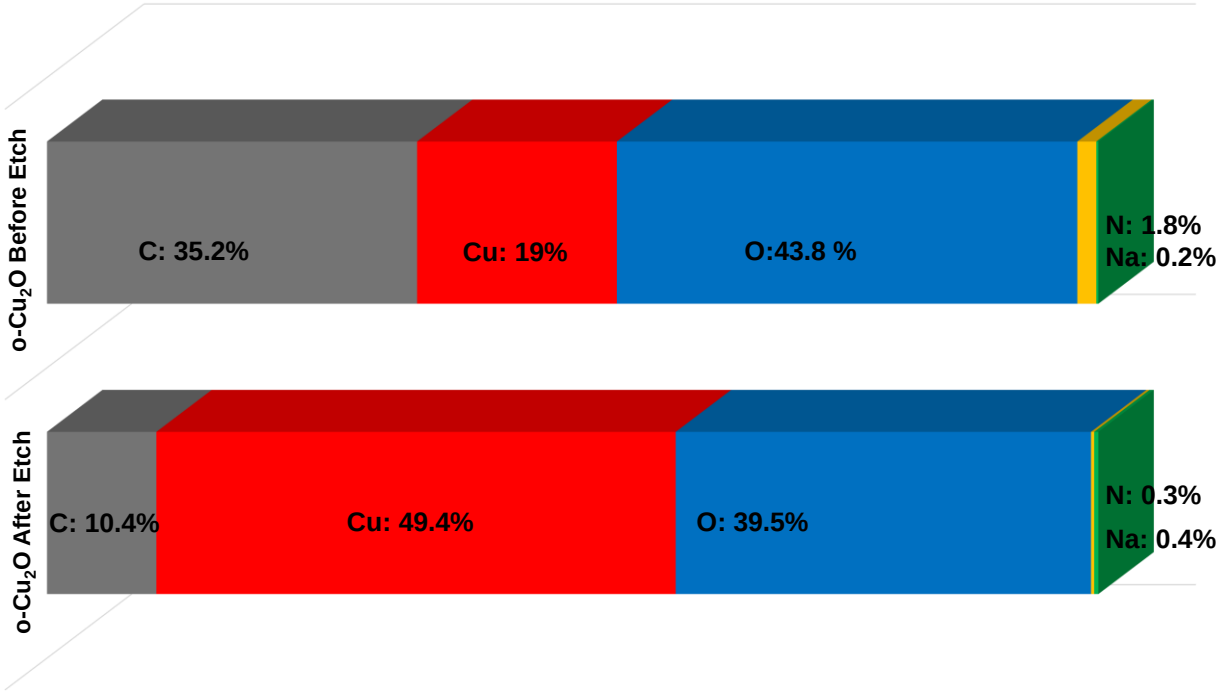


**Appendix B:** Surface atomic percentages from XPS survey spectra of o-$Cu_2O$ before and after etching.

## Appendix C: N 1s XPS of o-$Cu_2O$ before and after etching

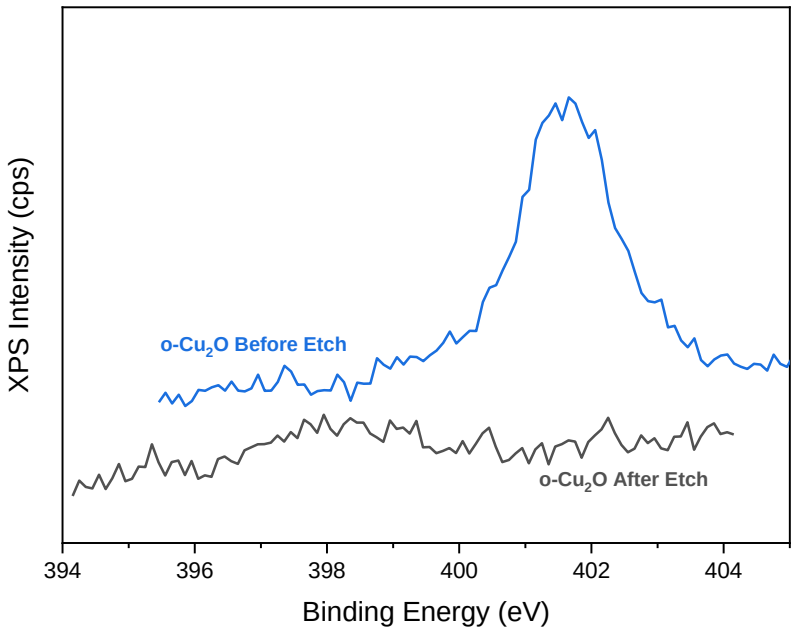


**Appendix C:** N 1s XPS of o-$Cu_2O$ before and after etching.

## Appendix D: Relative intensities m/z channels of the selected species

| m/z | 1 | 2 | 12 | 13 | 14 | 15 | 16 | 17 | 18 | 19 | 20 | 22 | 27 | 28 | 29 | 30 | 31 | 32 | 33 | 34 | 41 | 42 | 43 | 44 | 45 | 46 |
|---|---|---|---|---|---|---|---|---|---|---|---|---|---|---|---|---|---|---|---|---|---|---|---|---|---|---|
| $H_2$ | 2.09 | 100 | | | | | | | | | | | | | | | | | | | | | | | | |
| $H_2O$ | | | | | | | 0.89 | 21.3 | 100 | 0.51 | 0.31 | | | | | | | | | | | | | | | |
| CO | | | 4.72 | | | | 1.82 | | | | | | | 100 | 1.23 | | | | | | | | | | | |
| $CO_2$ | | | 8.67 | | | | 9.51 | | | | | 1.97 | | 9.8 | 0.1 | | | | | | | | | 100 | 1.2 | 0.6 |
| HCOH | | | 1 | 1 | 1 | 2 | | | | | | | | 24 | 100 | 58.3 | 0.5 | | | | | | | | | |
| $CH_3OH$ | | 0.3 | 0.2 | 0.6 | 1.86 | 12.4 | 0.1 | 0.3 | 0.7 | 0.1 | | | | 5.4 | 44.7 | 6.8 | 100 | 74.7 | 1.2 | 0.1 | | | | | | |

**Appendix D:** Relative intensities m/z channels of the selected species using reference QMS data available in the literature [116].

# Appendix E: c-$Cu_2O$ methanol TPD peak fits

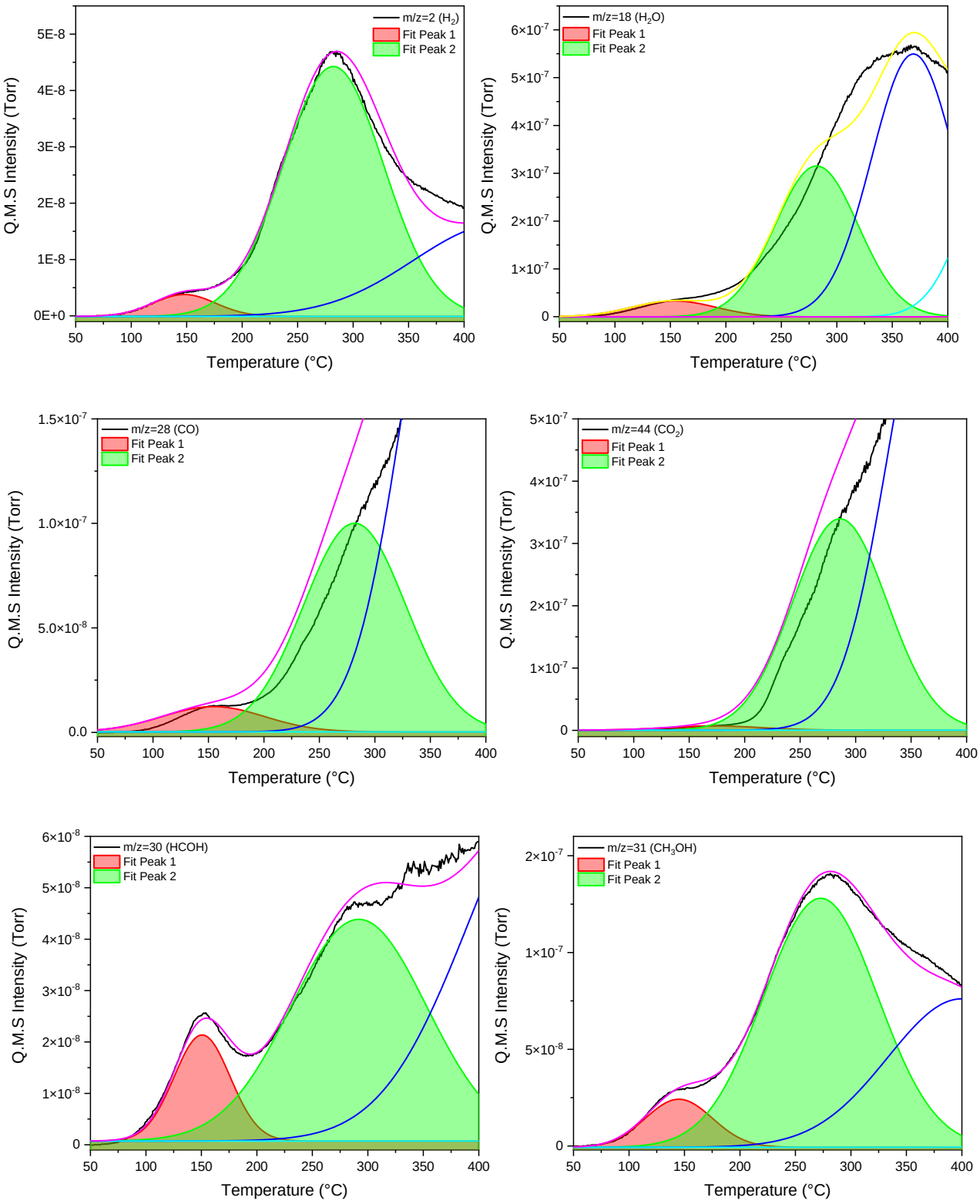


**Appendix E:** c-$Cu_2O$ methanol TPD peak fits.

# Appendix F: o-$Cu_2O$ methanol TPD peak fits

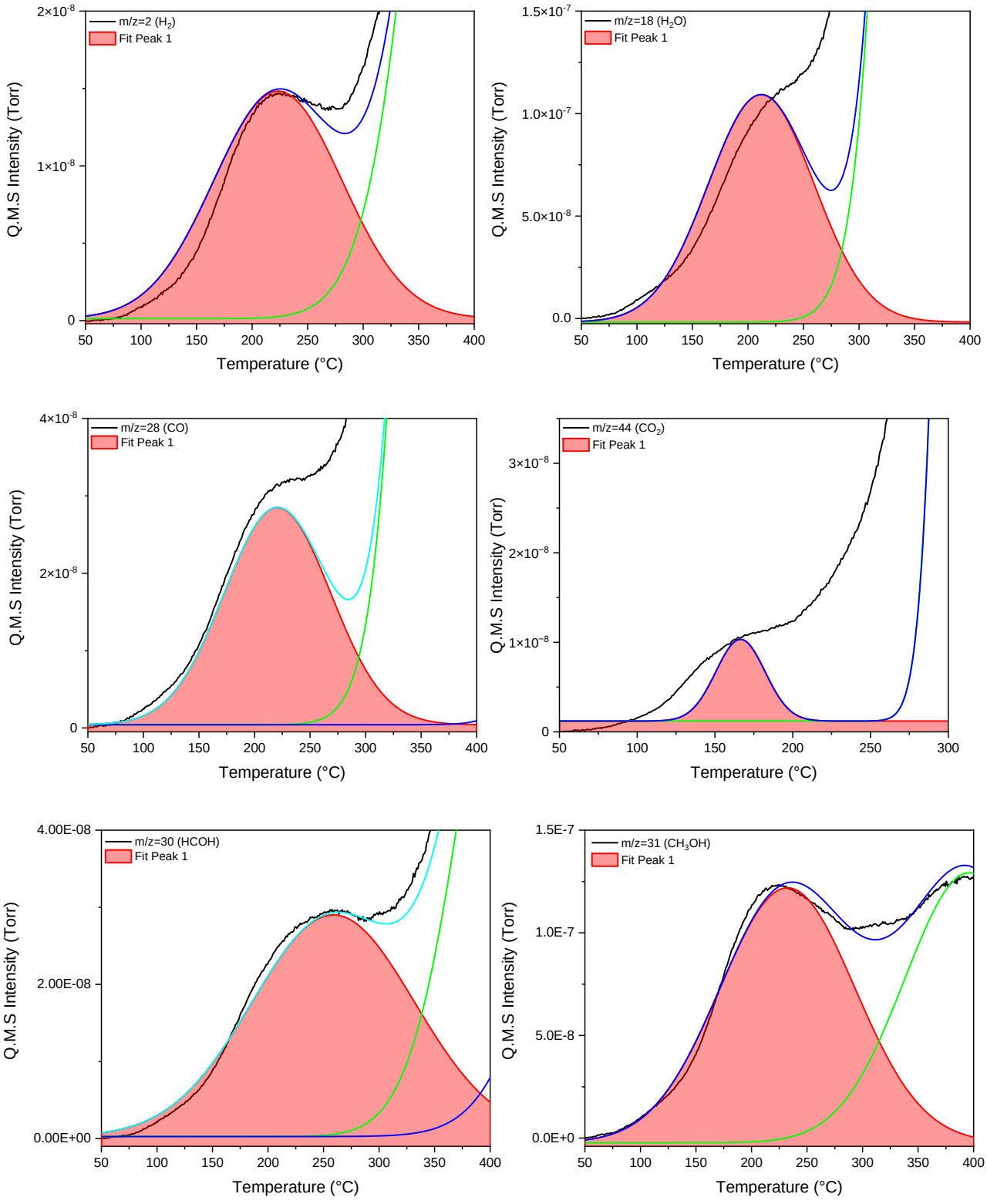


**Appendix F:** o-$Cu_2O$ methanol TPD peak fits.

# Appendix G: c-$Cu_2O$ formaldehyde TPD peak fits

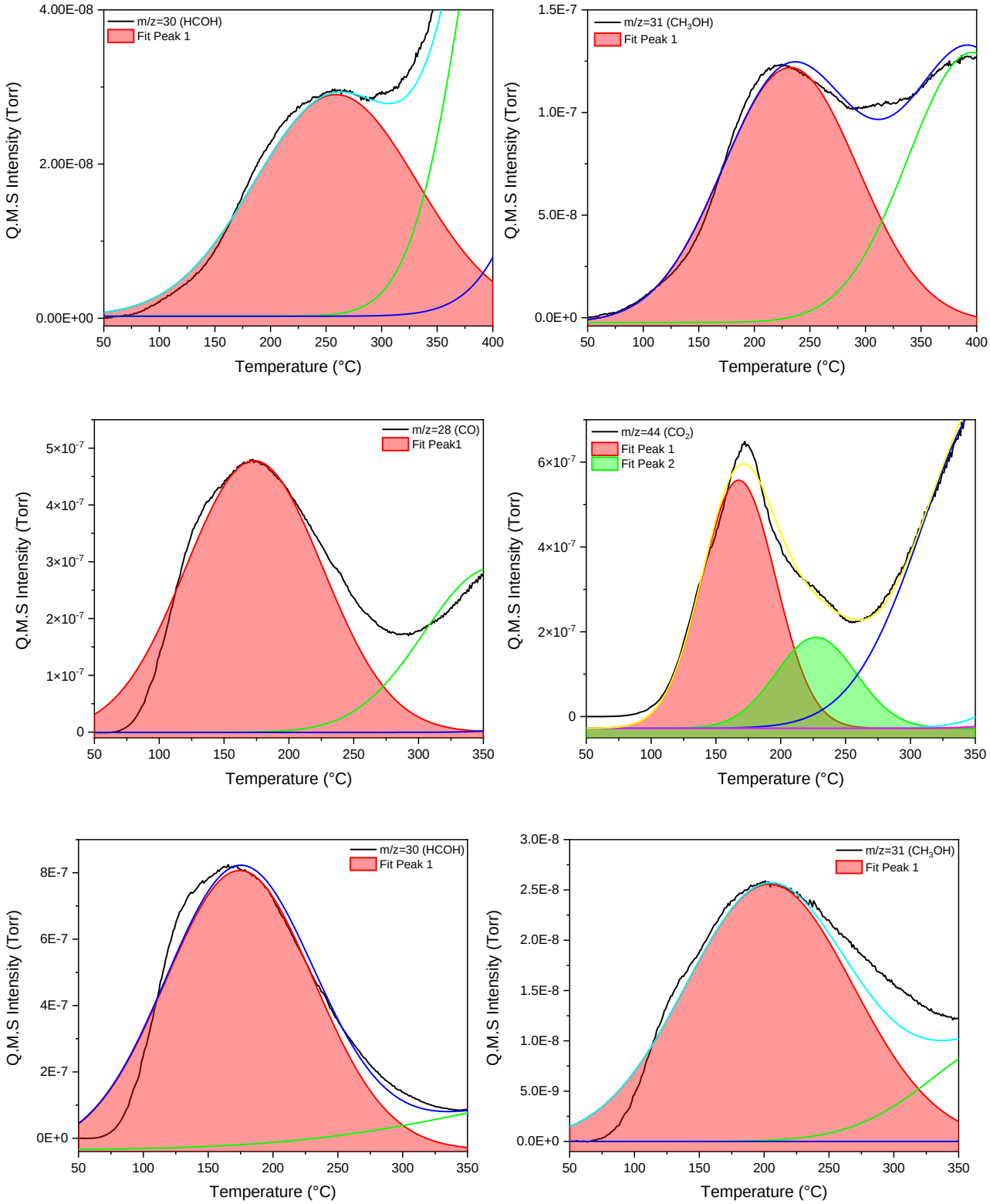


**Appendix G:** c-$Cu_2O$ formaldehyde TPD peak fits.

# Appendix H: o-$Cu_2O$ formaldehyde TPD peak fits

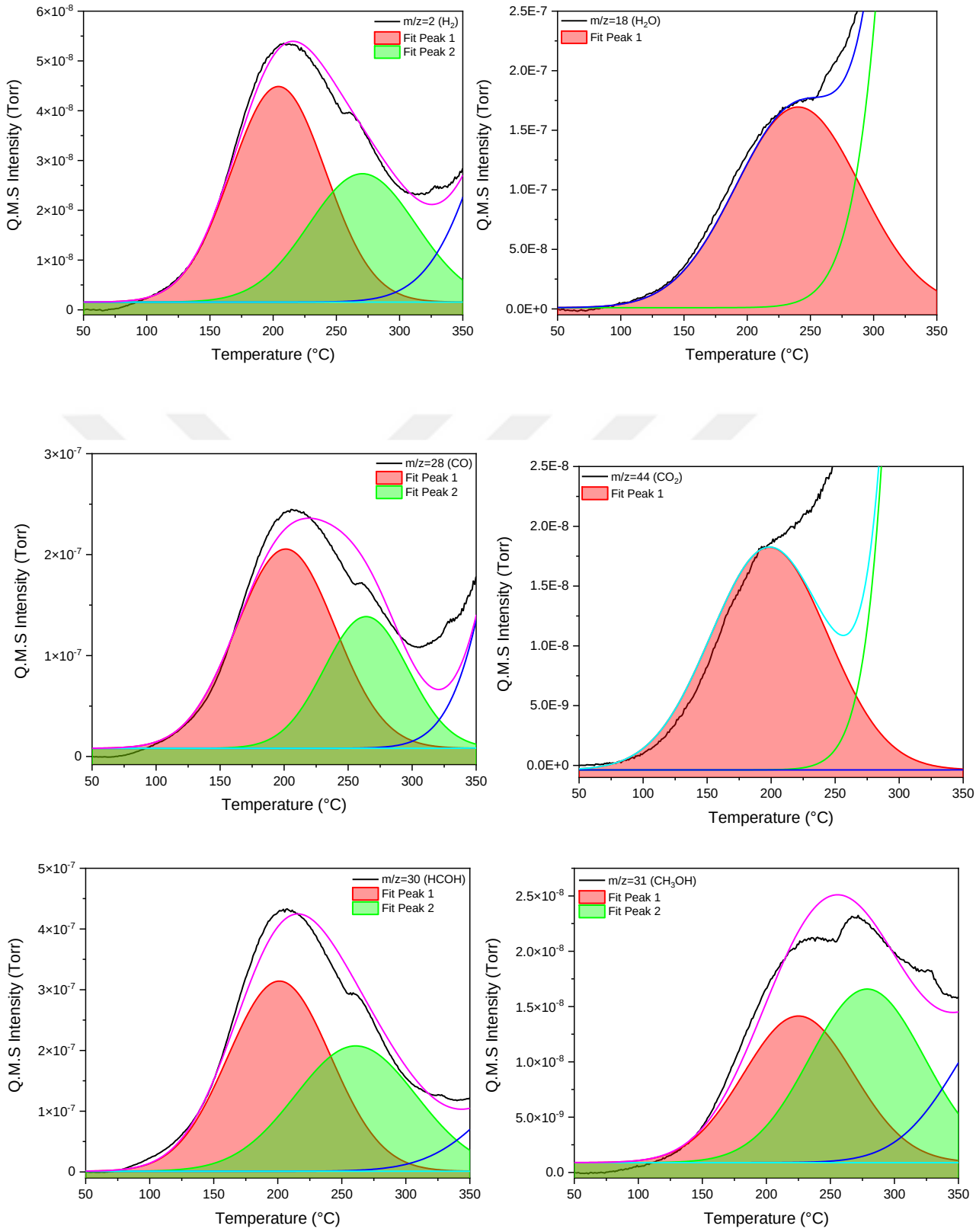


**Appendix H:** o-$Cu_2O$ formaldehyde TPD peak fits.

## Appendix I: Calculations for contributions from distinct species to the same m/z channel

For m/z = 30 there is also contribution from m/z = 31:

FA= Quantity of formaldehyde in m/z = 30

$$FA = (\int I_{30}\Delta T) - (\int I_{31}\Delta T) \times 0.068$$

For m/z = 28 there are contributions from m/z = 44, 31, 30:

CO = Quantity of CO in m/z = 28

$$CO = (\int I_{28}\Delta T) - (\int I_{44}\Delta T) \times 0.0975 - (\int I_{31}\Delta T) \times 0.0544 - FA \times 0.414$$

# References


1. Tabibian, S. S., & Sharifzadeh, M. (2023). Statistical and analytical investigation of methanol applications, production technologies, value-chain and economy with a special focus on renewable methanol. *Renewable and Sustainable Energy Reviews*, *179*, 113281. https://doi.org/10.1016/j.rser.2023.113281
2. Bertau, M., Offermanns, H., Plass, L., Schmidt, F., & Wernicke, H.-J. (Eds.). (2014). *Methanol: The Basic Chemical and Energy Feedstock of the Future*. Springer Berlin Heidelberg. https://doi.org/10.1007/978-3-642-39709-7
3. Yang, M., Fan, D., Wei, Y., Tian, P., & Liu, Z. (2019). Recent Progress in Methanol-to-Olefins (MTO) Catalysts. *Advanced Materials*, *31*(50). https://doi.org/10.1002/adma.201902181
4. Tian, P., Wei, Y., Ye, M., & Liu, Z. (2015). Methanol to Olefins (MTO): From Fundamentals to Commercialization. *ACS Catalysis*, *5*(3), 1922–1938. https://doi.org/10.1021/acscatal.5b00007
5. Ranjekar, A. M., & Yadav, G. D. (2021). Steam Reforming of Methanol for Hydrogen Production: A Critical Analysis of Catalysis, Processes, and Scope. *Industrial & Engineering Chemistry Research*, *60*(1), 89–113. https://doi.org/10.1021/acs.iecr.0c05041
6. Alias, M. S., Kamarudin, S. K., Zainoodin, A. M., & Masdar, M. S. (2020). Active direct methanol fuel cell: An overview. *International Journal of Hydrogen Energy*, *45*(38), 19620–19641. https://doi.org/10.1016/j.ijhydene.2020.04.202
7. Ben David, R., Ben Yaacov, A., Head, A. R., & Eren, B. (2022). Methanol Decomposition on Copper Surfaces under Ambient Conditions: Mechanism, Surface Kinetics, and Structure Sensitivity. *ACS Catalysis*, *12*(13), 7709–7718. https://doi.org/10.1021/acscatal.1c05933

8. Manzoli, M., Chiorino, A., & Boccuzzi, F. (2005). Decomposition and combined reforming of methanol to hydrogen: a FTIR and QMS study on Cu and Au catalysts supported on ZnO and TiO2. *Applied Catalysis B: Environmental*, *57*(3), 201–209. https://doi.org/10.1016/j.apcatb.2004.11.002
9. BOWKER, M. (1988). The mechanism of methanol synthesis on copper/zinc oxide/alumina catalysts. *Journal of Catalysis*, *109*(2), 263–273. https://doi.org/10.1016/0021-9517(88)90209-6
10. Ali, K. A., Abdullah, A. Z., & Mohamed, A. R. (2015). Recent development in catalytic technologies for methanol synthesis from renewable sources: A critical review. *Renewable and Sustainable Energy Reviews*, *44*, 508–518. https://doi.org/10.1016/j.rser.2015.01.010
11. Garcia, G., Arriola, E., Chen, W.-H., & de Luna, M. D. (2021). A comprehensive review of hydrogen production from methanol thermochemical conversion for sustainability. *Energy*, *217*, 119384. https://doi.org/10.1016/j.energy.2020.119384
12. Dalena, F., Senatore, A., Marino, A., Gordano, A., Basile, M., & Basile, A. (2018). Methanol Production and Applications: An Overview. In *Methanol* (pp. 3–28). Elsevier. https://doi.org/10.1016/B978-0-444-63903-5.00001-7
13. Kapran, A. Yu., & Orlyk, S. M. (2017). Hydrogen Production in Methanol Reforming on Modified Copper–Zinc Catalysts: A Review. *Theoretical and Experimental Chemistry*, *53*(1), 1–16. https://doi.org/10.1007/s11237-017-9495-9
14. Wu-Hsun Cheng. (1999). Development of Methanol Decomposition Catalysts for Production of H2 and CO. *Accounts of Chemical Research*, *32*(8), 685–691.
15. Thrane, J., Mentzel, U. v., Thorhauge, M., Høj, M., & Jensen, A. D. (2021). A Review and Experimental Revisit of Alternative Catalysts for Selective Oxidation of Methanol to Formaldehyde. *Catalysts*, *11*(11), 1329. https://doi.org/10.3390/catal11111329

16. Behrens, M., Studt, F., Kasatkin, I., Kühl, S., Hävecker, M., Abild-Pedersen, F., Zander, S., Girgsdies, F., Kurr, P., Kniep, B.-L., Tovar, M., Fischer, R. W., Nørskov, J. K., & Schlögl, R. (2012). The Active Site of Methanol Synthesis over Cu/ZnO/Al $_2$ O $_3$ Industrial Catalysts. *Science*, *336*(6083), 893–897. https://doi.org/10.1126/science.1219831
17. Yong, S. T., Ooi, C. W., Chai, S. P., & Wu, X. S. (2013). Review of methanol reforming-Cu-based catalysts, surface reaction mechanisms, and reaction schemes. *International Journal of Hydrogen Energy*, *38*(22), 9541–9552. https://doi.org/10.1016/j.ijhydene.2013.03.023
18. Lin, S. D., Cheng, H., & Hsiao, T. C. (2011). In situ DRIFTS study on the methanol oxidation by lattice oxygen over Cu/ZnO catalyst. *Journal of Molecular Catalysis A: Chemical*, *342–343*, 35–40. https://doi.org/10.1016/j.molcata.2011.04.007
19. Manzoli, M., Chiorino, A., & Boccuzzi, F. (2005). Decomposition and combined reforming of methanol to hydrogen: a FTIR and QMS study on Cu and Au catalysts supported on ZnO and TiO2. *Applied Catalysis B: Environmental*, *57*(3), 201–209. https://doi.org/10.1016/j.apcatb.2004.11.002
20. Millar, G. J., Rochester, C. H., & Waugh, K. C. (1991). Infrared study of the adsorption of methanol on oxidized and reduced Cu/SiO2 catalysts. *Journal of the Chemical Society, Faraday Transactions*, *87*(17), 2795. https://doi.org/10.1039/ft9918702795
21. Poulston, S., Rowbotham, E., Stone, P., Parlett, P., & Bowker, M. (1998). Temperature-programmed desorption studies of methanol and formic acid decomposition on copper oxide surfaces. *Catalysis Letters*, *52*(1/2), 63–67. https://doi.org/10.1023/A:1019007100649

22. Millar, G. J., Rochester, C. H., & Waugh, K. C. (1995). An FTIR Study of the Adsorption of Formic Acid and Formaldehyde on Potassium-Promoted Cu/SiO2 Catalysts. *Journal of Catalysis*, *155*(1), 52–58. https://doi.org/10.1006/jcat.1995.1187
23. Edwards, J. F., & Schrader, G. L. (1985). Methanol, formaldehyde, and formic acid adsorption on methanol synthesis catalysts. *The Journal of Physical Chemistry*, *89*(5), 782–788. https://doi.org/10.1021/j100251a015
24. Zhang, R., Sun, Y., & Peng, S. (2002). In situ FTIR studies of methanol adsorption and dehydrogenation over Cu/SiO2 catalyst. *Fuel*, *81*(11–12), 1619–1624. https://doi.org/10.1016/S0016-2361(02)00085-6
25. Fisher, I. A., & Bell, A. T. (1999). A Mechanistic Study of Methanol Decomposition over Cu/SiO2, ZrO2/SiO2, and Cu/ZrO2/SiO2. *Journal of Catalysis*, *184*(2), 357–376. https://doi.org/10.1006/jcat.1999.2420
26. Wang, X., Arvidsson, A. A., Cichocka, M. O., Zou, X., Martin, N. M., Nilsson, J., Carlson, S., Gustafson, J., Skoglundh, M., Hellman, A., & Carlsson, P.-A. (2017). Methanol Desorption from Cu-ZSM-5 Studied by *In Situ* Infrared Spectroscopy and First-Principles Calculations. *The Journal of Physical Chemistry C*, *121*(49), 27389–27398. https://doi.org/10.1021/acs.jpcc.7b07067
27. Clarke, D. B., Lee, D. K., Sandoval, M. J., & Bell, A. T. (1994). Infrared Studies of the Mechanism of Methanol Decomposition on Cu/SiO2. *Journal of Catalysis*, *150*(1), 81–93. https://doi.org/10.1006/jcat.1994.1324
28. Kukulska-Zając, E., & Datka, J. (2007). Transformations of Formaldehyde Molecules in Cu−ZSM-5 Zeolites. *The Journal of Physical Chemistry C*, *111*(8), 3471–3475. https://doi.org/10.1021/jp066732g

29. Ortelli, E. E., Weigel, J. M., & Wokaun, A. (1998). Methanol synthesis pathway over Cu/ZrO2 catalysts: a time-resolved DRIFT 13C-labelling experiment. *Catalysis Letters*, *54*(1/2), 41–48. https://doi.org/10.1023/A:1019032022881
30. ben David, R., ben Yaacov, A., & Eren, B. (2021). Effect of Surface Orientation on Methanol Adsorption and Thermally Induced Structural Transformations on Copper Surfaces. *The Journal of Physical Chemistry C*, *125*(11), 6099–6107. https://doi.org/10.1021/acs.jpcc.0c10278
31. Camplin, J. P., & McCash, E. M. (1996). A RAIRS study of methoxy and ethoxy on oxidised Cu(100). *Surface Science*, *360*(1–3), 229–241. https://doi.org/10.1016/0039-6028(96)00641-3
32. Ellis, T. H., & Wang, H. (1994). Isolating the Reaction Steps in the Formation of Methoxy on Cu(100). *Langmuir*, *10*(11), 4083–4088. https://doi.org/10.1021/la00023a030
33. Singnurkar, P., Bako, I., Koch, H. P., Demirci, E., Winkler, A., & Schennach, R. (2008). DFT and RAIRS Investigations of Methanol on Cu(110) and on Oxygen-Modified Cu(110). *The Journal of Physical Chemistry C*, *112*(36), 14034–14040. https://doi.org/10.1021/jp802488n
34. Chesters, M. A., & McCash, E. M. (1987). The adsorption and reaction of methanol on oxidized copper(111) studied by Fourier transform reflection-absorption infrared spectroscopy. *Spectrochimica Acta Part A: Molecular Spectroscopy*, *43*(12), 1625–1630. https://doi.org/10.1016/S0584-8539(87)80059-4
35. Takeyasu, K., Sawaki, Y., Imabayashi, T., Putra, S. E. M., Halim, H. H., Quan, J., Hamamoto, Y., Hamada, I., Morikawa, Y., Kondo, T., Fujitani, T., & Nakamura, J. (2022). Hydrogenation of Formate Species Using Atomic Hydrogen on a Cu(111)

Model Catalyst. *Journal of the American Chemical Society*, *144*(27), 12158–12166. https://doi.org/10.1021/jacs.2c02797

36. Mudalige, K., & Trenary, M. (2001). The Formation of Methoxy from Methanol on an Oxygen Covered Cu(100) Surface at Temperatures of 90−200 K. *The Journal of Physical Chemistry B*, *105*(18), 3823–3827. https://doi.org/10.1021/jp003611m
37. Mudalige, K., & Trenary, M. (2002). Identification of formate from methanol oxidation on Cu() with infrared spectroscopy. *Surface Science*, *504*, 208–214. https://doi.org/10.1016/S0039-6028(02)01101-9
38. Sexton, B. A., Hughes, A. E., & Avery, N. R. (1985). A spectroscopic study of the adsorption and reactions of methanol, formaldehyde and methyl formate on clean and oxygenated Cu(110) surfaces. *Surface Science*, *155*(1), 366–386. https://doi.org/10.1016/0039-6028(85)90423-6
39. Grabow, L. C., & Mavrikakis, M. (2011). Mechanism of Methanol Synthesis on Cu through $CO_2$ and CO Hydrogenation. *ACS Catalysis*, *1*(4), 365–384. https://doi.org/10.1021/cs200055d
40. Fajín, J. L. C., & Cordeiro, M. N. D. S. (2022). Insights into the Mechanism of Methanol Steam Reforming for Hydrogen Production over Ni–Cu-Based Catalysts. *ACS Catalysis*, *12*(1), 512–526. https://doi.org/10.1021/acscatal.1c03997
41. Busca, G. (1996). Infrared studies of the reactive adsorption of organic molecules over metal oxides and of the mechanisms of their heterogeneously-catalyzed oxidation. *Catalysis Today*, *27*(3–4), 457–496. https://doi.org/10.1016/0920-5861(95)00162-X
42. Prieto, G., & Schüth, F. (2015). Bridging the gap between insightful simplicity and successful complexity: From fundamental studies on model systems to technical catalysts. *Journal of Catalysis*, *328*, 59–71. https://doi.org/10.1016/j.jcat.2014.12.009

43. Chen, S., Xiong, F., & Huang, W. (2019). Surface chemistry and catalysis of oxide model catalysts from single crystals to nanocrystals. *Surface Science Reports*, *74*(4), 100471. https://doi.org/10.1016/j.surfrep.2019.100471

44. Huang, W. (2016). Oxide Nanocrystal Model Catalysts. *Accounts of Chemical Research*, *49*(3), 520–527. https://doi.org/10.1021/acs.accounts.5b00537

45. Huang, W. (2023). Uniform Catalytic Nanocrystals: From Model Catalysts to Efficient Catalysts. *Accounts of Materials Research*, *4*(4), 373–384. https://doi.org/10.1021/accountsmr.2c00260

46. Zhang, Z., You, R., & Huang, W. (2022). $Cu_2O$ Nanocrystal Model Catalysts. *Chinese Journal of Chemistry*, *40*(7), 846–855. https://doi.org/10.1002/cjoc.202100805

47. Zhang, Z., Wu, H., Yu, Z., Song, R., Qian, K., Chen, X., Tian, J., Zhang, W., & Huang, W. (2019). Site-Resolved $Cu_2O$ Catalysis in the Oxidation of CO. *Angewandte Chemie International Edition*, *58*(13), 4276–4280. https://doi.org/10.1002/anie.201814258

48. Hua, Q., Cao, T., Gu, X., Lu, J., Jiang, Z., Pan, X., Luo, L., Li, W., & Huang, W. (2014). Crystal-Plane-Controlled Selectivity of $Cu_2O$ Catalysts in Propylene Oxidation with Molecular Oxygen. *Angewandte Chemie International Edition*, *53*(19), 4856–4861. https://doi.org/10.1002/anie.201402374

49. Zhang, Z., Wang, S.-S., Song, R., Cao, T., Luo, L., Chen, X., Gao, Y., Lu, J., Li, W.-X., & Huang, W. (2017). The most active Cu facet for low-temperature water gas shift reaction. *Nature Communications*, *8*(1), 488. https://doi.org/10.1038/s41467-017-00620-6

50. Kumar Sahu, A., Pokhriyal, M., Upadhyayula, S., & Zhao, X. S. (2022). Modulating Charge Carrier Dynamics among Anisotropic Crystal Facets of $Cu_2O$ for Enhanced $CO_2$ Photoreduction. *The Journal of Physical Chemistry C*, *126*(31), 13094–13104. https://doi.org/10.1021/acs.jpcc.2c02306

51. Siddiqui, M. K., Manzoor, S., Ahmad, S., & Kaabar, M. K. A. (2021). On Computation and Analysis of Entropy Measures for Crystal Structures. *Mathematical Problems in Engineering*, *2021*, 1–16. https://doi.org/10.1155/2021/9936949

52. Sun, S., Zhang, X., Yang, Q., Liang, S., Zhang, X., & Yang, Z. (2018). Cuprous oxide (Cu2O) crystals with tailored architectures: A comprehensive review on synthesis, fundamental properties, functional modifications and applications. *Progress in Materials Science*, *96*, 111–173. https://doi.org/10.1016/j.pmatsci.2018.03.006

53. Zhang, Z., Zhang, J., Jia, A.-P., Lu, J.-Q., & Huang, W. (2020). Morphology-Dependent CO Reduction Kinetics and Surface Copper Species Evolution of $Cu_2O$ Nanocrystals. *The Journal of Physical Chemistry C*, *124*(39), 21568–21576. https://doi.org/10.1021/acs.jpcc.0c06425

54. Bao, H., Zhang, W., Shang, D., Hua, Q., Ma, Y., Jiang, Z., Yang, J., & Huang, W. (2010). Shape-Dependent Reducibility of Cuprous Oxide Nanocrystals. *The Journal of Physical Chemistry C*, *114*(14), 6676–6680. https://doi.org/10.1021/jp101617z

55. Liu, X.-W., Wang, F.-Y., Zhen, F., & Huang, J.-R. (2012). In situ growth of Au nanoparticles on the surfaces of Cu2O nanocubes for chemical sensors with enhanced performance. *RSC Advances*, *2*(20), 7647. https://doi.org/10.1039/c2ra20789c

56. Ren, Q., Zhang, N., Dong, Z., Zhang, L., Chen, X., & Luo, L. (2023). Structural evolution of Cu2O nanocube electrocatalysts for the CO2 reduction reaction. *Nano Energy*, *106*, 108080. https://doi.org/10.1016/j.nanoen.2022.108080

57. Jiang, D., Xing, C., Liang, X., Shao, L., & Chen, M. (2016). Synthesis of cuprous oxide with morphological evolution from truncated octahedral to spherical structures and their size and shape-dependent photocatalytic activities. *Journal of Colloid and Interface Science*, *461*, 25–31. https://doi.org/10.1016/j.jcis.2015.09.034

58. Hua, Q., Cao, T., Gu, X., Lu, J., Jiang, Z., Pan, X., Luo, L., Li, W., & Huang, W. (2014). Crystal-Plane-Controlled Selectivity of $Cu_2O$ Catalysts in Propylene Oxidation with Molecular Oxygen. *Angewandte Chemie*, *126*(19), 4956–4961. https://doi.org/10.1002/ange.201402374

59. Lamberti, C., Bordiga, S., Bonino, F., Prestipino, C., Berlier, G., Capello, L., D'Acapito, F., Llabrés i Xamena, F. X., & Zecchina, A. (2003). Determination of the oxidation and coordination state of copper on different Cu-based catalysts by XANES spectroscopy in situ or in operando conditions. *Phys. Chem. Chem. Phys.*, *5*(20), 4502–4509. https://doi.org/10.1039/B305810G

60. Kordus, D., Jelic, J., Lopez Luna, M., Divins, N. J., Timoshenko, J., Chee, S. W., Rettenmaier, C., Kröhnert, J., Kühl, S., Trunschke, A., Schlögl, R., Studt, F., & Roldan Cuenya, B. (2023). Shape-Dependent $CO_2$ Hydrogenation to Methanol over $Cu_2O$ Nanocubes Supported on ZnO. *Journal of the American Chemical Society*, *145*(5), 3016–3030. https://doi.org/10.1021/jacs.2c11540

61. Sharma, A., Varshney, M., Park, J., Ha, T.-K., Chae, K.-H., & Shin, H.-J. (2015). XANES, EXAFS and photocatalytic investigations on copper oxide nanoparticles and nanocomposites. *RSC Advances*, *5*(28), 21762–21771. https://doi.org/10.1039/C4RA16217J

62. Wang, J., Gan, L., Zhang, Q., Reddu, V., Peng, Y., Liu, Z., Xia, X., Wang, C., & Wang, X. (2019). A Water-Soluble Cu Complex as Molecular Catalyst for Electrocatalytic $CO_2$ Reduction on Graphene-Based Electrodes. *Advanced Energy Materials*, *9*(3). https://doi.org/10.1002/aenm.201803151

63. Ho, W., Tay, Q., Qi, H., Huang, Z., Li, J., & Chen, Z. (2017). Photocatalytic and Adsorption Performances of Faceted Cuprous Oxide (Cu2O) Particles for the Removal

of Methyl Orange (MO) from Aqueous Media. *Molecules*, *22*(4), 677. https://doi.org/10.3390/molecules22040677

64. Debbichi, L., Marco de Lucas, M. C., Pierson, J. F., & Krüger, P. (2012). Vibrational Properties of CuO and $Cu_4O_3$ from First-Principles Calculations, and Raman and Infrared Spectroscopy. *The Journal of Physical Chemistry C*, *116*(18), 10232–10237. https://doi.org/10.1021/jp303096m
65. Chang, Y.-N. (1992). Fourier Transform Infrared (FTIR) Analysis of Copper Oxide Thin Films Prepared by Metal Organic Chemical Vapor Deposition (MOCVD). *MRS Proceedings*, *293*, 443. https://doi.org/10.1557/PROC-293-443
66. Gupta, D., Meher, S. R., Illyaskutty, N., & Alex, Z. C. (2018). Facile synthesis of Cu2O and CuO nanoparticles and study of their structural, optical and electronic properties. *Journal of Alloys and Compounds*, *743*, 737–745. https://doi.org/10.1016/j.jallcom.2018.01.181
67. Shoeib, M. A., Abdelsalam, O. E., Khafagi, M. G., & Hammam, R. E. (2012). Synthesis of Cu2O nanocrystallites and their adsorption and photocatalysis behavior. *Advanced Powder Technology*, *23*(3), 298–304. https://doi.org/10.1016/j.apt.2011.04.001
68. Balık, M., Bulut, V., & Erdogan, I. Y. (2019). Optical, structural and phase transition properties of Cu2O, CuO and Cu2O/CuO: Their photoelectrochemical sensor applications. *International Journal of Hydrogen Energy*, *44*(34), 18744–18755. https://doi.org/10.1016/j.ijhydene.2018.08.159
69. Yohannan Panicker, C., Tresa Varghese, H., & Philip, D. (2006). FT-IR, FT-Raman and SERS spectra of Vitamin C. *Spectrochimica Acta Part A: Molecular and Biomolecular Spectroscopy*, *65*(3–4), 802–804. https://doi.org/10.1016/j.saa.2005.12.044
70. Hvoslef, J., Klæboe, P., Pettersson, B., Svensson, S., Koskikallio, J., & Kachi, S. (1971). Vibrational Spectroscopic Studies of L-Ascorbic Acid and Sodium Ascorbate. *Acta*

*Chemica Scandinavica*, *25*, 3043–3053. https://doi.org/10.3891/acta.chem.scand.25-3043

71. Rahma, A., Munir, M. M., Khairurrijal, Prasetyo, A., Suendo, V., & Rachmawati, H. (2016). Intermolecular Interactions and the Release Pattern of Electrospun Curcumin-Polyvinyl(pyrrolidone) Fiber. *Biological & Pharmaceutical Bulletin*, *39*(2), 163–173. https://doi.org/10.1248/bpb.b15-00391
72. Safo, I. A., Werheid, M., Dosche, C., & Oezaslan, M. (2019). The role of polyvinylpyrrolidone (PVP) as a capping and structure-directing agent in the formation of Pt nanocubes. *Nanoscale Advances*, *1*(8), 3095–3106. https://doi.org/10.1039/C9NA00186G
73. Shahmiri, M., Ibrahim, N. A., Yunus, W. M. Z. W., Shameli, K., Zainuddin, N., & Jahangirian, H. (2013). Synthesis and Characterization of CuO Nanosheets in Polyvinylpyrrolidone by Quick Precipitation Method. *Advanced Science, Engineering and Medicine*, *5*(3), 193–197. https://doi.org/10.1166/asem.2013.1227
74. Jiang, P., Prendergast, D., Borondics, F., Porsgaard, S., Giovanetti, L., Pach, E., Newberg, J., Bluhm, H., Besenbacher, F., & Salmeron, M. (2013). Experimental and theoretical investigation of the electronic structure of Cu2O and CuO thin films on Cu(110) using x-ray photoelectron and absorption spectroscopy. *The Journal of Chemical Physics*, *138*(2). https://doi.org/10.1063/1.4773583
75. Gao, Y., Zhang, L., van Hoof, A. J. F., & Hensen, E. J. M. (2020). On the surface-dependent oxidation of Cu2O during CO oxidation: Cu2+ is more active than Cu+. *Applied Catalysis A: General*, *602*, 117712. https://doi.org/10.1016/j.apcata.2020.117712
76. Svintsitskiy, D. A., Kardash, T. Yu., Stonkus, O. A., Slavinskaya, E. M., Stadnichenko, A. I., Koscheev, S. v., Chupakhin, A. P., & Boronin, A. I. (2013). In Situ XRD, XPS,

TEM, and TPR Study of Highly Active in CO Oxidation CuO Nanopowders. *The Journal of Physical Chemistry C*, *117*(28), 14588–14599. https://doi.org/10.1021/jp403339r

77. S. Poulston, P. M. Parlett, P. Stone, & M. Bowker. (1996). Surface Oxidation and Reduction of CuO and Cu2O Studied Using XPS and XAES. *Surf. Interface Anal.*, *24*, 811–820.
78. Martin, L., Martinez, H., Poinot, D., Pecquenard, B., & le Cras, F. (2013). Comprehensive X-ray Photoelectron Spectroscopy Study of the Conversion Reaction Mechanism of CuO in Lithiated Thin Film Electrodes. *The Journal of Physical Chemistry C*, *117*(9), 4421–4430. https://doi.org/10.1021/jp3119633
79. Davydov, A. (2003). *Molecular Spectroscopy of Oxide Catalyst Surfaces*. Wiley. https://doi.org/10.1002/0470867981
80. Tsoncheva, T., Genova, I., Stoyanova, M., Pohl, M.-M., Nickolov, R., Dimitrov, M., Sarcadi-Priboczki, E., Mihaylov, M., Kovacheva, D., & Hadjiivanov, K. (2014). Effect of mesoporous silica topology on the formation of active sites in copper supported catalysts for methanol decomposition. *Applied Catalysis B: Environmental*, *147*, 684–697. https://doi.org/10.1016/j.apcatb.2013.10.002
81. Dandekar, A., & Vannice, M. A. (1998). Determination of the Dispersion and Surface Oxidation States of Supported Cu Catalysts. *Journal of Catalysis*, *178*(2), 621–639. https://doi.org/10.1006/jcat.1998.2190
82. Hadjiivanov, K. I., & Vayssilov, G. N. (2002). *Characterization of oxide surfaces and zeolites by carbon monoxide as an IR probe molecule* (pp. 307–511). https://doi.org/10.1016/S0360-0564(02)47008-3
83. Liu, Z., Rittermeier, A., Becker, M., Kähler, K., Löffler, E., & Muhler, M. (2011). High-Pressure CO Adsorption on Cu-Based Catalysts: Zn-Induced Formation of Strongly

Bound CO Monitored by ATR-IR Spectroscopy. *Langmuir*, *27*(8), 4728–4733. https://doi.org/10.1021/la2000766

84. Palomino, G. T., Bordiga, S., Zecchina, A., Marra, G. L., & Lamberti, C. (2000). XRD, XAS, and IR Characterization of Copper-Exchanged Y Zeolite. *The Journal of Physical Chemistry B*, *104*(36), 8641–8651. https://doi.org/10.1021/jp000584r
85. Huang, W. (2016). Oxide Nanocrystal Model Catalysts. *Accounts of Chemical Research*, *49*(3), 520–527. https://doi.org/10.1021/acs.accounts.5b00537
86. Chen, S., Cao, T., Gao, Y., Li, D., Xiong, F., & Huang, W. (2016). Probing Surface Structures of $CeO_2$, $TiO_2$, and $Cu_2O$ Nanocrystals with CO and $CO_2$ Chemisorption. *The Journal of Physical Chemistry C*, *120*(38), 21472–21485. https://doi.org/10.1021/acs.jpcc.6b06158
87. Abdel-Mageed, A. M., Cisneros, S., Mosrati, J., Atia, H., Vuong, T. H., Rockstroh, N., Wohlrab, S., Brückner, A., & Rabeah, J. (2023). Controlling Activity of Heterogeneous Cu Single-Atom Catalysts by Fine-Tuning the Redox Properties of $CeO_2$-$TiO_2$ Supports. *ChemCatChem*, *15*(8). https://doi.org/10.1002/cctc.202201669
88. Impeng, S., Salaya-Gerónimo, E., Kunkel, B., Bartling, S., Faungnawakij, K., Rungtaweevoranit, B., & Abdel-Mageed, A. M. (2024). Mechanism and selectivity of MOF-supported Cu single-atom catalysts for preferential CO oxidation. *Journal of Materials Chemistry A*, *12*(5), 3084–3095. https://doi.org/10.1039/D3TA05047E
89. Diyu Zhang, Charlotte Jansen, Otto T. Berg, Joost M. Bakker, Jörg Meyer, Aart W. Kleyn, & Ludo B. F. Juurlink. (2022). RAIRS Characterization of CO and O Coadsorption on Cu(111). *The Journal of Physical Chemistry C*, *126*(31), 13114–13121.

90. Villarroel-Rocha, J., & Gil, A. (2024). Modeling the temperature-programmed reduction of metal oxide catalysts by considering the particle-size distribution effect. *Chemical Engineering Journal*, *487*, 150722. https://doi.org/10.1016/j.cej.2024.150722
91. Rousseau, S., Marie, O., Bazin, P., Daturi, M., Verdier, S., & Harlé, V. (2010). Investigation of Methanol Oxidation over Au/Catalysts Using Operando IR Spectroscopy: Determination of the Active Sites, Intermediate/Spectator Species, and Reaction Mechanism. *Journal of the American Chemical Society*, *132*(31), 10832–10841. https://doi.org/10.1021/ja1028809
92. Deitermann, M., Sato, T., Haver, Y., Schnegg, A., Muhler, M., & Mei, B. T. (2024). Mechanistic understanding of the thermal-assisted photocatalytic oxidation of methanol-to-formaldehyde with water vapor over Pt/$SrTiO_3$. *Physical Chemistry Chemical Physics*, *26*(20), 14960–14969. https://doi.org/10.1039/D4CP01106F
93. Wu, Z., Li, M., Mullins, D. R., & Overbury, S. H. (2012). Probing the Surface Sites of $CeO_2$ Nanocrystals with Well-Defined Surface Planes via Methanol Adsorption and Desorption. *ACS Catalysis*, *2*(11), 2224–2234. https://doi.org/10.1021/cs300467p
94. Busca, G., Guidetti, R., & Lorenzelli, V. (1990). Fourier-transform infrared study of the surface properties of cobalt oxides. *Journal of the Chemical Society, Faraday Transactions*, *86*(6), 989. https://doi.org/10.1039/ft9908600989
95. Ouyang, F., Yao, S., Tabata, K., & Suzuki, E. (2000). Infrared identification of reaction route from adsorbed species derived from adsorption of methanol on SnO2. *Applied Surface Science*, *158*(1–2), 28–31. https://doi.org/10.1016/S0169-4332(99)00585-1
96. Fan, Q., Pu, C., & Smotkin, E. S. (1996). In Situ Fourier Transform Infrared-Diffuse Reflection Spectroscopy of Direct Methanol Fuel Cell Anodes and Cathodes. *Journal of The Electrochemical Society*, *143*(10), 3053–3057. https://doi.org/10.1149/1.1837163

97. CHEN, T., WU, G., FENG, Z., HU, G., SU, W., YING, P., & LI, C. (2008). In Situ FT-IR Study of Photocatalytic Decomposition of Formic Acid to Hydrogen on Pt/TiO2 Catalyst. *Chinese Journal of Catalysis*, *29*(2), 105–107. https://doi.org/10.1016/S1872-2067(08)60019-4

98. Kecskés, T., Németh, R., Raskó, J., & Kiss, J. (2005). New reaction route of HCOOH catalytic decomposition. *Vacuum*, *80*(1–3), 64–68. https://doi.org/10.1016/j.vacuum.2005.07.014

99. RASKO, J. (2004). Adsorption and reaction of formaldehyde on TiO2-supported Rh catalysts studied by FTIR and mass spectrometry. *Journal of Catalysis*, *226*(1), 183–191. https://doi.org/10.1016/j.jcat.2004.05.024

100. Busca, G., Lamotte, J., Lavalley, J. C., & Lorenzelli, V. (1987). FT-IR study of the adsorption and transformation of formaldehyde on oxide surfaces. *Journal of the American Chemical Society*, *109*(17), 5197–5202. https://doi.org/10.1021/ja00251a025

101. Manzoli, M., Chiorino, A., & Boccuzzi, F. (2005). Decomposition and combined reforming of methanol to hydrogen: a FTIR and QMS study on Cu and Au catalysts supported on ZnO and TiO2. *Applied Catalysis B: Environmental*, *57*(3), 201–209. https://doi.org/10.1016/j.apcatb.2004.11.002

102. Sim, W. S., Gardner, P., & King, D. A. (1995). Structure and Reactivity of the Surface Methoxy Species on Ag{111}. *The Journal of Physical Chemistry*, *99*(43), 16002–16010. https://doi.org/10.1021/j100043a046

103. Idriss, H., Hindermann, J. P., Kieffer, R., Kiennemann, A., Vallet, A., Chauvin, C., Lavalley, J. C., & Chaumette, P. (1987). Characterization of dioxymethylene species over cu-zn catalysts. *Journal of Molecular Catalysis*, *42*(2), 205–213. https://doi.org/10.1016/0304-5102(87)85027-7

104. Karatok, M., Sensoy, M. G., Vovk, E. I., Ustunel, H., Toffoli, D., & Ozensoy, E. (2021). Formaldehyde Selectivity in Methanol Partial Oxidation on Silver: Effect of Reactive Oxygen Species, Surface Reconstruction, and Stability of Intermediates. *ACS Catalysis*, *11*(10), 6200–6209. https://doi.org/10.1021/acscatal.1c00344

105. Hauchecorne, B., Terrens, D., Verbruggen, S., Martens, J. A., van Langenhove, H., Demeestere, K., & Lenaerts, S. (2011). Elucidating the photocatalytic degradation pathway of acetaldehyde: An FTIR in situ study under atmospheric conditions. *Applied Catalysis B: Environmental*, *106*(3–4), 630–638. https://doi.org/10.1016/j.apcatb.2011.06.026

106. Popova, G. Ya., Chesalov, Ya. A., Andrushkevich, T. v., & Stoyanov, E. S. (2000). Heterogeneous selective oxidation of formaldehyde on oxide catalysts:In situ FTIR study of formaldehyde surface species on a V-Ti-O catalyst and oxygen effect. *Kinetics and Catalysis*, *41*(4), 546–552. https://doi.org/10.1007/BF02756073

107. Zhang, Z., Huang, K., Yuan, F., & Xie, C. (2014). Gas-sensing properties and in situ diffuse reflectance infrared Fourier transform spectroscopy study of formaldehyde adsorption and reactions on $SnO_2$ films. *Journal of Materials Research*, *29*(1), 139–147. https://doi.org/10.1557/jmr.2013.300

108. Chen, X., He, G., Li, Y., Chen, M., Qin, X., Zhang, C., & He, H. (2020). Identification of a Facile Pathway for Dioxymethylene Conversion to Formate Catalyzed by Surface Hydroxyl on $TiO_2$ -Based Catalyst. *ACS Catalysis*, *10*(17), 9706–9715. https://doi.org/10.1021/acscatal.0c01901

109. Chen, M., Wang, H., Chen, X., Wang, F., Qin, X., Zhang, C., & He, H. (2020). High-performance of Cu-TiO2 for photocatalytic oxidation of formaldehyde under

visible light and the mechanism study. *Chemical Engineering Journal*, *390*, 124481. https://doi.org/10.1016/j.cej.2020.124481

110. Chen, B.-B., Shi, C., Crocker, M., Wang, Y., & Zhu, A.-M. (2013). Catalytic removal of formaldehyde at room temperature over supported gold catalysts. *Applied Catalysis B: Environmental*, *132–133*, 245–255. https://doi.org/10.1016/j.apcatb.2012.11.028

111. Sun, Z., Zhu, X., Li, X.-S., Cai, R., & Zhu, A.-M. (2024). Mechanism and Reaction Kinetics of Formaldehyde Oxidation on $TiO_2$ : Amorphous Hydroxylated Outperforms Anatase. *Industrial & Engineering Chemistry Research*, *63*(10), 4353–4361. https://doi.org/10.1021/acs.iecr.3c04334

112. Lavalley, J.-C., Lamotte, J., Busca, G., & Lorenzelli, V. (1985). Fourier transform i.r. evidence of the formation of dioxymethylene species from formaldehyde adsorption on anatase and thoria. *Journal of the Chemical Society, Chemical Communications*, *14*, 1006. https://doi.org/10.1039/c39850001006

113. Lin, T., An, Y., Yu, F., Gong, K., Yu, H., Wang, C., Sun, Y., & Zhong, L. (2022). Advances in Selectivity Control for Fischer–Tropsch Synthesis to Fuels and Chemicals with High Carbon Efficiency. *ACS Catalysis*, *12*(19), 12092–12112. https://doi.org/10.1021/acscatal.2c03404

114. Wang, H., Dong, X., Zhao, T., Yu, H., & Li, M. (2019). Dry reforming of methane over bimetallic Ni-Co catalyst prepared from La(CoxNi1-x)0.5Fe0.5O3 perovskite precursor: Catalytic activity and coking resistance. *Applied Catalysis B: Environmental*, *245*, 302–313. https://doi.org/10.1016/j.apcatb.2018.12.072

115. Ostadi, M., Rytter, E., & Hillestad, M. (2019). Boosting carbon efficiency of the biomass to liquid process with hydrogen from power: The effect of H2/CO ratio to the

Fischer-Tropsch reactors on the production and power consumption. *Biomass and Bioenergy*, *127*, 105282. https://doi.org/10.1016/j.biombioe.2019.105282

116. Data, T. (2017). In NIST Chemistry WebBook, NIST Standard Reference Database Number 69.